

Contract No:

This document was prepared in conjunction with work accomplished under Contract No. DE-AC09-08SR22470 with the U.S. Department of Energy (DOE) Office of Environmental Management (EM).

Disclaimer:

This work was prepared under an agreement with and funded by the U.S. Government. Neither the U. S. Government or its employees, nor any of its contractors, subcontractors or their employees, makes any express or implied:

- 1) warranty or assumes any legal liability for the accuracy, completeness, or for the use or results of such use of any information, product, or process disclosed; or
- 2) representation that such use or results of such use would not infringe privately owned rights; or
- 3) endorsement or recommendation of any specifically identified commercial product, process, or service.

Any views and opinions of authors expressed in this work do not necessarily state or reflect those of the United States Government, or its contractors, or subcontractors.

Full Loop Thermodynamic Corrosion Inhibition and Sensing in Molten Chloride Systems - Final Report

Project Title: Full Loop Thermodynamic Corrosion Inhibition and Sensing in Molten Chloride Systems

Project Period: 02/01/18 – 02/29/20

Budget Period: 02/01/18 – 02/29/20

Submission Date: 2/29/20

Recipient: Savannah River National Laboratory

Address: Savannah River Site
Aiken, SC 29808

Award Number: 33871

Project Team: Savannah River Consulting
University of South Carolina
Israel Chemicals Ltd
Haynes International

Principal Investigator: Brenda L. Garcia-Diaz, Principal Engineer
Phone: (803) 725-9978
Email: brenda.garcia-diaz@srnl.doe.gov

Business Contact: Matt Biasiny, Contract Administration
Phone: (803) 952-8648
Email: Matthew.Biasiny@srs.gov

HQ Tech Manager: Levi Irwin

HQ Project Officer: Christine Bing

Executive Summary

The objective of this project is to increase the lifetime of Concentrated Solar Power (CSP) systems by identifying corrosion mitigation methods for heat transfer loops in the temperature range of 500 - 800 °C. Coupling of experimental data with CFD modeling has provided greater insight into corrosion mitigation methods and how they will be applied in molten salt systems with convective flows. The overall goal of the program is to demonstrate techniques that control corrosion while having limited impact on system alloys.

Dehydrated carnallite salt ($\text{MgCl}_2\text{-KCl-NaCl}$) was thermally treated by stepwise heating to 850 °C while sparging with Ar. After cooling, the salt was chemically treated by adding ~1.7 wt% Mg and heating to 850 °C. Corrosion tests were subsequently conducted with Haynes 230 (H230) specimens immersed in the salt at 800 °C for 100 h. Two separate trials yielded an overall H230 corrosion rate of $99.8 \pm 13.5 \mu\text{m/yr}$. Line scans and elemental maps acquired for the post-test samples revealed that Cr was selectively oxidized from the H230 surface to a depth of $9.0 \pm 0.7 \mu\text{m}$. Such a scenario was confirmed by inductively-coupled plasma optical emission spectrometry (ICP-OES) analysis, where the presence of Cr was detected in post-test salt aliquots.

Following the initial round of experiments, the Chloride Collective consisting of researchers from SRNL, NREL, and ORNL was established to standardize salt purification and corrosion testing. From the results of corrosion tests (800 °C for 100 h) conducted according to this protocol, a lower overall H230 corrosion rate of $44.7 \pm 11.0 \mu\text{m/yr}$ was obtained. As expected, post-test analysis of the samples and salt showed that Cr was selectively oxidized to a depth of $14.8 \pm 2.4 \mu\text{m}$.

The Chloride Collective then agreed to a second round of modifications to both the salt purification treatment and corrosion testing procedure. Regarding the salt treatment protocol, 6.1 wt% halite and 0.25 wt% Mg were added to ~4 kg of anhydrous carnallite (AC) in a quartz crucible, and the mixture was thermally/chemically treated in a single-step process by heating to 670 °C. During purification, a significant drop in the pH of a base solution placed in-line with the exhaust stream was observed at ~540 °C, close to the temperature corresponding to the thermal decomposition of MgOHCl (554 °C). The final composition of the purified salt was 45.7 wt% MgCl_2 , 39.0 wt% KCl, and 15.3 wt% NaCl; the addition of halite appeared to be effective in lowering the melting point (as predicted by the ternary phase diagram). Results of a filtration/titration procedure showed the average MgOHCl concentration in the treated salt to be $0.13 \pm 0.03 \text{ wt\%}$, a value that was in strong agreement with the $0.12 \pm 0.03 \text{ wt\%}$ figure reported by NREL.

The average corrosion rate calculated from immersion tests conducted after the second round of procedure modifications was $80.0 \pm 4.7 \mu\text{m/yr}$. This rate represented an approximately 80% increase from the $44.7 \pm 11.0 \mu\text{m/yr}$ value observed in previous tests; a similar trend was observed for immersion tests carried out by NREL (average corrosion rate of $249.2 \pm 23.2 \mu\text{m/yr}$ compared to $39.8 \pm 12.1 \mu\text{m/yr}$ in previous tests). Follow-up experiments performed with different salt purification and immersion testing crucible materials (Table 1) indicate that the use of quartz may have a deleterious effect on corrosion resistance, possibly due to the generation of oxidizing species from a reaction between the molten salt and SiO_2 .

Table 1. Corrosion test results obtained with different salt purification-immersion test vessel configurations.

Samples	Material: Salt Purification Vessel	Material: Corrosion Test Vessel	Average Corrosion Rate ($\mu\text{m}/\text{y}$)
H230-G3-SRC-Q1 to Q3	Quartz	Quartz	98.7 ± 21.6
H230-G3-SRC-Q4 to Q6	Quartz	Ni	117.9 ± 24.9
H230-G3-SRC-Ni1 to Ni3	Pyrolytic Boron Nitride	Quartz	106.3 ± 11.6
H230-G3-SRC-Ni4 to Ni6	Pyrolytic Boron Nitride	Ni	62.1 ± 2.6

Immersion tests were carried out to examine a worst-case scenario whereby no Mg chemical treatment was implemented during the salt purification process. The resulting salt was then used in an 800 °C/100 h corrosion test of H230 in a Ni crucible. It was found that the average corrosion rate of H230 with thermally purified carnallite was $722.2 \pm 23.2 \mu\text{m}/\text{yr}$, an approximately 810% increase from the $79.4 \pm 6.1 \mu\text{m}/\text{yr}$ obtained with dehydrated carnallite subjected to both a thermal and chemical treatment.

As part of an effort to develop effective corrosion mitigation strategies, Zr was successfully deposited on H230 samples at 800 °C via mass transfer in molten carnallite salt. The outward diffusion of Ni into Zr is believed to be the primary cause of both the formation of a Cr/W-rich “affected zone” and a rise in the thickness of a Ni/Zr-rich outer layer. X-ray diffraction (XRD) analysis of as-coated Zr-H230 samples confirmed the presence of various Ni-Zr compounds. Regardless of the exact mechanism by which these layers form, the film growth process did not appear to be self-limiting and thus, it was deemed risky as a corrosion mitigation approach in solar receivers and heat exchangers, where salt flow channels may only be $\sim 300 \mu\text{m}$ in diameter.

Corrosion tests were performed with Zr-coated H230 specimens in both ultra-high purity (UHP) air and Ar environments. While the mass of both samples decreased after testing, the final weights of the specimens were still greater than those measured prior to coating with Zr. Furthermore, the Cr content in the salt after each test was below the detectable limits for the ICP-OES instrument, thereby demonstrating the effectiveness of Zr-rich barrier layers as corrosion inhibitors. Based on our results, a manuscript titled, “Sacrificial Zirconium Coatings for Corrosion Mitigation in Molten Chloride Salts” has been submitted for publication in *Solar Energy Materials and Solar Cells*.

Table of Contents

Background 5

Project Results and Discussion 10

 Task 0.0: Qualify into The Chloride Collective 10

 Task 1.0: Exchange of Samples and Data with Project Cohorts 31

 Task 2.0: Identify Full Temperature Range for Corrosion Mitigation 34

 Subtask 2.1.1: Identify Full Loop Corrosion Mitigation Methods 34

 Subtask 2.1.2: Evaluate the Use of Self-Healing Coatings as Corrosion Inhibitors 37

 Subtask 2.1.3: Design and test a getter bed for a thermosiphon reactor in collaboration with ORNL 44

 Subtask 2.1.4: CFD Modeling of Optimized Getter Bed for Thermosiphon Integration 47

Conclusions **Error! Bookmark not defined.**

References 68

Background

Savannah River National Lab (SRNL) researchers have investigated molten halide corrosion for concentrated solar power (CSP) systems and nuclear applications [1]. This has included investigations that showed unmitigated corrosion is only mass transfer limited with very fast kinetics for Ni-, Fe-, and Co-based families of alloys. The main corrosion mechanism is the selective oxidation of Cr and Mn along grain boundaries. Figure 1 illustrates the corrosion mechanism proposed by SRNL for the selective oxidation of Cr, which is the principle corrosion pathway. It is believed that corrosion follows initiation and propagation steps. Initiation occurs at grain boundaries when impurities cause the oxidation of chromium in chromium carbides to CrCl_3 . The CrCl_3 can then oxidize metallic Cr in the alloy to CrCl_2 , which is subsequently transported to Cr depleted regions of the system such as welds, where it deposits as NiCr or other compounds. The formation of a NiCr pathway also reforms CrCl_3 , which in turn oxidizes more Cr. Two separate projects have been funded by the DOE to determine the most likely mechanism of chromium oxidation in alloys; one at Oak Ridge National Laboratory (ORNL) entitled, *Comparison of Protecting Layer Performance for Corrosion Inhibition in Molten Chloride Salts through Interfacial Studies at the Molecular Scale* (CPS #33874), and another at Rensselaer Polytechnic Institute entitled, *Development of In-Situ Corrosion Kinetics and Salt Property Measurements* (DE-EE0008380).

SRNL has shown that active metals with low thermodynamic reduction potentials (e.g., Mg, Zr, and Ti) prevent selective oxidation of Cr and Mn by reducing the electrochemical potential of the alloy below the equilibrium potentials for Cr and Mn oxidation. Active metals thermodynamically prevent the corrosion mechanism displayed in Figure 1 by: 1) providing a more favorable species to react with impurities rather than allowing them to react with chromium carbides ('gettering'), 2) preventing the oxidation of Cr compounds, and 3) reducing CrCl_2 and CrCl_3 in the molten salt to metallic Cr. Research at SRNL showed that Mg, Zr, and Ti can all inhibit corrosion, but Mg was used in previous SunShot research because it had no interaction with the alloy surface and because it does not introduce a new element to the salt system. The studies at SRNL focused on temperatures in the range of 750 to 950 °C, which represent worst-case scenarios that may occur at localized hot-spots in the receiver. Because of this temperature range, the 650 °C freezing point of Mg was not a significant consideration. Lower-cost alloys were not considered because they did not possess the required mechanical strength.

SRNL has participated in the Gen 3 Roadmap Workshops with the SunShot program. As part of these workshops, it became clear that adapting corrosion mitigation methods to the full 500 - 750 °C range envisioned for the 10 MW demonstration was a top priority to ensure that a molten salt flow loop can achieve a 30+ year lifetime to enable low levelized energy costs. The proposed work will use the thermodynamic corrosion inhibition framework developed in the previous DOE project, but will examine ways that it can be adapted for the full flow loop temperature range. In addition, the proposed research will adapt methods to monitor the corrosion inhibitor concentration as well as add the capability to monitor for corrosion products that are of interest to industry members.

To expand the temperature range of the corrosion inhibition method, there are a variety of pathways that have demonstrated promising initial results. These methods include: 1) using Mg-alloys with a lower melting point, 2) utilizing sacrificial Ti or Zr elements as

cathodic protection or self-healing coatings, 3) employing salt redox couples with a low electrochemical potential with electrochemical regeneration, and 4) using novel corrosion inhibitors or salt treatment methods.

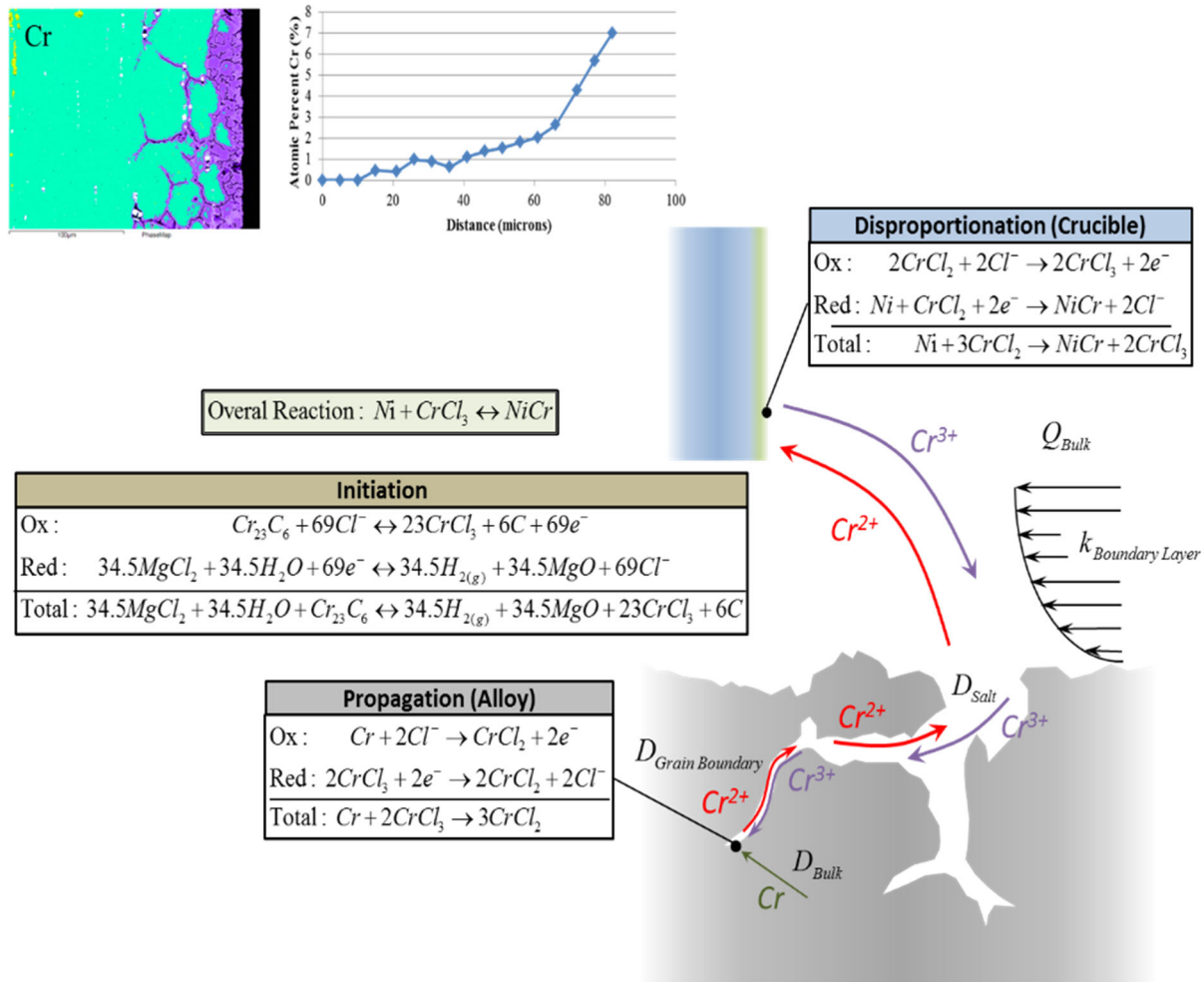


Figure 1. EDX of Haynes 230 in molten $MgCl_2$ -KCl after 100 h and proposed mechanism for selective oxidation of chromium in molten salts [1].

One approach to test is lowering the melting point of Mg by alloying it with other active metals such as Al or Zn. Eutectic Mg-Al alloy (~70-30 at%) has a melting point of 440 °C, which is on the same order as that of NaCl- $MgCl_2$ -KCl ternary salt mixtures from ICL Innovations. Eutectic Mg-Zn alloys can have melting points as low as 341 °C. Therefore, reduction of the Mg melting temperature can be readily accomplished. The main question is if corrosion inhibition will be equally as effective. Since the corrosion potential of alloying elements such as Al is low, this will likely be as effective, but the interaction with metallic tubing species would need to be determined.

A second approach that has been demonstrated by SRNL is to use Zr or Ti to mitigate corrosion. Both Zr and Ti can form intermetallics with Ni or form carbides that lead to

mass gain, which makes calculating and comparing corrosion rates more complicated. Shown in Figure 2 are SEM/EDS images where Zr was used as a corrosion inhibitor. Here, Zr oxidizes from the pure Zr coupon and forms an alloy with Ni at the Haynes 230 (H230) surface. Such an interaction could assist in preventing corrosion by forming cubic close-packed carbides such as ZrC and TiC. The less stable chromium carbides (e.g., Cr₂₃C₆) at H230 grain boundaries over temperatures of interest facilitate selective

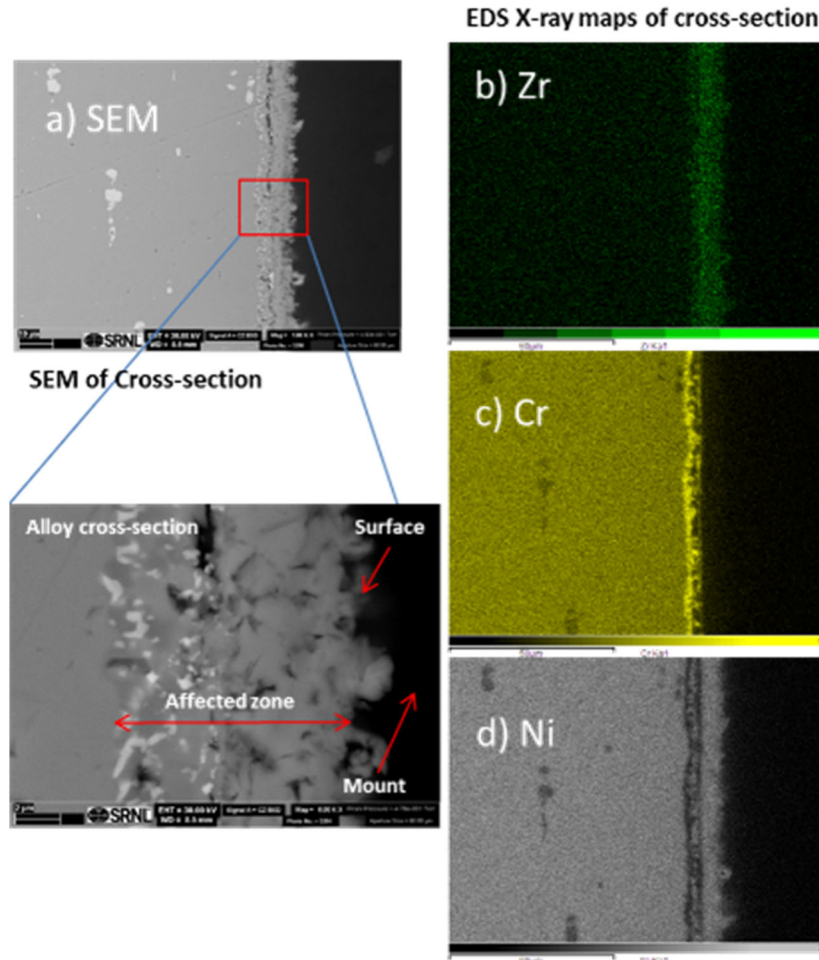


Figure 2. SEM/EDX of Haynes 230 after 100 hours in MgCl₂-KCl with Zr as a corrosion inhibitor [1].

oxidation of Cr. In addition to lowering the corrosion potential, the use of Ti and Zr as corrosion inhibitors can tie up carbon at the grain boundaries in more stable carbides and stop corrosive attack. The incorporation of stable carbide forming elements (e.g., Ti, Nb, Ta, Zr) is a known method of improving the corrosion resistance of alloys and is used in materials such as Type 347 stainless steel. Therefore, utilizing Ti or Zr as a corrosion inhibitor has potential advantages over Mg. One challenge in implementing such a strategy is, unlike Mg, Ti and Zr are solids. This can have both advantages and disadvantages. The advantage is that there would be no issues related to phase separation (which may occur with some metals), while a potential drawback would be that corrosion inhibition may not be evenly distributed. One method of incorporating Ti and Zr is to make them into sacrificial electrodes that could be incorporated periodically in tees

or other fittings so as to cathodically protect components. A second method would be to use active metals as self-healing coatings. Metals can thermodynamically migrate due to activity differences in systems at high temperatures in molten electrolytes with small concentrations of their corresponding metal ions in solutions. Consequently, even incomplete coating with Ti or Zr could lead to uniform, self-healing films throughout a CSP system. This has been demonstrated by SRNL using coupons coated on only one side with Ti or Zr. After 100 h, the metals partially migrate to the other side of the sample. It should be noted that the ability of Ti or Zr to form self-limiting coatings has not been demonstrated.

A third method of corrosion inhibition is to use redox couples (e.g. $ZrCl_2/ZrCl_3$ or $TiCl_2/TiCl_3$) in the molten salt. The presence of redox couples with active metals buffers the electrochemical potential below the point at which Cr oxidation can occur. A unique aspect of redox couples is that the oxidized couple can be reduced back to a lower oxidation state in-situ with immersed electrodes, which allows regeneration of the corrosion inhibitors. Challenge to address include finding proper concentration ratios that provide adequate buffering and identifying convenient methods to prepare the salts at an industrial scale.

A fourth method to be considered is a combination of the above approaches above or novel approaches that are not listed. For example, Zr self-healing coatings could be used with Zr-based redox couples to provide both passive and active methods of corrosion protection. This could provide a significant amount of protection and still only require minor amounts of the corrosion inhibitor.

All four of the aforementioned corrosion mitigation methods involve changing the thermodynamic potential of the molten salt. SRNL has demonstrated that corrosion susceptibility can be assessed by measuring the electrochemical potential in a system using a reference electrode. The monitoring of corrosion potential in a system with and without Mg present as a corrosion inhibitor is shown in Figure 3. In previous SunShot research, SRNL calculated that the oxidation of pure Cr to $CrCl_2$ would occur above 0.5 V vs Ag/AgCl. The potential of the H230 coupons in pure and commercial salt were close

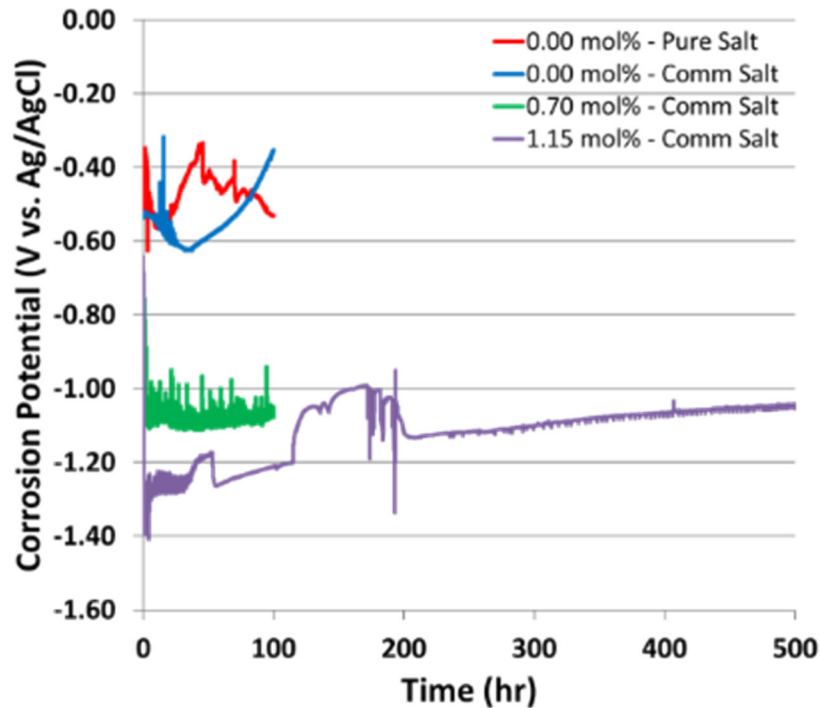


Figure 3. Electrochemical potential monitoring for experiments with different amounts of corrosion inhibitors and for varying time [1].

to this potential during a 100 h test and exceeded the 0.5 V value for extended periods of time. These samples also showed corrosion, which is not surprising because the specimens were at a potential where selective oxidation of Cr could occur. For both 0.7 and 1.15 wt% Mg (-1.5 V vs Ag/AgCl equilibrium potential) additions to commercial salt, the potential of the sample decreased to below -1.0 V. Having a potential below approximately -0.5 V vs. Ag/AgCl thermodynamically prevents selective oxidation of Cr from occurring, and no corrosion occurred in either case with Mg addition. A test with 1.15 wt% Mg was run for 500 h to see if there was consumption of the Mg with time (due to impurity ingress, etc.) and to confirm that changes in potential could be monitored. The data showed a slight increase in potential with time that is likely due to the consumption of some Mg by impurities in the initial phase. It is expected that the potential would stabilize in the long term, but that it could be monitored and more Mg could be added as needed to react with any impurities. In the system with the lower electrochemical potential, no corrosion occurred. Therefore, SRNL has proposed the use of a reference electrode as a method to monitor thermodynamic corrosion inhibition. As part of this proposal, the electrochemical potential of systems using adapted corrosion mitigation methods would be assessed and quantified. This would provide the basis for the detection of corrosion inhibitors in the system.

Conversations with industry members at SunShot Gen 3 workshops indicated that they believe methods for detecting corrosion in real-time need to be developed for CSP plants so any necessary action can be implemented quickly. Another application of interest is in detecting oxidation products of corrosion inhibitors to ensure that they are properly being settled out and not building up in the flowing salt to concentrations where they could agglomerate and cause clogging. It is anticipated that the oxide would settle out in the

salt tanks. Raman spectroscopy is one technique that allows for the detection of corrosion products in the ppm range. Sporian Microsystems has developed Raman probes for use with molten salts. SRNL will work with Sporian to demonstrate the detection of corrosion products in industrial molten chloride salts over the full 500 -750 °C operating temperature range both with and without corrosion inhibitors.

Project Results and Discussion

Task 0.0: Qualify into The Chloride Collective

The objective of this task was to perform salt purification, characterization, and corrosion of H230 samples according to the Collective's agreed upon guidelines. Similar methods and equipment were used as described in previous project reports [2, 3], except for changes agreed to by The Chloride Collective.

The salt for testing was dehydrated carnallite provided by ICL and treated in-house at SRNL. The chemical composition of the received salt is shown in Table 2. For the initial H230 corrosion testing, 2 trials were carried out at 800 °C for 100 h to obtain additional results for statistical analysis, as one of the samples in the first trial likely made galvanic contact with the bottom of the Ni crucible, thereby significantly increasing the corrosion rate (1239.7 $\mu\text{m}/\text{yr}$). The outlier data point was excluded from the average calculation.

Corrosion rate results for the first 2 trials are shown in Table 3 with the average, standard deviation, and a T-test for comparing the two groups. The corrosion rate comparison was performed using a significance level of 5% and a two-tailed T-test analysis. The p-values from the T-test are shown in green and red cells for $p > 5\%$ (statistically significant) and $p < 5\%$ (not statistically significant), respectively. Comparison of the two groups show that $p = 43.2\%$ and hence, the differences between the two groups are not statistically significant. The overall average corrosion rate was 99.8 $\mu\text{m}/\text{yr}$ with a standard deviation of 13.5 $\mu\text{m}/\text{yr}$.

Table 2. Chemical composition (in wt%) of dehydrated carnallite provided by ICL.

Element/Compound	Concentration (wt%)
MgCl ₂	48.7
KCl*	41.0
NaCl	3.8
MgO	1.58
H ₂ O	4.3
SO ₄ ²⁻	0.02
Br	0.58
B	0.0001
Insoluble Residues	< 0.01
K ₂ O recalculated from KCl is 25.9 wt%	

Table 3. Corrosion rates and t-test data for H230 in carnallite salt at 800 °C for 100 h.

Salt	MgCl ₂ -KCl-NaCl	
Test	1 st Trial	2 nd Trial
	113.4	96.5
	98.8	79.5
		110.7
Average	106.1	95.6
Std Dev	10.3	15.6
2σ	20.6	31.2

Test	1 st Trial	2 nd Trial
1 st Trial	106.1 ± 20.6	43.20%
2 nd Trial		95.6 ± 31.2

Gray cells in diagonal: average corrosion rate (μm/yr) ± 2σ.

Red cells: p < 5% means that the difference in compared values is statistically significant.

Green cells: p > 5% means that the difference in compared values is not statistically significant.

Characterization of the post-test samples from the first trial was performed by scanning electron microscopy (SEM) and EDX, while the salt was analyzed by inductively-coupled plasma optical emission spectrometry (ICP-OES). The ICP-OES results obtained for as-received carnallite, carnallite after treatment, and post-corrosion test salt (first trial data set) are shown in Table 4. No significant changes from the as-received salt were measured for the elements of interest. However, the results for the post-corrosion test salt show that Ni and Cr were the primary elements present in the salt. Although Fe was detected for sample H230-G3-3, this sample likely made galvanic contact with the bottom of the Ni crucible.

Elemental maps of the H230-G3-2 cross-section after corrosion testing are shown in Figure 4. From the EDX maps, it is evident that Cr is being selectively oxidized from the sample.

Table 4. ICP-OES results for carnallite as-received, purified by stepwise heating, and after corrosion testing; results are given in units of ppm.

Salt Sample	Ni	Cr	Fe	Co	Mo	Mn	Ca
As-received	<DL	<DL	<DL	<DL	<DL	<DL	744.2
Post-treated	<DL	<DL	<DL	<DL	<DL	<DL	1011.4
H230-G3-1	153.8	315.4	<DL	<DL	<DL	<DL	983.9
H230-G3-2	277.3	122.3	<DL	<DL	<DL	<DL	954.5
H230-G3-3	437.0	145.2	275.2	<DL	<DL	<DL	881.7

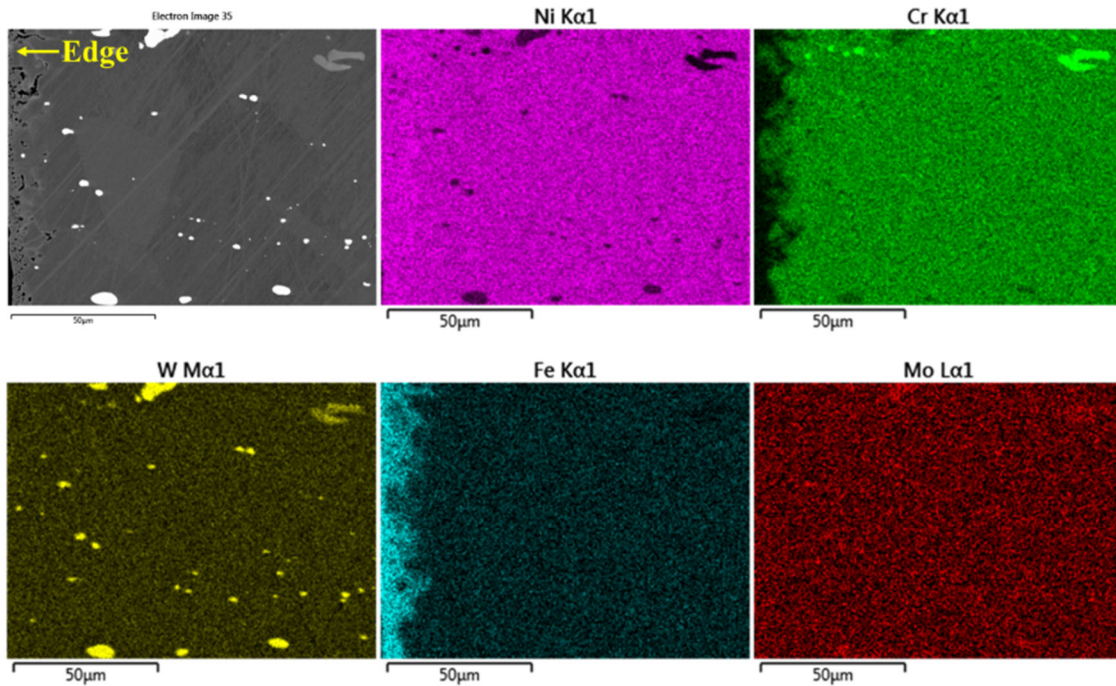


Figure 4. Elemental maps obtained for H230-G3-2 after corrosion testing in carnallite at 800°C for 100 hours.

Due to differences in the initial corrosion results obtained by The Chloride Collective, it was agreed that the salt purification process and corrosion tests would be repeated with detailed conditions, material and supplies. SRNL contributed to the development of the procedure and took the lead in the development of protocols for SEM/EDX characterization of the H230.

Corrosion testing of H230 samples at 800 °C for 100 h was conducted according to the procedure devised by The Chloride Collective. Photographic images of the testing configuration are shown in Figure 5. Ni wire (1 mm diameter) was first passed through holes in three H230 coupons and subsequently twisted to support an insulating alumina tube (Figure 5(a)). The tubing was then put through holes in the center of both a Ni crucible lid and alumina disc. Excess Ni wire protruding from the top of the alumina tube was shaped into a circular pattern to hold the Ni wire-H230 assembly firmly in place (Figure 5(b)). Lastly, a second alumina disc was placed on top of the first and held into place by a strip of Ta foil tucked under the first disc (Figure 5(c)).

In an inert glovebox, each Ni wire-H230 assembly was placed into a 250 mL Ni crucible filled with approximately 170 g of purified carnallite. The crucibles were put into stainless steel bags with a small (4-5 cm²) amount of Ta foil; the bags were then folded and crimped. Next, the crucibles were removed from the glovebox and immediately inserted into an Inconel 600 vessel situated inside a 3-zone horizontal tube furnace. Upon evacuating and filling the vessel three times with Ar, the system was purged overnight with Ar at a flow rate of ~250 sccm. To eliminate moisture and oxygen from the Ar stream, the gas was circulated through a two-stage purification setup prior to entering the Inconel vessel. After purging the system, corrosion tests were conducted at 800 °C for 100 h, after which time the furnace was shut off and allowed to cool naturally to room

temperature. At the conclusion of each experiment, the H230 specimens were removed from the carnallite and cleaned via sonication for 20 min in deionized water. Post-test salt samples were taken inside a glovebox prior to ICP-OES analysis.

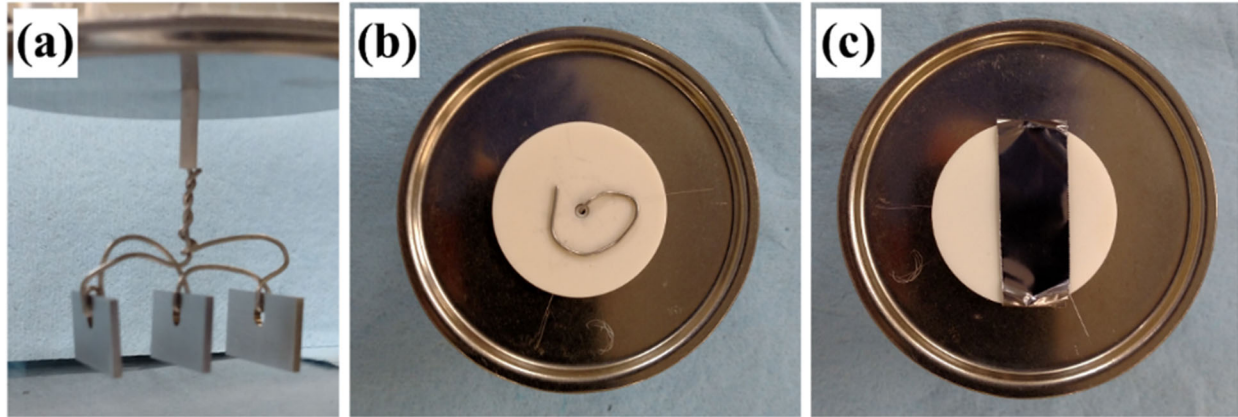


Figure 5. (a) Ni wire-H230 assembly for corrosion testing, (b) top view of Ni wire on bottom alumina disc, and (c) completed assembly with Ta foil holding top alumina disc in place.

Shown in Table 5 are the results from two corrosion tests conducted under The Chloride Collective procedure. Similar corrosion rates of $44.5 \pm 15.0 \mu\text{m/yr}$ and $44.8 \pm 8.8 \mu\text{m/yr}$ were observed in the first and second tests, respectively. The average overall corrosion rate was calculated as $44.7 \pm 11.0 \mu\text{m/yr}$, a value whose difference is not statistically significant from the $39.8 \pm 12.1 \mu\text{m/yr}$ average corrosion rate calculated by the National Renewable Energy Laboratory.

In addition to carrying out corrosion tests with the three-sample Chloride Collective configuration, two other experiments were conducted at $800 \text{ }^\circ\text{C}$ for 100 h. In the first test, The Chloride Collective procedure was followed with one exception: only one H230 specimen was placed into each crucible (as in the first round of Chloride Collective tests). The average corrosion rate from three samples tested in this manner was $52.7 \pm 15.8 \mu\text{m/yr}$ (Table 6). In the second experiment, effects of galvanic contact on corrosion were evaluated by connecting three H230 coupons with Ni wire and hanging the specimens from a Ni crucible lid. This configuration was designed to ensure electrical contact between the H230, lid, and Ni crucible. The average corrosion rate from two galvanic tests was $350.0 \pm 31.6 \mu\text{m/yr}$ (Table 7). Such a value is consistent with results from earlier galvanic corrosion tests at SRNL, where an average corrosion rate of $497.0 \pm 7.9 \mu\text{m/yr}$ was observed with the same configuration, but at a higher temperature of $850 \text{ }^\circ\text{C}$.

Table 5. Results from Chloride Collective tests conducted at 800 °C for 100 h.

Sample ID	1 st Test: Corrosion Rate (µm/y)	Sample ID	2 nd Test: Corrosion Rate (µm/y)
H230-G3-SRC-5	27.3	H230-G3-SRC-15	36.0
H230-G3-SRC-6	53.1	H230-G3-SRC-16	44.7
H230-G3-SRC-7	53.3	H230-G3-SRC-17	53.7
Average (µm/y):	44.5	Average (µm/y):	44.8
St. Dev. (µm/y):	15.0	St. Dev. (µm/y):	8.8
Average corrosion rate from both tests (µm/y): 44.7 ± 11.0			

Table 6. Results from Chloride Collective tests conducted at 800 °C for 100 h.

Sample ID	Corrosion Rate (µm/y)
H230-G3-SRC-8	34.7
H230-G3-SRC-9	59.6
H230-G3-SRC-18	63.9
Average (µm/y):	52.7
St. Dev. (µm/y):	15.8

Table 7. Corrosion test results for H230 in galvanic contact with the crucible.

Sample ID	1 st Test: Corrosion Rate (µm/y)	Sample ID	2 nd Test: Corrosion Rate (µm/y)
H230-G3-SRC-12	349.7	H230-G3-SRC-20	402.0
H230-G3-SRC-13	336.6	H230-G3-SRC-21	316.7
H230-G3-SRC-14	369.9	H230-G3-SRC-22	325.2
Average (µm/y):	352.0	Average (µm/y):	348.0
St. Dev. (µm/y):	16.8	St. Dev. (µm/y):	47.0
Average corrosion rate from both tests (µm/y): 350.0 ± 31.6			

Elemental maps acquired for samples H230-G3-SRC-5 and H230-G3-SRC-6, which exhibited corrosion rates of 27.3 and 53.1 µm/yr, respectively, are presented in Figure 6. According to The Chloride Collective procedure, the elements of interest for energy dispersive X-ray spectroscopy (EDX) are Ni, Cr, W, Fe, Mo and Mg. However, the Mg concentration was found to be negligible (<1.0 at%) and thus, maps for this element are not shown. From Figure 6, it is seen that the bulk interior of the H230 can be characterized by W-rich precipitates dispersed in a matrix composed primarily of Ni and Cr. In contrast,

the edges of the samples exposed to molten carnallite are depleted in Cr and contain higher concentrations of Ni and Fe; these Cr depleted regions are denoted in Figure 6(a) and (b). The phenomenon of selective oxidation and depletion of Cr from H230 surfaces exposed to molten salt has been noted in previous reports. To quantify the bulk Cr content and Cr depletion depth, multiple line scans were obtained for the samples in Figure 6; the results are shown in Table 8. Here, the maximum depth of Cr depletion was defined as the point at which the Cr concentration decreases by more than 2 standard deviations from the bulk value. As evident in Table 8, the line scan data are consistent with the difference in corrosion rates between the two specimens, as Cr depletion depths of 7.85 ± 0.8 and 19.9 ± 2.8 μm were calculated for H230-SRC-G3-5 and H230-SRC-G3-6, respectively.

As detailed in The Chloride Collective procedure, multiple EDX point scans were taken at different regions of the surface for H230-G3-SRC-6. A plane view scanning electron microscopy (SEM) image of H230-G3-SRC-6 and the average elemental concentrations from 15 point scans are presented in Figure 7; the average elemental content from point scans obtained on the surface of pristine (i.e., untested) H230 are also provided for reference. When compared to pristine H230, the concentration of Ni on the surface of H230-G3-SRC-6 increased by $\sim 16\%$ after testing, while the content of Cr decreased by approximately 75%. Such trends are also observed in the Ni and Cr maps of Figure 6 when moving from interior of the sample to the edge.

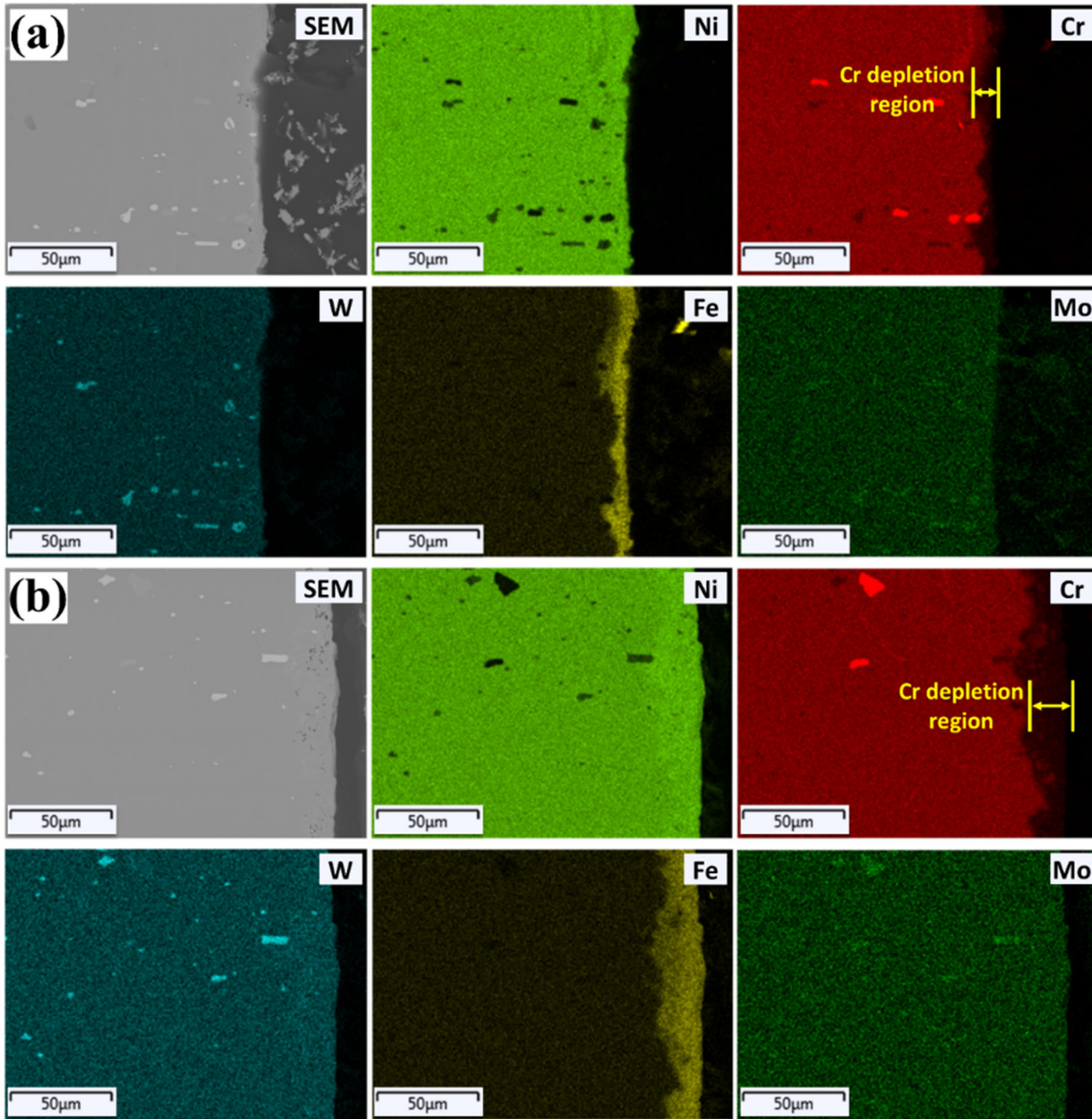
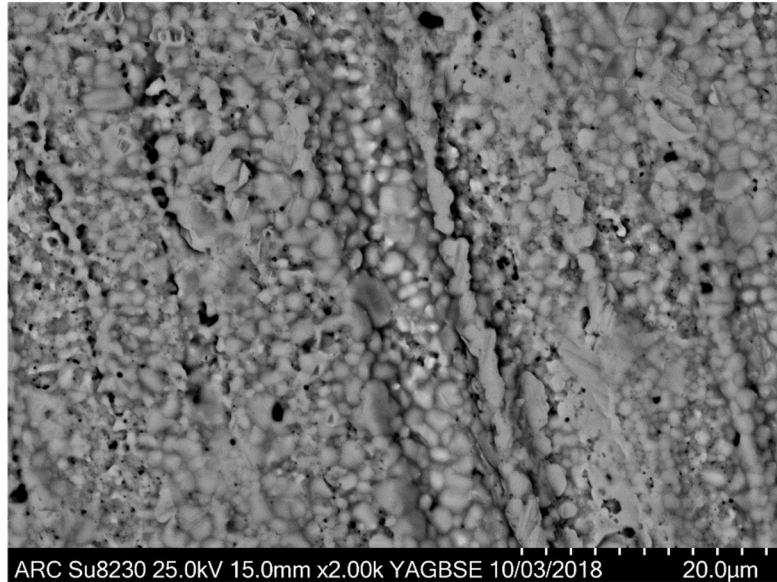


Figure 6. Elemental maps acquired for (a) H230-G3-SRC-5 and (b) H230-G3-SRC-6.

Table 8. Results from Chloride Collective tests conducted at 800 °C for 100 h.

H230-G3-SRC-5		H230-G3-SRC-6	
Parameter	Value	Parameter	Value
Bulk Cr Content (at%)	28.3	Bulk Cr Content (at%)	28.6
St. Dev. in Bulk Cr content (at%)	0.3	St. Dev. in Bulk Cr content (at%)	0.2
Cr depletion depth (µm)	7.9	Cr depletion depth (µm)	19.9
St. Dev. in Cr depletion depth (µm)	0.8	St. Dev. in Cr depletion depth (µm)	2.8



H230-G3-SRC-6 (Point Scans: Surface)			Pristine H230 (Point Scans: Surface)		
Element	Mean Conc. (at%)	St. Dev. (at%)	Element	Mean Conc. (at%)	St. Dev. (at%)
Ni	72.0	0.4	Ni	62.0	4.7
Fe	13.8	0.5	Fe	2.0	3.4
Cr	6.9	0.2	Cr	28.3	0.2
W	5.7	0.3	W	4.5	2.8
Mo	1.2	0.2	Mo	1.0	1.6
Mg	0.4	0.3	Mg	Not detected	Not detected
H230-G3-SRC-6 (Line Scans: Bulk Cross-section)			Pristine H230 (Line Scans: Bulk Cross-section)		
Element	Mean Conc. (at%)	St. Dev. (at%)	Element	Mean Conc. (at%)	St. Dev. (at%)
Ni	62.7	1.4	Ni	61.1	4.8
Fe	2.0	0.4	Fe	2.0	1.4
Cr	28.6	0.2	Cr	28.0	3.4
W	5.0	0.8	W	4.6	2.8
Mo	0.9	0.6	Mo	1.1	1.6
Mg	0.7	0.9	Mg	Not detected	Not detected

Figure 7. Plane view SEM image and average elemental concentrations from 15 point scans across the surface of specimen H230-G3-SRC-6; the composition of pristine H230 derived from line and point scans is also provided along with cross-sectional line scan data from the bulk region of H230-G3-SRC-6.

The results of ICP-OES analysis of as-received, post-treated, post-corrosion test salt samples from the second round of Chloride Collective tests are shown in Table 9. In contrast to the data obtained from the first Chloride Collective tests, the concentration of Ni in all salt samples was below detectable limits. Furthermore, the content of Cr in the salt used for H230-G3-SRC-9 was lower than that for all specimens in the first Chloride Collective tests, which were also conducted with one sample per crucible.

Table 9. ICP-OES data of salt samples from Chloride Collective tests; results are given in units of ppm.

Salt Sample	Ni	Cr	Fe	Co	Mo	Mn	Ca
As-received	<9.2	<2.0	<1.9	<2.1	<8.9	2.5	918
Post-treated (devised procedure)	<11.1	<1.7	218	<1.8	<11.0	102	1100
H230-G3-SRC-5 to 7 (3 samples/crucible)	<27.6	136	<2.9	<2.7	<8.6	102	977
H230-G3-SRC-15 to 17 (3 samples/crucible)	<11.8	167	<1.7	<1.9	<8.0	105	940
H230-G3-SRC-9	<9.2	105	<1.9	<2.1	<8.9	168	998

Upon further modifications to testing protocols implemented by members of The Chloride Collective, additional salt purification and immersion corrosion experiments were conducted. For the purification procedure, approximately 4 kg of as-received anhydrous carnallite (AC) was placed into a quartz crucible, followed by the addition of 6.1 wt% halite and 0.25 wt% Mg (in the form of chips). Photographic images of both the salt mixture prior to heating and the Inconel 600 purification vessel are shown in Figure 8(a) and (b), respectively. Upon loading the quartz crucible into the chamber, the system was evacuated and refilled three times with ultra-high purity (UHP) Ar. The flow rate of Ar through the primary gas inlet (“E” in Figure 8(b)) was maintained at 500 sccm throughout the entirety of the purification process. Furthermore, both a Mo sparge tube and K-type thermocouple shielded with Mo tubing (closed on one end) were inserted into the salt before heating; the flow rate of Ar through the sparge tube was kept constant at 150 sccm. Ultimately, the salt was heated at a peak temperature of ~670 °C. The pH of a 0.1 M NaOH solution used to neutralize exhaust gases was closely monitored throughout the duration of the experiment. After cooling naturally to room temperature, the solidified product was removed from the quartz crucible and placed in an inert glovebox for use in corrosion testing.

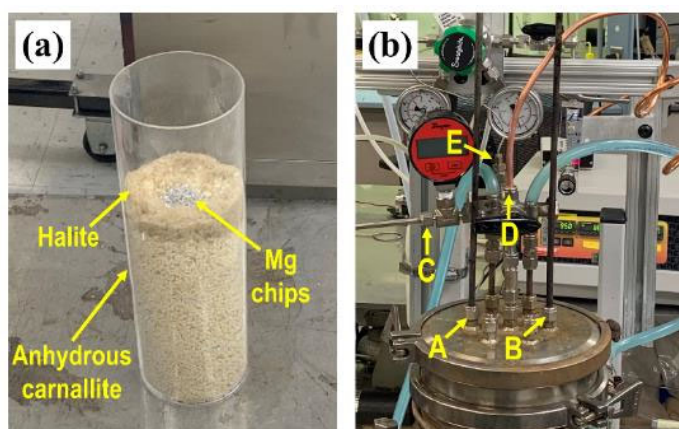


Figure 8. (a) Photographic image of a quartz crucible loaded with AC, halite, and Mg chips prior to purification. (b) Photograph of the salt purification chamber; denoted in the figure are ports for (A) K-type thermocouple with Mo shielding, (B) Mo sparge tube, (C) exhaust, (D) vacuum, and (E) Ar cover gas.

Shown in Figure 9 is a plot of pH and temperature versus time acquired during a salt purification experiment. Above ~ 200 °C, the pH of the solution decreased from 12.17 to a final value of 0.87 after the dwell time at 670 °C. Interestingly, the sharp decrease in pH observed after ~ 2 h occurs near the temperature at which MgOHCl is reportedly decomposed into MgO and HCl (554 °C [4]).

The composition of the as-received AC and purified AC + halite was quantified via inductively-coupled plasma optical emission spectrometry (ICP-OES); the results obtained from both SRNL and NREL are provided in Figure 10. Based on the ICP data, the bulk composition of the purified salt (neglecting impurities) is 39.0 wt% KCl, 15.3 wt% NaCl, and 45.7 wt% MgCl₂. According to the ternary phase diagram for KCl-MgCl₂-NaCl (Figure 11(a) [5]), the addition of halite to the salt mixture should decrease the melting point. From temperature-time plots acquired during the purification of dehydrated carnallite and AC + halite (Figure 11(b)), small plateaus, likely due melting of the salt, appear in the data obtained for both salts. However, the plateau for the AC + halite mixture is visible at a temperature ~ 50 °C lower than that for dehydrated carnallite.

A technique involving successive filtration and titration procedures was employed to determine the quantity of MgOHCl in both as-received and purified carnallite [6]. In this method, approximately 500 mg of salt is placed in a beaker with ~ 250 mL of methanol and stirred for at least 1 h. The resulting methanol-salt mixture is then filtered so as to remove dissolved chlorides and collect MgO/MgOHCl impurities. The MgO/MgOHCl residue is then placed in a beaker with ~ 200 mL of deionized (DI) water, which serves to dissolve MgOHCl species while leaving MgO particles suspended in solution. Another filtration is subsequently performed to remove the MgO/Mg(OH)₂ residue and produce a filtrate containing MgCl₂. After raising the pH of the filtrate to 10.00 ± 0.1 with an ammonium hydroxide buffer solution, Calmagite indicator is added. Depending on the

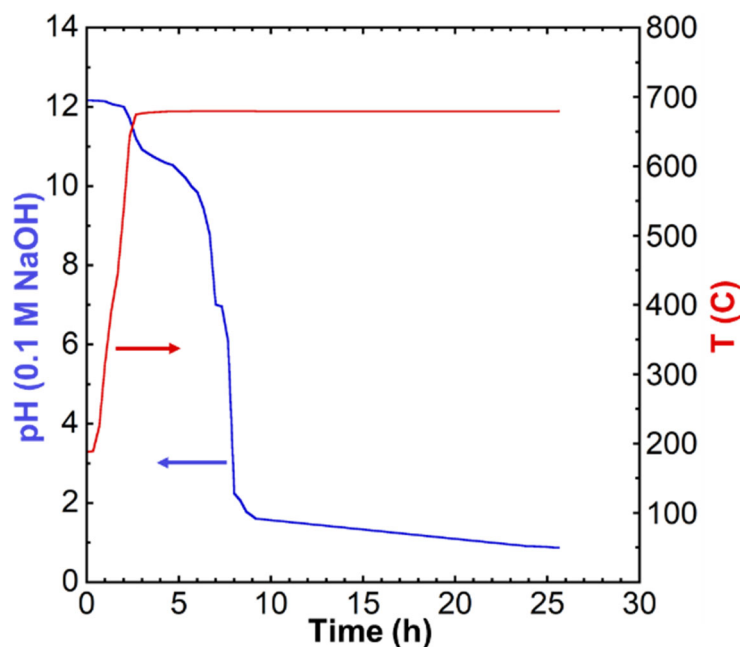


Figure 9. Plot of pH and temperature vs. time during salt purification.

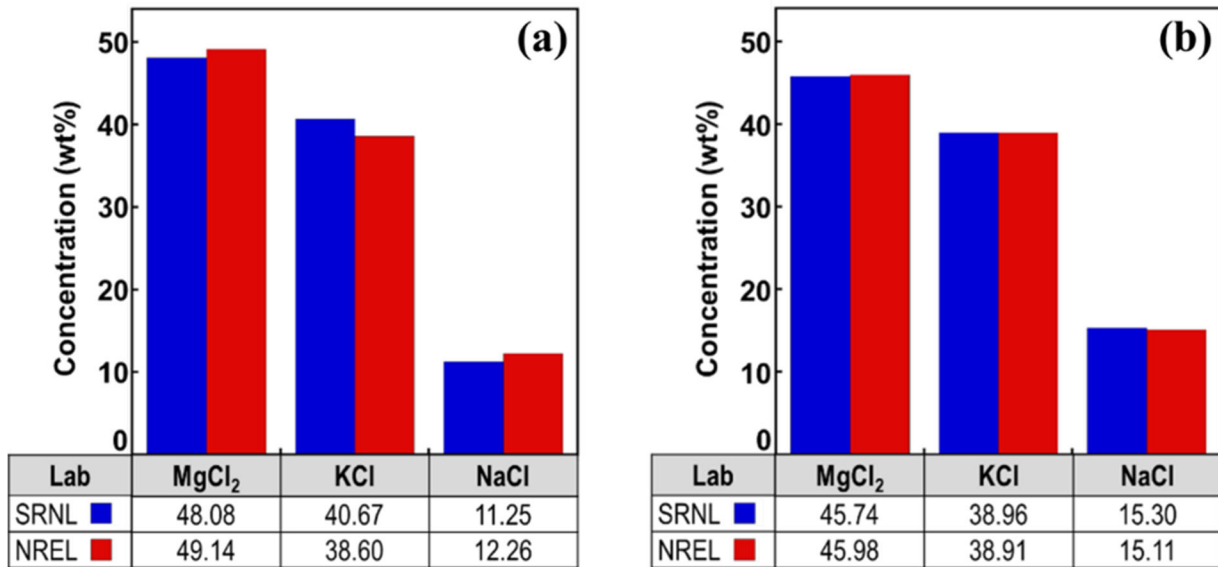


Figure 10. ICP-OES results obtained for (a) as-received AC and (b) purified AC + halite; results from NREL are provided for comparison.

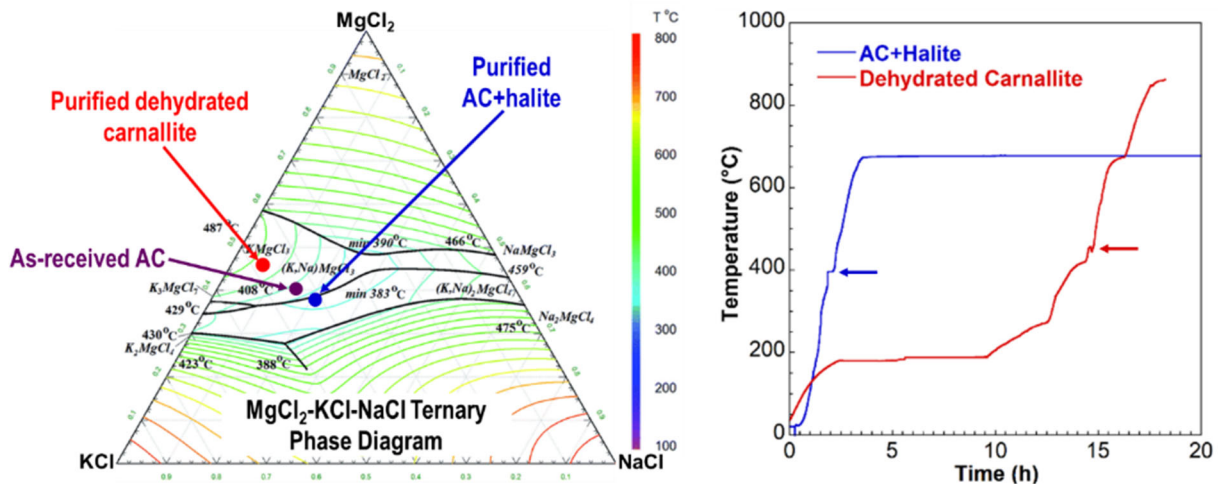


Figure 11. (a) Ternary phase diagram for KCl-MgCl₂-NaCl [5] and (b) temperature-time plots acquired during the purification of dehydrated carnallite and AC + halite (Note: The peak temperature and dwell times were different for AC+halite and dehydrated carnallite in accordance with procedural modifications agreed to by the Chloride Collective).

initial concentration of MgOHCl in the salt sample, the introduction of Calmagite indicator will cause the filtrate to turn either red (higher MgOHCl content) or violet (lower MgOHCl concentration). As a final step, the filtrate is titrated with a 5 mM EDTA solution until a color change from red/violet to blue is observed.

The titration results obtained for as-received and purified carnallite are given in Table 10. For the as-received AC, the average MgOHCl concentration of 0.61 ± 0.03 wt% is within one standard deviation of the 1.0 ± 0.5 wt% value reported by NREL. Stronger agreement was observed in the data acquired for purified AC, where MgOHCl concentrations of 0.13 ± 0.03 wt% and 0.12 ± 0.03 wt% were recorded by NREL and SRNL, respectively.

Corrosion tests were conducted with purified carnallite at 800 °C for 100 h. A photographic image of the crucible setup is shown in Figure 12(a). Three H230 coupons were mounted onto a Ni lid with Ni wire and subsequently placed inside a quartz crucible with ~200 g of purified carnallite. The quartz crucible was then inserted into a stainless steel bag with Ta foil and sealed. An Inconel 600 chamber situated in a three-zone horizontal tube furnace was loaded with the sealed crucibles for the corrosion test. Throughout the duration of the corrosion experiment, a 150 sccm flow of UHP Ar was employed as the cover gas; the Ar was passed through a moisture trap and gettering furnace prior to entering the chamber. At the conclusion of the test, the furnace was shut off and allowed to cool naturally to room temperature. An image of H230 specimens encased in solidified carnallite at the completion of the corrosion experiment is displayed in Figure 12(b). Post-test H230 specimens were cleaned in DI water and then weighed to determine the corrosion rate.

Table 10. MgOHCl content in as-received and purified AC as determined by titration.

Titration	MgOHCl:	MgOHCl: Purified AC
	As-received AC (wt%)	(wt%)
Run #1	0.64	0.09
Run #2	0.62	0.14
Run #3	0.58	0.15
Average (wt%)	0.61	0.13
Std. Dev. (wt%)	0.03	0.03

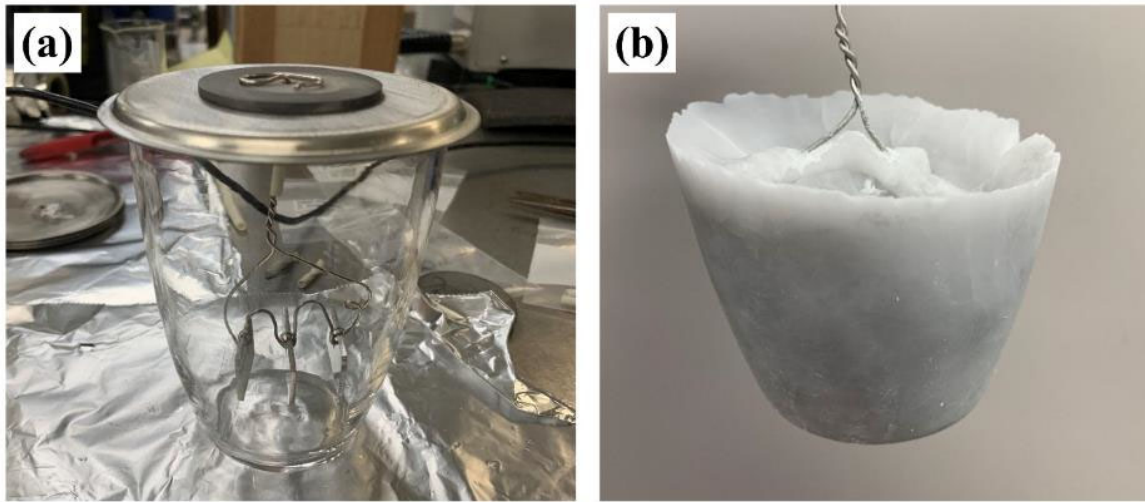


Figure 12. (a) Photograph of H230 samples mounted on a Ni lid and placed inside a quartz crucible; (b) image of the post-test solidified salt.

The average corrosion rate calculated from the first trial was $80.0 \pm 4.7 \mu\text{m}/\text{yr}$. This rate represents an approximately 80% increase from the $44.7 \pm 11.0 \mu\text{m}/\text{yr}$ value observed in previous tests. Shown in Figure 13 are the elemental maps obtained for sample H230-G3-SRC-23, which displayed a corrosion rate of $82.1 \mu\text{m}/\text{yr}$. In addition to the Cr depletion region near the surface of the sample, evidence of grain boundary attack is apparent in the Cr elemental map. Given that a significant increase in the corrosion rate was also observed in tests conducted by NREL (average rate of $249.2 \pm 23.2 \mu\text{m}/\text{yr}$ compared to $39.8 \pm 12.1 \mu\text{m}/\text{yr}$ in previous tests), a thorough examination of possible factors leading to a rise in corrosion rates with the modified protocol would be beneficial. To quantify the extent of Cr depletion, line and point scans were obtained for the post-test H230 coupons. Shown in Table 11 are the average results from 8 line scans acquired at different locations of specimen H230-G3-SRC-23. Here, the mean bulk Cr content for each line scan was derived from regions of constant Cr concentration near the interior. The point at which the Cr concentration decreased by more than three standard deviations from the mean was defined as the maximum depth of the Cr depletion layer. For sample H230-G3-SRC-23, the Cr depletion depth was found to be $24.7 \pm 6.9 \mu\text{m}$. By comparison, specimen H230-G3-SRC-17, which displayed the highest corrosion rate of any tested sample ($53.7 \mu\text{m}/\text{yr}$) in the previous round of Chloride Collective trials, was observed to have a Cr depletion depth of $19.6 \mu\text{m}$.

Point scan data obtained at different locations on the surface of H230-G3-SRC-23 are shown in Figure 14; elemental concentrations acquired for pristine H230 are provided for reference. When compared to untested H230, the Cr content at the surface of H230-G3-SRC-23 decreased by almost 74%.

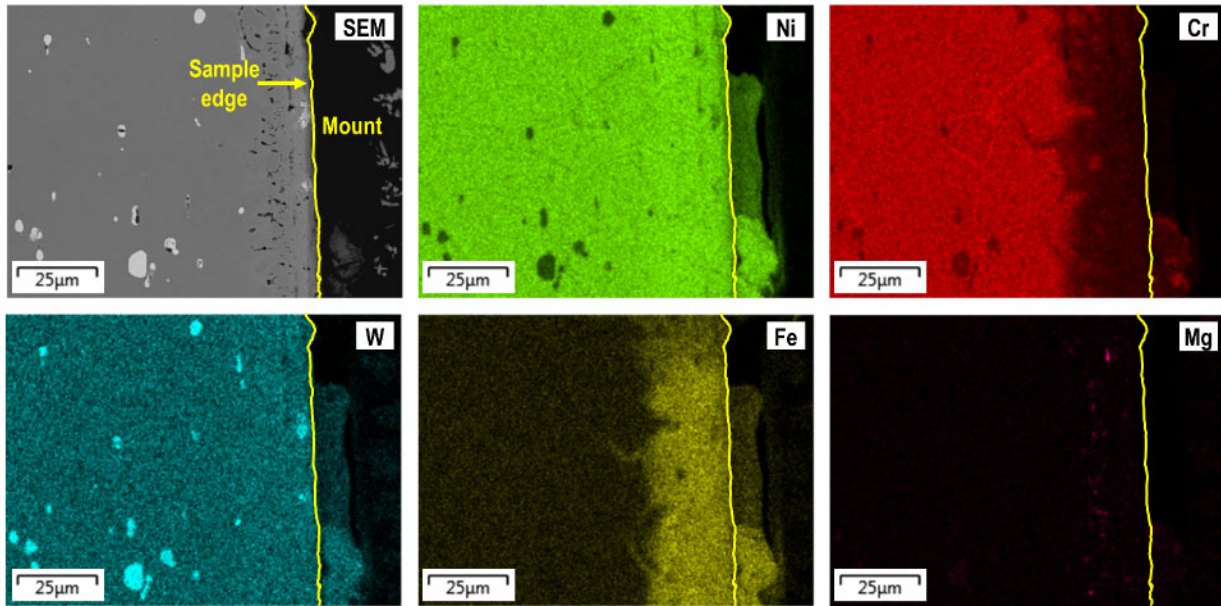


Figure 13. Cross-sectional elemental maps obtained for H230-G3-SRC-23 after corrosion testing at 800 °C for 100 h.

Table 11. Averaged results from 8 line scans to determine the Cr depletion depth

H230-G3-SRC-23: Corrosion Rate = 82.1 μm/yr	
Parameter	Value
Bulk Cr content (at%)	26.7
SD: Bulk Cr content (at%)	0.3
*Cr depletion depth (μm)	24.7
SD: Cr depletion depth (μm)	6.9

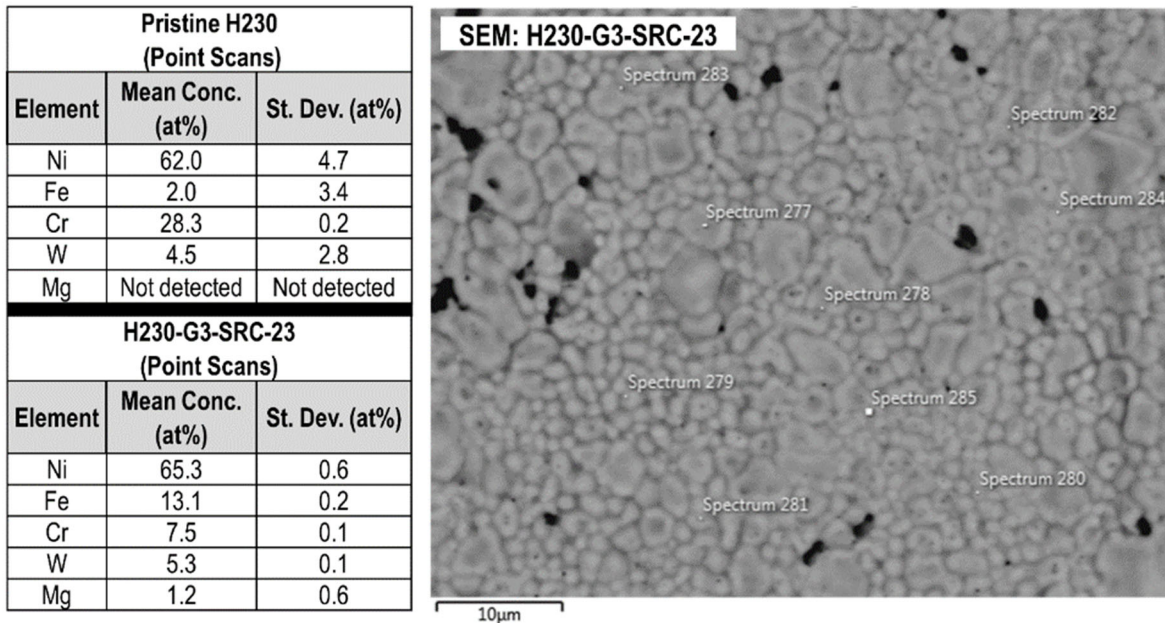


Figure 14. Point scans and SEM image acquired at the surface of H230-G3-SRC-23.

Experiments were conducted to elucidate the cause of the corrosion rate increase from an average of $44.7 \pm 11.0 \mu\text{m}/\text{yr}$ to $80.0 \pm 4.7 \mu\text{m}/\text{yr}$. The changes implemented for the salt treatment and immersion experiments included: 1) the use of an anhydrous carnallite-halite mixture as the molten salt, 2) the employment of a single-step thermal/chemical purification process utilizing a lower quantity of Mg (0.25 wt% vs. 1.7 wt% in prior procedures), 3) a lower peak temperature of 670 °C for the thermal/chemical treatment, and 4) the specification of a quartz crucible as the containment vessel for both salt purification and immersion testing. To ascertain the effects of the purification/testing containment material, corrosion tests were conducted with H230 specimens immersed in purified AC + halite purified in either a quartz vessel or pyrolytic boron nitride (PBN) crucible. Both sets of tests were carried out at 800 °C for 100 h in Ni and quartz crucibles.

The results of the corrosion tests are provided in Figure 15; the lowest average corrosion rate was obtained with samples contained in a Ni crucible and exposed to salt purified in PBN. According to the t-test data, there is a statistically significant difference only between the corrosion rates from the PBN/Ni experiment and that from the PBN/quartz

Purification: Quartz Corrosion Test: Quartz		Purification: Quartz Corrosion Test: Ni		Purification: PBN Corrosion Test: Quartz		Purification: PBN Corrosion Test: Ni	
Sample ID	CR ($\mu\text{m}/\text{y}$)						
H230-G3-SRC-Q1	123.2	H230-G3-SRC-Q4	98.9	H230-G3-SRC-Ni4	118.8	H230-G3-SRC-Ni1	63.5
H230-G3-SRC-Q2	90.3	H230-G3-SRC-Q5	108.7	H230-G3-SRC-Ni5	96.0	H230-G3-SRC-Ni2	59.1
H230-G3-SRC-Q3	82.6	H230-G3-SRC-Q6	146.1	H230-G3-SRC-Ni6	104.1	H230-G3-SRC-Ni3	63.8
Average ($\mu\text{m}/\text{y}$):	98.7	Average ($\mu\text{m}/\text{y}$):	117.9	Average ($\mu\text{m}/\text{y}$):	106.3	Average ($\mu\text{m}/\text{y}$):	62.1
St. Dev. ($\mu\text{m}/\text{y}$):	21.6	St. Dev. ($\mu\text{m}/\text{y}$):	24.9	St. Dev. ($\mu\text{m}/\text{y}$):	11.6	St. Dev. ($\mu\text{m}/\text{y}$):	2.6

		Quartz		PBN	
Test		Quartz	Ni	Quartz	Ni
Quartz	Quartz	98.7 \pm 43.1	37.10%	62.72%	9.69%
	Ni		117.9 \pm 49.8	52.04%	5.90%
PBN	Quartz			106.3 \pm 23.1	1.80%
	Ni				62.1 \pm 5.3

Gray cells in diagonal: average corrosion rate ($\mu\text{m}/\text{yr}$) \pm 2 σ

Red cells: $p < 5\%$ means that the difference in compared values is statistically significant

Green cells: $p > 5\%$ means that the difference in compared values is not statistically significant

Figure 15. Corrosion rates (top) and t-test results (bottom) from H230 samples immersed in Ni or quartz crucibles with salt purified in either quartz or PBN vessels.

test. However, there is a possibility that the use of a quartz crucible during salt purification and/or corrosion testing may drive the formation of various compounds that partially negate weight losses due to Cr depletion. In previous corrosion research conducted with molten chlorides salt, it has been suggested that SiO_2 may react with KCl-MgCl_2 to produce oxidants that can attack alloys [7].

EDX analysis was performed on representative samples to ascertain composition and the extent of Cr depletion. Shown in Figure 16(a) and (b) are elemental maps acquired for samples H230-G3-SRC-Q2 (purification/testing in quartz) and H230-G3-SRC-Ni2 (salt purified in PBN, sample tested in Ni), respectively. From a visual inspection of Figure 16, it appears that the depth of Cr depletion is greater for sample H230-G3-SRC-Q2. This was confirmed from line scan data (Figure 17), where the Cr depletion depths calculated for H230-G3-SRC-Q2 and H230-G3-SRC-Ni2 were $33.4 \pm 5.4 \mu\text{m}$ and $25.4 \pm 3.9 \mu\text{m}$, respectively. According to a t-test carried out for a comparison, there is a statistically significant difference in the calculated Cr depletion depth averages ($p = 1.44\%$). Such a result suggests the possibility that mass loss due to Cr depletion may be “masked” to some extent by the formation of certain compounds due to reactions between the H230 and salt/crucible constituents. Furthermore, a comparison of the elemental maps acquired for Fe in Figure 16 show a higher concentration of this element over a larger area near the edge of H230-G3-SRC-Q2. This could be ascribed to an increase in the degree of Cr loss in the near-edge region, as Fe would then represent a greater proportion of the total composition.

SEM images taken in backscatter mode for samples H230-G3-SRC-Q2 and H230-G3-SRC-Ni2 revealed the existence of dark, irregularly-shaped areas across the surfaces of both specimens. The SEM images and elemental maps of Ni, Mg, and O for H230-G3-SRC-Q2 and H230-G3-SRC-Ni2 are displayed in Figure 18(a) and (b), respectively. It is evident from the figure that the darker regions are composed mainly of Mg and O. To better assess the composition within these areas, multiple surface point scans were

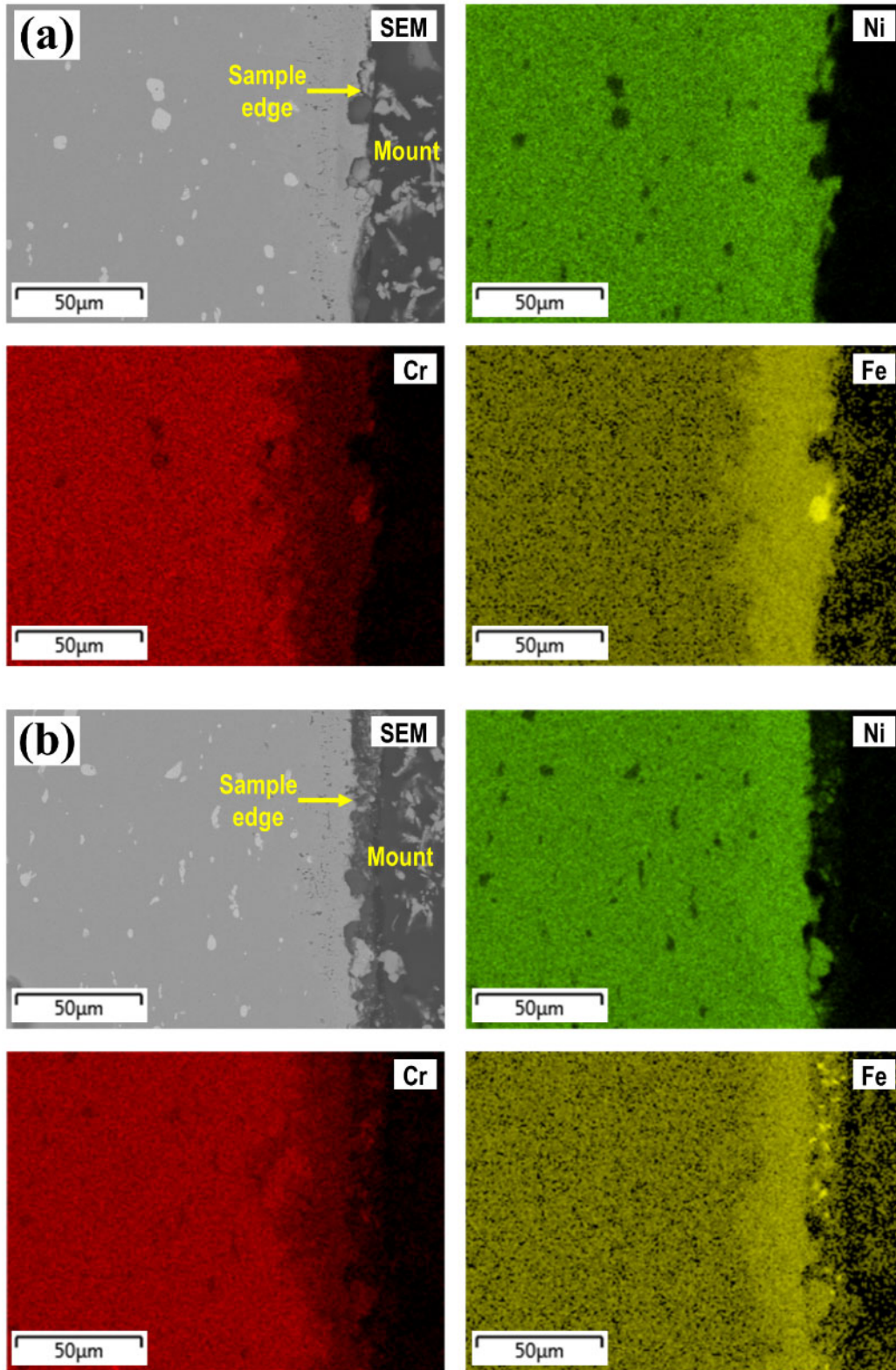


Figure 16. Elemental maps obtained for (a) H230-G3-SRC-Q2 tested in quartz and (b) H230-G3-SRC-Ni2 tested in Ni.

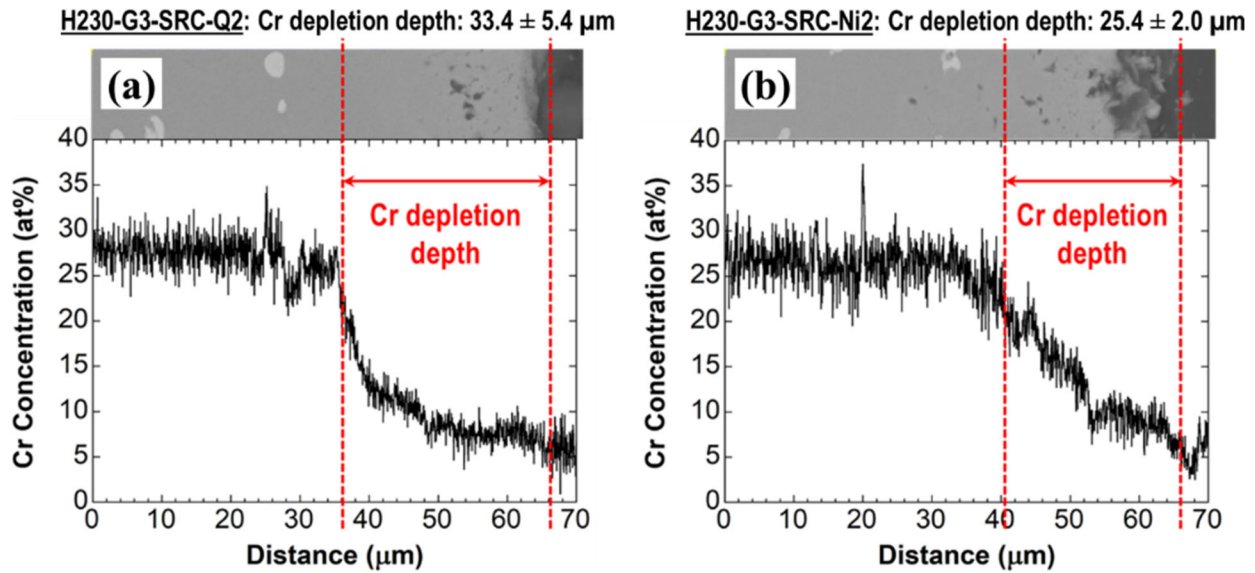


Figure 17. Line scan data obtained for (a) H230-G3-SRC-Q2 and (b) H230-G3-SRC-Ni2. obtained for each specimen; the results are provided in Figure 19. As displayed in the figure, the darker regions (point scans 1 – 5 in Figure 19) have a composition consistent with MgO. The derived Mg:O ratio for samples H230-G3-SRC-Q2 and H230-G3-SRC-Ni2 differ from that of MgO by approximately 6.2% and 0.2%, respectively. One possible explanation for the presence of MgO could be related to the use of a quartz crucible during the salt purification and testing procedures. In such a scenario, the SiO_2 containment vessel could provide a source of oxygen ions, which may serve to enhance corrosion and facilitate the formation of Mg-O compounds. Compositional data were also acquired at locations outside of the darker areas (scans 6 – 8 in Figure 19). It was found that the average Cr content at the surface of H230-G3-SRC-Ni2 ($10.0 \pm 0.2 \text{ at}\%$) was approximately 43% higher than that observed for H230-G3-SRC-Q2. This is consistent with the both the elemental mapping and line scan analysis shown in Figure 16 and Figure 17, respectively.

An additional immersion test was carried out to examine a worst-case scenario whereby no Mg chemical treatment was implemented during the salt treatment process. Here, a batch of dehydrated carnallite was thermally purified in a PBN crucible following the previous treatment protocols issued on June 2018. However, the stage involving Mg addition and subsequent heating was not performed. The resulting salt was then used in an $800 \text{ }^\circ\text{C}/100 \text{ h}$ corrosion test of H230 in a Ni crucible; the data were compared to that obtained in a Ni crucible test with thermally/chemically salt (PBN crucible) from the same batch.

The average corrosion rate of H230 with thermally purified carnallite was $722.2 \pm 23.2 \mu\text{m}/\text{yr}$, an approximately 810% increase from the $79.4 \pm 6.1 \mu\text{m}/\text{yr}$ obtained with dehydrated carnallite subjected to both a thermal and chemical treatment.

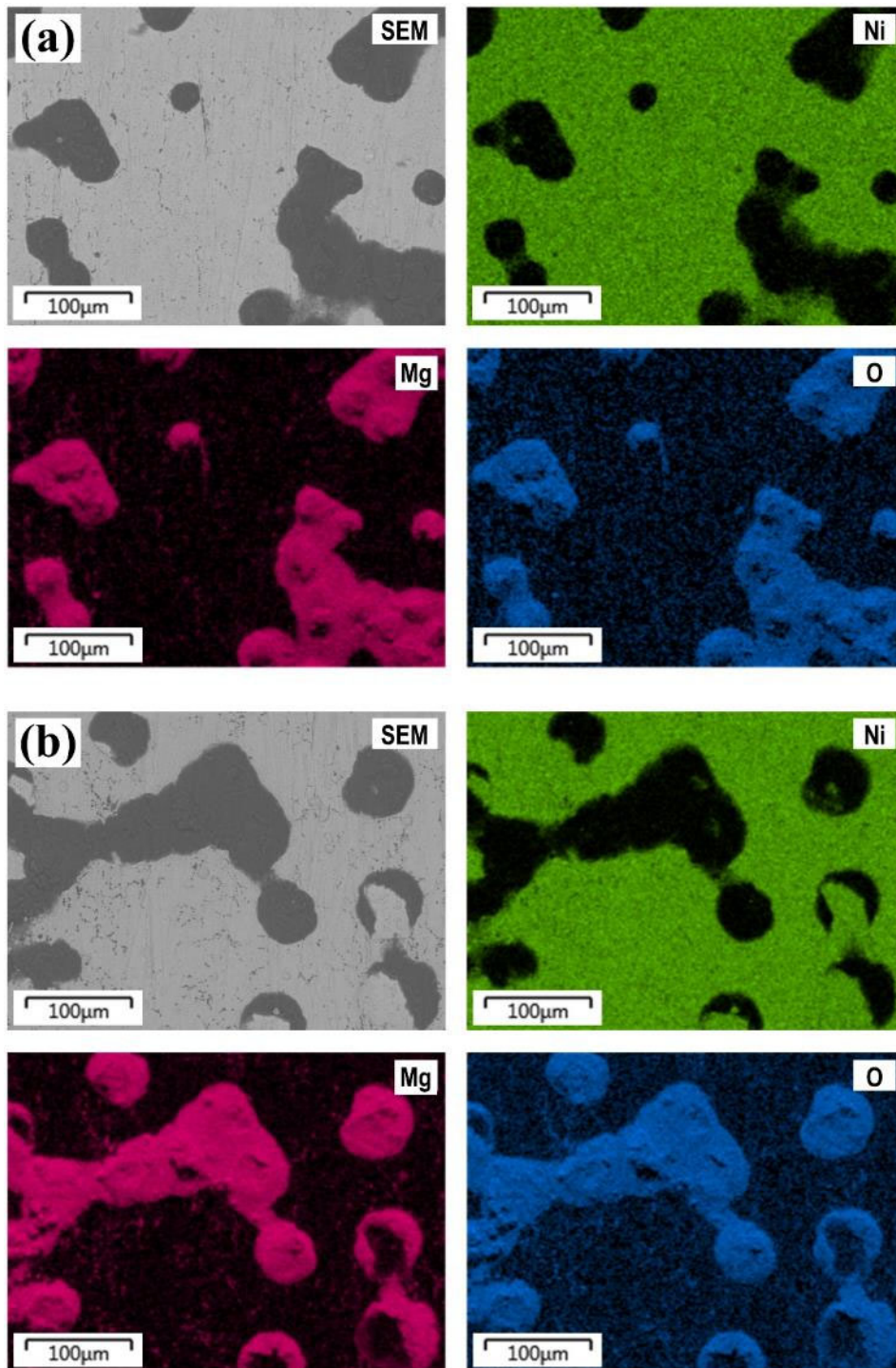


Figure 18. Elemental maps obtained at the surface of (a) H230-G3-SRC-Q2 and (b) H230-G3-SRC-Ni2.

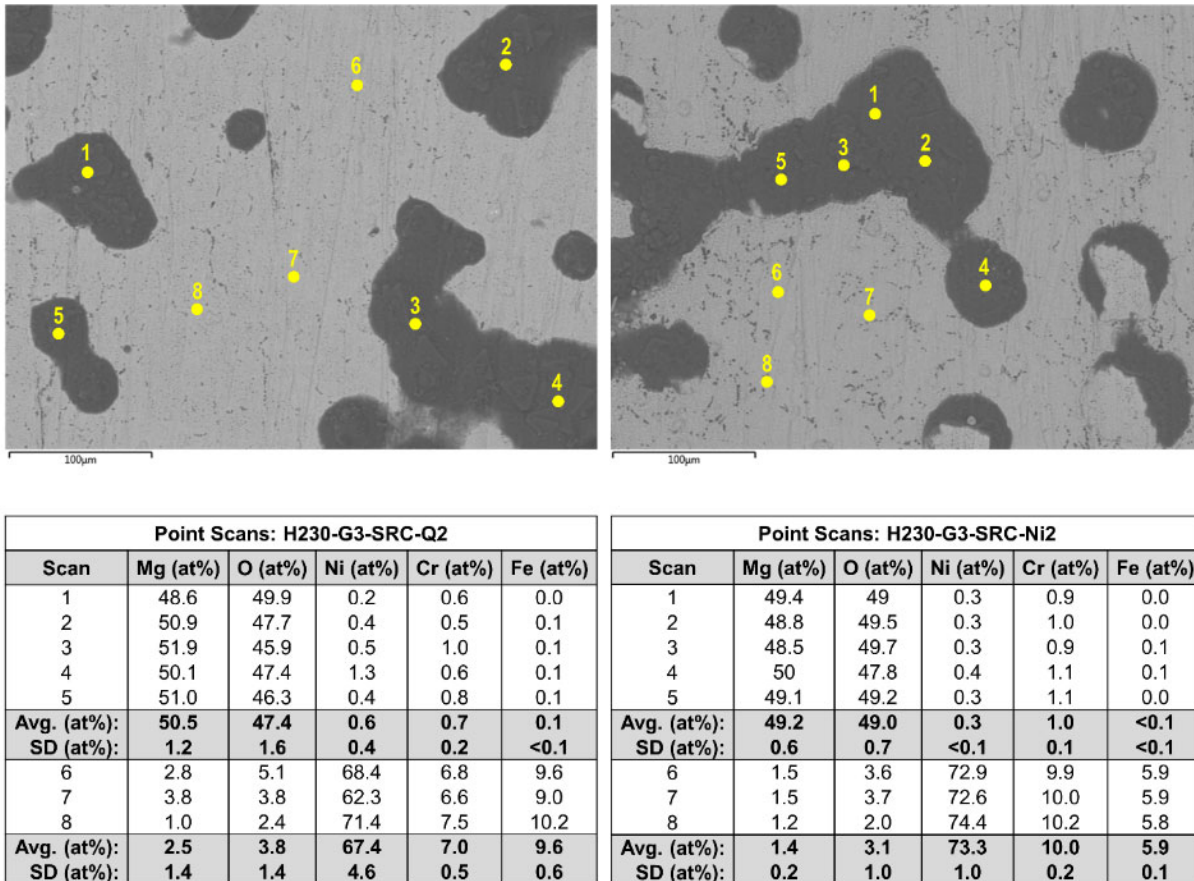


Figure 19. Point scan locations and data acquired for samples H230-G3-SRC-Q2 (left) and H230-G3-SRC-Ni2 (right).

Elemental maps acquired for H230-G3-SRC-T1 (corrosion rate of 722.5 $\mu\text{m}/\text{yr}$), a representative sample from the thermally purified salt, and H230-G3-SRC-TC1 (corrosion rate of 82.5 $\mu\text{m}/\text{yr}$), taken from the thermally/purified salt test, are displayed in Figure 20(a) and (b), respectively. Extensive Cr depletion from grain boundaries and the near-surface region are quite apparent for H230-G3-SRC-T1. Line scan analyses of H230-G3-SRC-T1 and H230-G3-SRC-TC1 (Figure 21) revealed Cr depletion depths of $48.9 \pm 9.9 \mu\text{m}$ and $13.2 \pm 1.4 \mu\text{m}$, respectively. Such a difference was found to be statistically significant ($p = 0.56\%$) according to the results of a t-test.

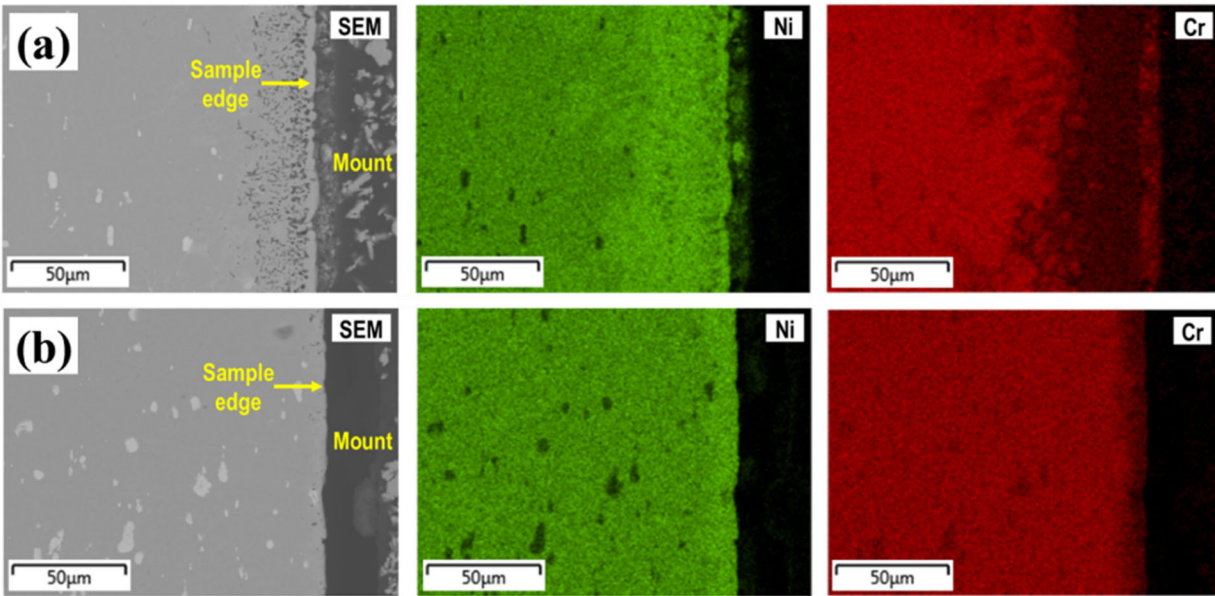


Figure 20. Elemental maps acquired for (a) H230-G3-SRC-T1 (corrosion rate of 722.5 $\mu\text{m}/\text{yr}$) from thermally purified salt and (b) H230-G3-SRC-TC1 (corrosion rate of 82.5 $\mu\text{m}/\text{yr}$) from thermally/chemically purified salt.

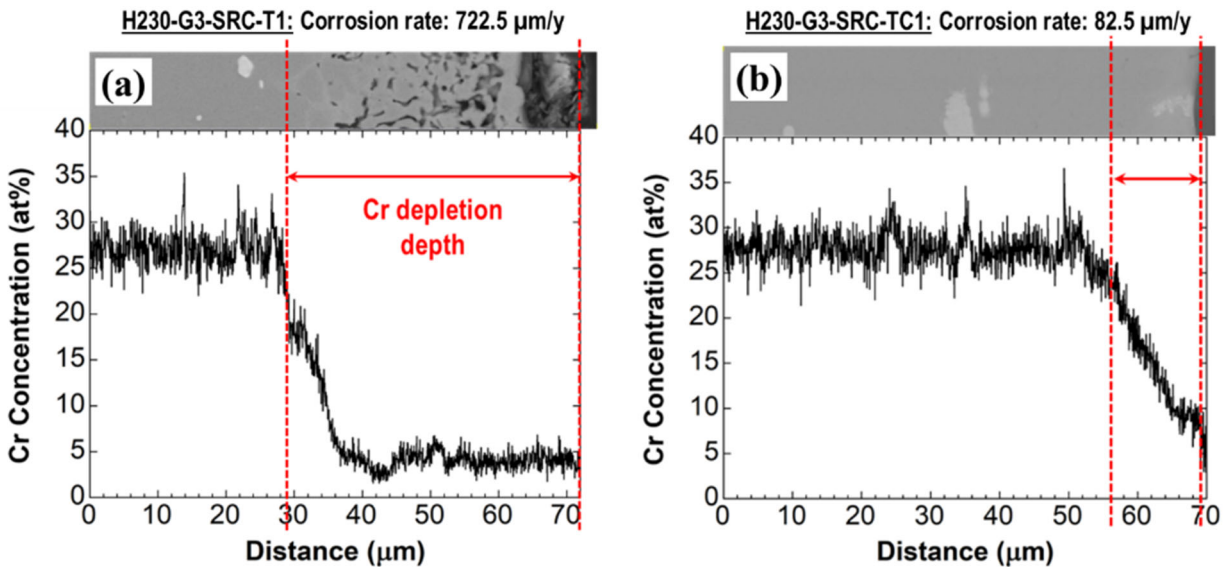


Figure 21. Line scans obtained for (a) H230-G3-SRC-T1 and (b) H230-G3-SRC-TC1.

Task 1.0: Exchange of Samples and Data with Project Cohorts

As part of the Chloride Collective, procedures and guidelines have been defined for performing corrosion testing of H230 as described in Task 0.0. Results from tests conducted at SRNL were compared with relevant results from previous projects and current findings from different trials. Furthermore, data were compared with those obtained by other project teams.

The SRNL tests addressed several experimental factors, including sample mounting, number of samples tested per crucible, test temperature, and the salt used for testing; the results are summarized in Figure 22. Corrosion tests from the previous projects employed Ni wire for sample mounting and were performed using pure and commercial MgCl₂-KCl salts as well as dehydrated carnallite. No statistical difference in the results was observed for this group [1]. However, the plot in Figure 22 implies significant (statistical and practical) differences among the findings when other factors are considered. The more significant issue concerns the manner in which the specimens are mounted. Considering the corrosion rates derived from tests in dehydrated carnallite at 800 °C with 3 coupons per crucible, the results acquired with the Al₂O₃ tube mount versus those for the Ni wire mount are statistically different at the 5% significance level. As shown in Figure 23(a), the rates observed with Ni wire are statistically higher than those obtained with the Al₂O₃ tube mount. There is also an indication that mounting of the specimens with Ni wire leads to greater variation in the corrosion rate when compared to the use of Al₂O₃ tube mounts; this can be seen in the residual calculations displayed in Figure 23(b). A similar

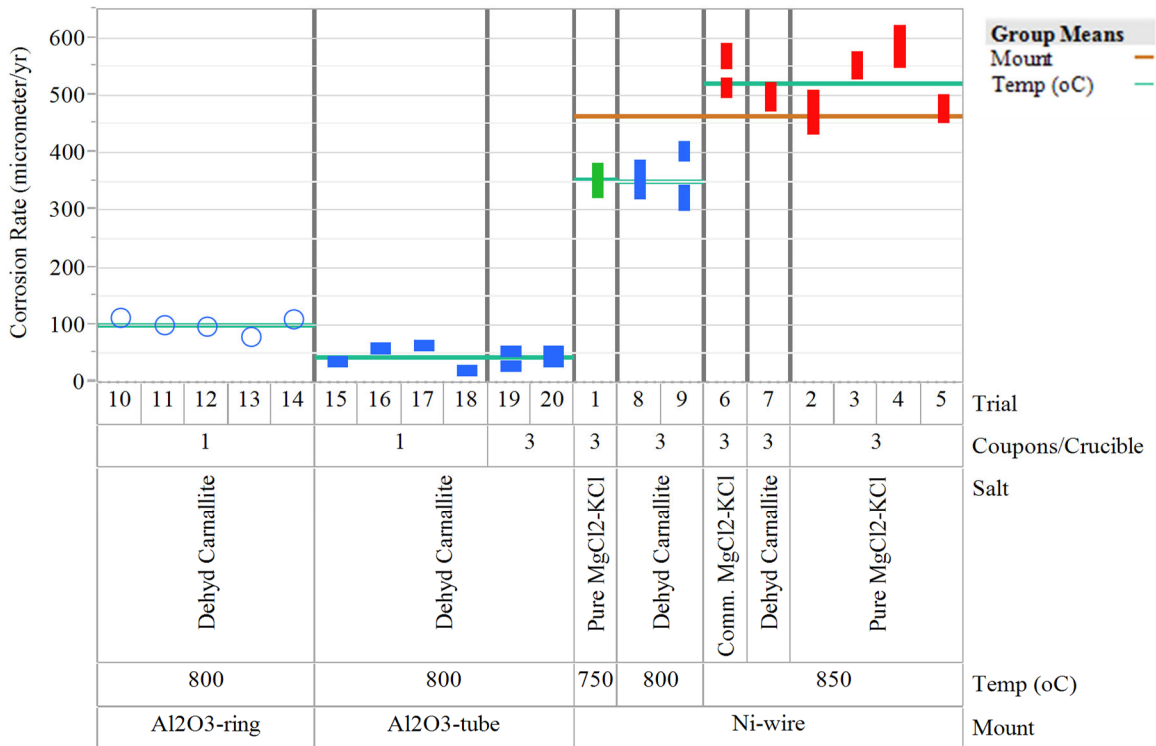


Figure 22. Corrosion rate comparisons for SRNL testing involving several factors.

comparison was performed for corrosion tests with 1 coupon per crucible in dehydrated carnallite at 800 °C using Al₂O₃ ring and Al₂O₃ tube mounts; the findings are presented in Figure 24. The test of the null hypothesis of equal variances for each separate group cannot be rejected at the 5% significance level and thus, there is no indication of a difference in variances. However, there is a statistically significant difference in the mean rates of the two mounts; the Al₂O₃ ring yields a statistically higher mean rate than that obtained with Al₂O₃ tube mount.

In terms of a comparison between trials for SRNL tests conducted with 3 coupons per crucible (trials 19 and 20 in Figure 22), there is no indication of a statistically significant difference in the variances or means (at a 5% significance level), as shown in Figure 25(a). When comparing the tests with 3 coupons per crucible versus those with 1 coupon per crucible (Figure 25(b)), the test of the null hypothesis of equal variances would be rejected at a significance level just over 5%, as the 1 coupon per crucible rates exhibit

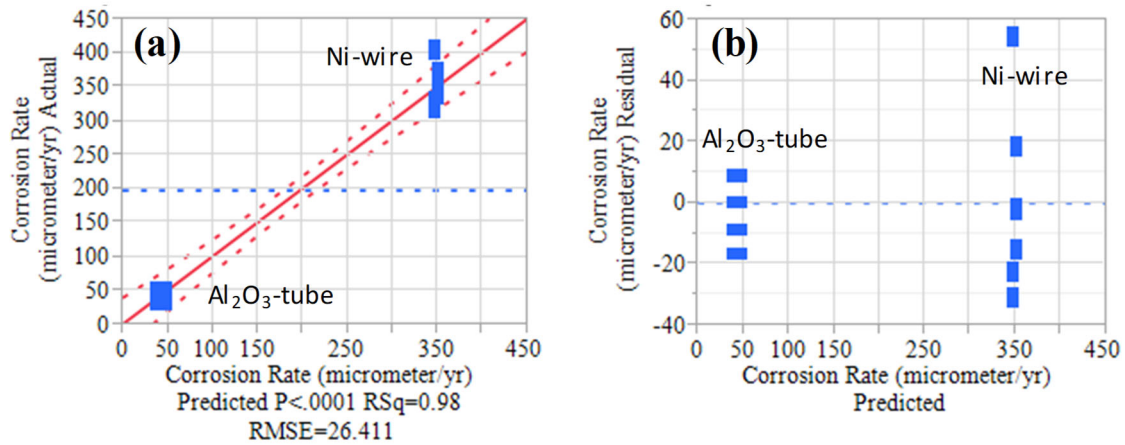


Figure 23. Comparison of the corrosion rate obtained with Al₂O₃ tubing and Ni wire: (a) actual vs predicted and (b) residuals from the predicted plot.

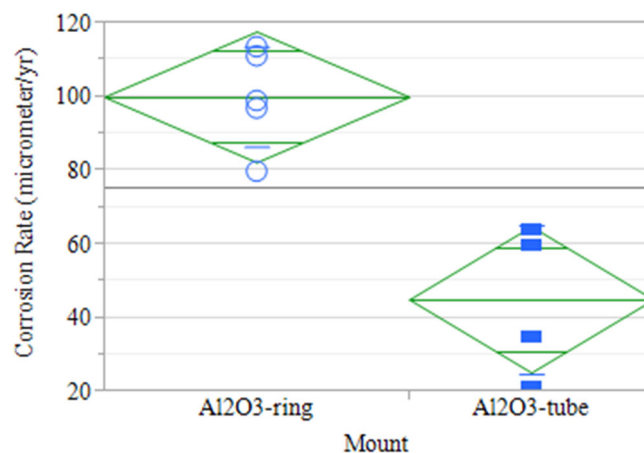


Figure 24. Comparison of the corrosion rates observed when using Al₂O₃ ring and Al₂O₃ tube mounts.

more variation than their 3 coupon per crucible counterparts. While there may be a difference in variances, there is no indication of a statistically significant difference in the mean rates of the two testing conditions; both yield a mean rate at $\sim 45 \mu\text{m}/\text{yr}$. Finally, a comparison of results between project teams is shown in Figure 26. Here, the data from ORNL) was not included because they reported weight gain in their tests. However, results from the 3 coupons per crucible test reported by NREL and SRNL were compared. The test of the null hypothesis of equal variances cannot be rejected at the 5% significance level and thus, there is no indication of a difference in variances. Also, the test of the null hypothesis of equal means cannot be rejected at the 5% significance level and hence, there is no indication of a difference in the mean corrosion rate for these two laboratories.

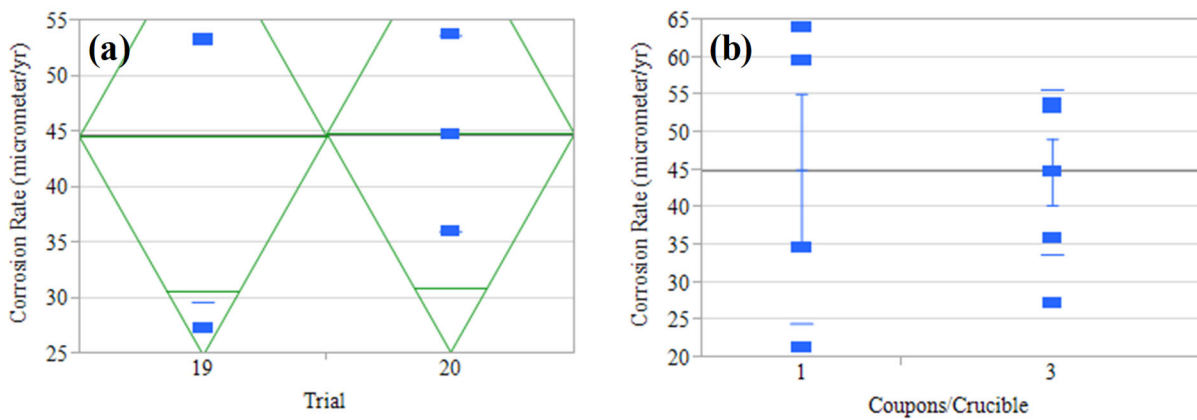


Figure 25. Corrosion rate comparison of SRNL tests carried out with (a) three coupons per crucible and (b) one vs. three coupons per crucible.

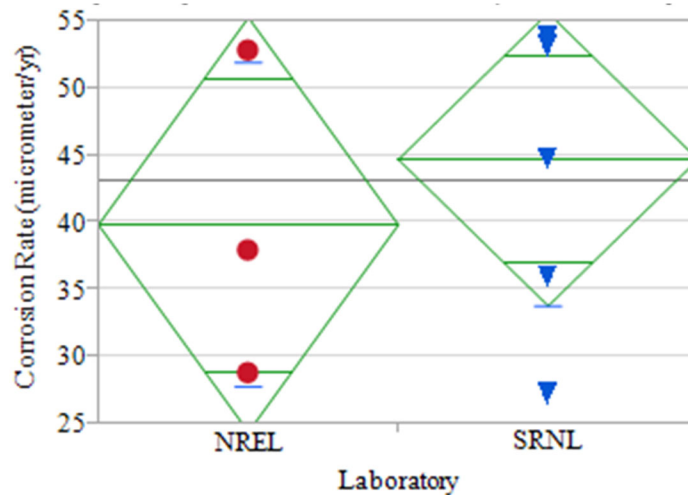


Figure 26. Comparison of the corrosion rates obtained from tests carried out at NREL and SRNL.

Task 2.0: Identify Full Temperature Range for Corrosion Mitigation**Subtask 2.1.1: Identify Full Loop Corrosion Mitigation Methods**

Several approaches have been proposed and investigated for corrosion inhibition. The potential benefits and drawbacks of different corrosion mitigation schemes are given in Table 12. Chlorinating compounds such as CCl_4 and HCl have been employed in previous work to minimize corrosion by eliminating moisture and impurities [8, 9]. However, the use of CCl_4 may produce extremely toxic phosgene as a byproduct [10]. Impurities may also be removed with active metal additives such as Mg or Zr. For carnallite, this strategy may be particularly advantageous in that Mg is already present and thus, the number of different chemical species in the salt is minimized. While the low cost and buffering ability

Table 12. Advantages and disadvantages of various corrosion mitigation strategies.

Strategy	Advantages	Disadvantages
Salt purification using chlorinating compounds (e.g., CCl_4 , HCl)	<ul style="list-style-type: none"> Well-established and extensively studied procedures Demonstrated effectiveness for removing certain oxides in chloride salts 	<ul style="list-style-type: none"> May produce highly toxic byproducts Can increase corrosivity of salt, requiring metal addition Systems to remove offgas Cl-containing compounds are needed
Salt purification via addition of active metals (e.g. Mg, Zr)	<ul style="list-style-type: none"> Simplicity Minimal production of toxic byproducts Low-cost and abundance of Mg Buffering ability of Mg and Zr Can utilize existing salt components 	<ul style="list-style-type: none"> Possibility of forming eutectic compounds (e.g., Mg_2Ni at 508 °C) Limited effectiveness in salts containing less electronegative cations Potential transport of solidified additives
Electrolytic purification of salt	<ul style="list-style-type: none"> No introduction of additives to salt Minimal operator action needed once electrodes introduced 	<ul style="list-style-type: none"> Mg-Cl recombination Degradation of electrodes: poisoning, direct mechanical or chemical degradation Cl_2 gas removal systems required
Use of reducing gas (e.g., Ar/ H_2 mixture)	<ul style="list-style-type: none"> Allows tailoring of $p\text{O}_2$ level for specific applications Flammability hazards mitigated by use of <5% H_2 gas mixtures 	<ul style="list-style-type: none"> Generation of water vapor Potential to reduce system component materials No buffering ability
Molten salt deposition of corrosion-resistant films	<ul style="list-style-type: none"> Ability to plate non-line-of-sight components Demonstrated effectiveness for corrosion mitigation 	<ul style="list-style-type: none"> System tolerances may be altered if film is not self-limiting Delamination and fracturing of films can occur
Boriding, nitriding, or carburizing	<ul style="list-style-type: none"> Formation of compounds with established corrosion resistance Added benefit of increasing wear resistance Can have limited effect on system tolerances due to low solubility of C and N in Ni 	<ul style="list-style-type: none"> Requires salt additives that will affect chemical properties High toxicity of techniques involving gaseous species for compound formation

of Mg provide further benefits, issues related to solidification and the formation of eutectic compounds with system components must be addressed. Electrolytic salt purification, can be considered a more passive technique that requires a lower degree of operator action when compared to other schemes. In the case of carnallite, an added advantage is that an element already present in the salt is exploited to remove impurities. One drawback is the recombination of cationic species with Cl_2 . Molten salt can be utilized for mass transport and the subsequent formation of corrosion mitigating films. Although the ability to coat non-line-of-sight components is attractive, system tolerances can possibly be compromised, and fracturing or delamination of the films may occur.

A variety of electrochemical characterizations were tested to identify electrochemical responses from species that can be used for quantification of concentrations in the molten salt. Cyclic voltammetry (CV) is widely utilized by electrochemists to qualitatively survey where electrochemical reactions occur in an electrolyte as well as to provide an estimate of the order of magnitude for the reaction. CVs were performed on the salt while starting purification by inserting a magnesium rod that was not used as an electrode. The magnesium rod should react with MgOHCl in the salt and be consumed with time. CV scans with time should be able to detect changes in the concentration of MgOHCl . As an initial test, CVs were performed using tungsten working and counter electrodes along with a Mg reference electrode. The scan rate was 20 mV/s between -0.001 V and 1.6 V. For electrochemical experiments, the lower bound for the CV was adjusted to limit Mg oxidation and reduction on the electrode.

Figure 27 shows the first 6 CV cycles after immersion of the Mg rods and tungsten electrodes into the purified carnallite at 600 °C. The reduction reaction for MgOHCl is given by:

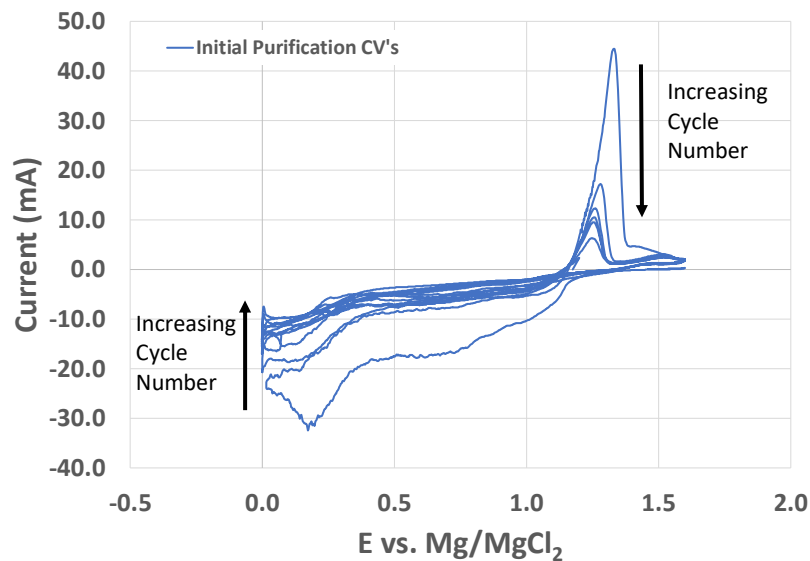
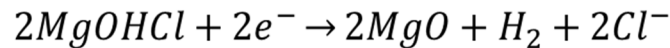


Figure 27. Cyclic voltammograms at the start of purification with Mg rod immersed in the molten salt.

Calculations at 600 °C indicated that the equilibrium voltage for this reaction is 1.621 V vs. Mg/MgCl₂. Large cathodic currents were observed below 1.2 V and likely are due to this reduction reaction. The cathodic current stays relatively stable down to -0.5 V where reactions related to Mg oxidation and reduction become more pronounced. At potentials above 1.2 V, there is an oxidation peak. This peak is likely due to adsorption of MgOHCl with the electrode surface. Both the oxidation peak and the reduction current decrease rapidly at the start of purification. The decrease in current is likely due to the consumption of MgOHCl through reaction with the Mg rod. After the first 4 hours, the peak and reduction current continued decreasing at a slower rate. Galvanic purification was then utilized to remove impurities from the salt as was performed in the previous quarter and that was able to eliminate corrosion in the purified carnallite. After purification, the CV became centered about 0 A and the capacitive component of the current increased.

Figure 28 shows a comparison of the CVs from early purification and after galvanic purification. The peak at 1.2 V and reduction current can be distinguished, but is near the peak of the after purification salt. The reduction current even on the positive scan is also still evident in the early scan, but is in the middle of the currents from the forward and reverse scans.

Although CV can be utilized in some applications for quantification, it can be limited because it does not separate double-layer charging effects from faradaic reactions. Square-wave voltammetry (SWV) is a method to remove double layer capacitance currents and focus on faradaic reactions. SWV and related methods such as AC voltammetry are currently in testing to determine the best method for quantification.

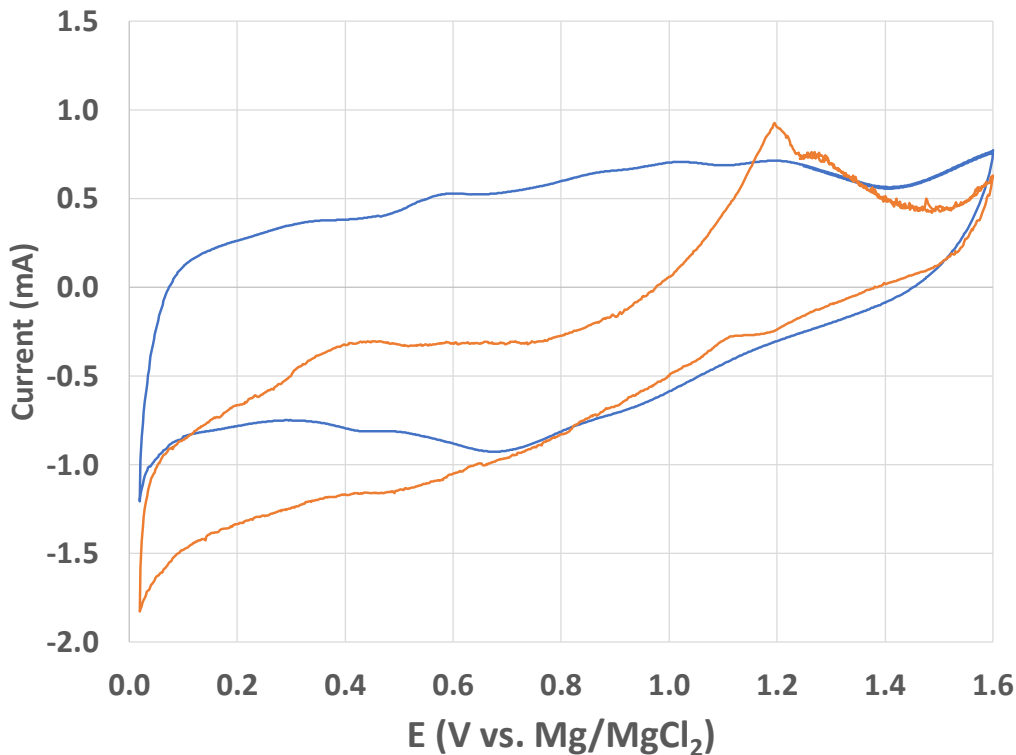


Figure 28. Comparison of CVs from early purification and after galvanic purification.

Subtask 2.1.2: Evaluate the Use of Self-Healing Coatings as Corrosion Inhibitors

The primary objective of this subtask was to investigate a range of active metals (e.g., Zr, Ti, Nb, Ta) as viable corrosion inhibitors for molten salt heat transfer loops. Among the candidates for corrosion mitigation, Zr was selected for use in initial experiments. In previous research conducted at SRNL, H230 specimens were immersed in KCl-MgCl₂ salt containing Zr and subsequently heated at 850 °C for 100 h [11]. Based on SEM imaging and EDX analysis of sample cross-sections, a so-called “affected zone” composed of two distinct regions was identified. The first region, which is adjacent to the bulk material and marks the maximum depth of the affected zone, is nearly devoid of Ni and is characterized by Cr-W precipitates situated in a matrix consisting almost entirely of Cr. Closer to the sample edge, the Cr content decreases significantly while the concentrations of Ni and Zr exhibit a substantial rise. This second region, which persists up to the edge of the specimen, is composed primarily of Ni and Zr. Both the length of the affected zone and the depth of the Zr/Ni-rich region (i.e., the thickness of the second region) were quantified by determining the points at which the Cr and Zr concentrations increased by more than three standard deviations from their respective bulk values. The analysis revealed affected zone length and Zr rich region depths of 8.79 μm and 5.86 μm, respectively, as measured from the sample surface.

A preliminary experiment was performed with H230 and Zircaloy coupons placed in Ni crucibles and immersed in treated carnallite salt under a 200 – 250 sccm flow of Ar. To both accelerate Zr deposition and examine the growth of Zr layers at extreme temperatures, the Zircaloy coupons and H230 were first sequentially stacked and wrapped in Ni wire; a photograph of the assembly prior to testing is shown in Figure 29. Upon immersion in carnallite, the sealed crucible was heated to 1000 °C for 100 h. Examination of the specimens at the completion of the test revealed partial melting of the constituent materials likely caused by eutectic formation.

After determining an upper temperature boundary for the Zr coating experiments, an additional test was performed at 850 °C for 336 h (2 weeks). 850 °C is about 110 °C below the lowest known Zr-Ni eutectic. Given the earlier work cited above, the results of this test could be used to generate a relationship between time and Zr film thickness at 850 °C. To prevent the possibility of eutectic transformations and melting of the samples, Zircaloy coupons and H230 were separated by W spacers and held together in W wire.



Figure 29. Photograph the Zircaloy-H230 assembly prior to heating at 1000 °C for 100 h.

The weight change measured for both the H230 and Zircaloy coupons after the coating experiment are provided in Table 13. On average, the weight of the Haynes 230 specimens increased by 0.24 g (with a standard deviation less than 0.01 g), while the Zircaloy coupons showed an average weight loss of 2.12 ± 0.2 g.

The morphology and elemental composition of sample H230-G3-SRC-Zr4 in Table 13 were examined via SEM and EDX analyses. The specimen was first cut with a diamond saw and then polished in successive steps down to a 1 μm finish. To prevent charging during the SEM analysis, the sample was mounted in a conductive copper-based resin. Both the SEM images and EDX data were acquired at an accelerating voltage of 25 kV.

Table 13. Weight change data for Haynes 230 and Zircaloy coupons after heating in molten salt at 850 °C for 336 h.

Haynes 230	Pre-test wt. (g)	Post-test wt. (g)	% increase in wt.
H230-G3-SRC-Zr4	4.2583	4.5037	5.7630
H230-G3-SRC-Zr5	4.2599	4.4994	5.6221
H230-G3-SRC-Zr6	4.2666	4.4930	5.3063
Zircaloy	Pre-test wt. (g)	Post-test wt. (g)	% decrease in wt.
Zr-2-13	11.5134	9.5419	17.124
Zr-2-20	11.5927	9.6361	16.878
Zr-2-22	11.6896	9.5588	18.228
Zr-2-28*	11.5492	9.1448	20.819

*In contact with bottom of crucible

Elemental maps acquired at different regions of H230-G3-SRC-Zr4 are shown in Figure 30(a)-(b). Starting from the edge of Figure 30(a), it can be seen that a thick ($>100 \mu\text{m}$) layer of Zr was successfully formed; specifics regarding the Zr diffusion depth are discussed below. Moving inwards towards the bulk of the sample, a decrease in the Ni content along with a rise in both the Cr and W concentrations are observed. The elemental maps in Figure 30(b), which were obtained at the corner of the cross-section, indicate that a relatively uniform layer of Zr can be formed around edges via immersion in molten salt.

Averaged line scan data obtained at 12 separate cross-section locations of H230-G3-SRC-Zr4 suggest the formation of Zr-Ni phases. In a previous study on Ni-Zr diffusion couples, NiZr₂ and NiZr phases were detected in the direction from pure Zr to pristine Ni [12]. From an examination of Zr and Ni line scans (Co, Al, and Fe were also included, but these elements were present in concentrations of less than 2 at%) acquired for H230-G3-SRC-Zr4, the average atomic fraction of Zr in regions within 30 μm of the edge was calculated to be 0.67 (with a standard deviation of less than 0.1), a value that differs from the ideal Zr atomic fraction in NiZr₂ (0.67) by a maximum of 2.2%. Moving closer to the interior of the sample, the average Zr atomic fraction between $72.3 \pm 4.3 \mu\text{m}$ and $92.3 \pm 12.7 \mu\text{m}$ was determined to be 0.53 (with a standard deviation of less than 0.1), which differs from the stoichiometric NiZr value (0.5) by $6.6 \pm 2.3\%$.

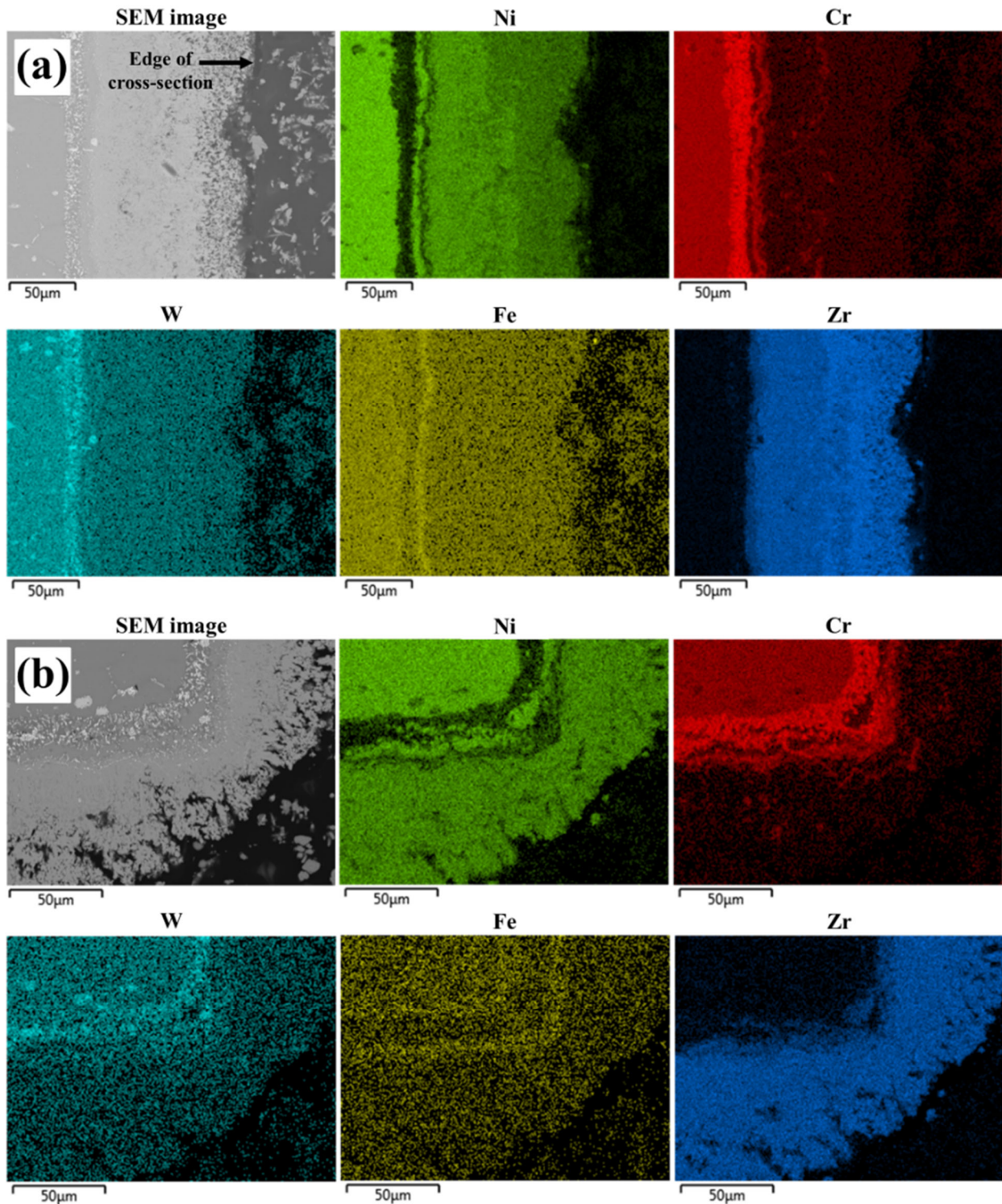


Figure 30. Elemental maps obtained for H230-G3-SRC-Zr4 at (a) the sample edge and (b) at a corner of the cross-section.

Line scans obtained for H230-G3-SRC-Zr4 were also utilized to ascertain the affected zone length and depth of Zr diffusion. Here, the mean Cr and Zr content in the bulk of the material was first calculated. The points at which the Cr and Zr concentrations increased by more than 3 standard deviations from their respective means were then determined. The distance from these points to the edge of the copper mount were defined as the affected zone length and the depth of Zr diffusion. To better illustrate the process, representative Cr and Zr line scans are provided in Figure 31.

A total of 12 line scans were used to calculate the average affected zone length and depth of the Zr-rich region. Each scan consisted of 1500 data points separated by approximately 0.1 μm. The parameters obtained from line scans on sample H230-G3-SRC-Zr4 are provided in **Error! Reference source not found.**

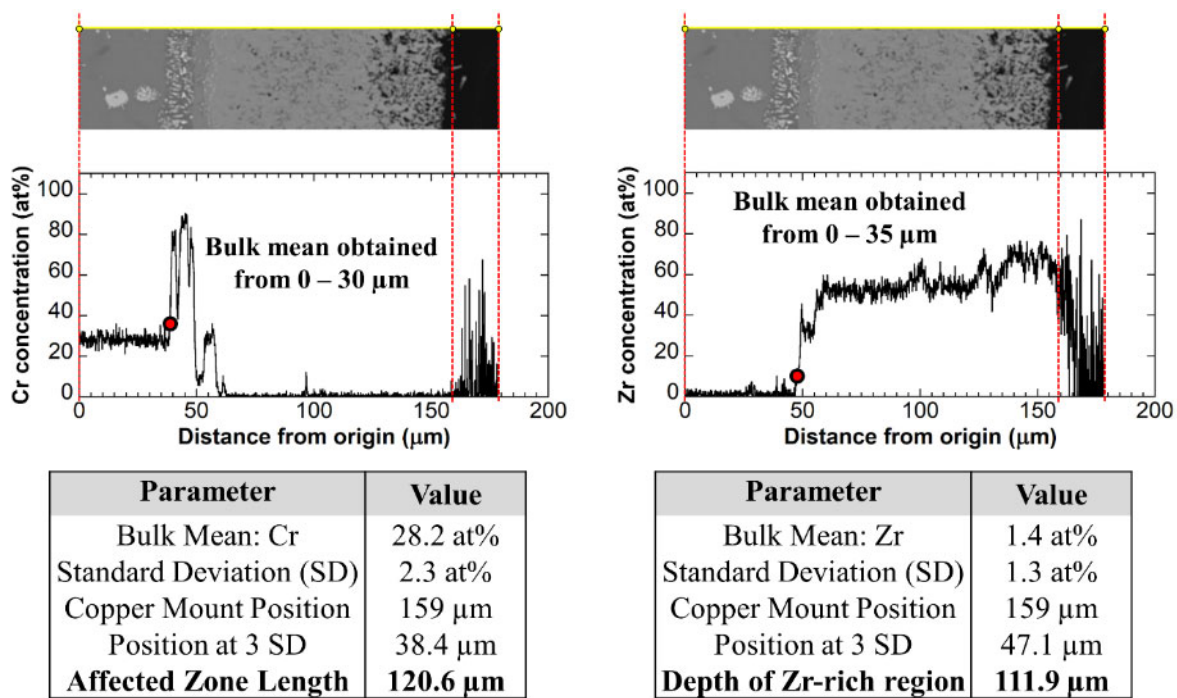


Figure 31. From top to bottom: SEM images showing the line scan position, plots of the Cr and Zr concentrations at different positions on the sample, and tables with the parameters employed to compute the affected zone length and Zr diffusion depth.

Table 14. Data derived from an average of 12 line scans for sample H230-G3-SRC-Zr4 after a Zr coating test at 850 °C for 336 h.

Parameter	Value
Average Bulk Mean: Cr	27.9 at%
Average Standard Deviation (SD)	3.3 at%
Average Affected Zone Length	128.2 μm
Affected Zone Length SD	6.3 μm
Average Bulk Mean: Zr	1.7 at%
Average Standard Deviation (SD)	1.9 at%
Average Depth: Zr-rich Region	113.2 μm
SD: Depth of Zr-rich Region	5.6 μm

To confirm the phases present in Zr-coated H230, XRD patterns were obtained for both pristine H230 and H230 coated with Zr at 850 °C for 336 h; the results are presented in Figure 32. As stated previously, a Zr-rich layer with a thickness of $113.2 \pm 5.6 \mu\text{m}$ was measured under these deposition conditions. The stark difference in the makeup of the patterns suggests that significant attenuation of the X-rays occurred before the photons could reach the underlying H230 substrate of the Zr-coated specimen. Furthermore, the peaks of highest intensity for Zr-coated H230 were indexed to NiZr_2 , while strong peaks of slight less intensity corresponded to NiZr . These findings are in agreement with the aforementioned EDX data.

A portion of the crucible used for the 850 °C/336 h Zr coating test was cut, mounted, and polished for EDX analysis to verify that molten salt containing Zr could be used to condition system components of different alloy types in a full loop heat transfer system. Elemental maps acquired for a coupon of the crucible are shown in **Error! Reference source not found.** As evident in the figure, a Zr layer was formed on the interior of the crucible exposed to molten salt, thereby demonstrating that protective barrier coatings may be deposited on concentrating solar power elements via transport through molten salt.

Among the Zr-coated samples listed in Table 13, H230-G3-SRC-Zr5 was selected for a corrosion test conducted at 800 °C for 100 h under an ambient atmosphere of air (ultra-high purity, flow rate: 200 – 250 sccm). The sample was placed in a pyrolytic boron nitride crucible and immersed in treated carnallite. During the experiment, extensive evaporation of the salt was observed. Due to failure of the primary measurement thermocouple, it was determined that the test, while started at 800 °C, likely reached temperatures as high as ~875 °C. Photographic images of the Inconel vessel after completion of the test and specimen H230-G3-SRC-Zr5 prior to removal from the salt are displayed in Figure 34(a) and (b), respectively. A thick layer of evaporated salt/oxide (yellowish powder in Figure 34(a)) was deposited onto the interior walls of the Incoloy vessel, and condensed powder was observed along the entire length (~15 feet) of exhaust tubing.

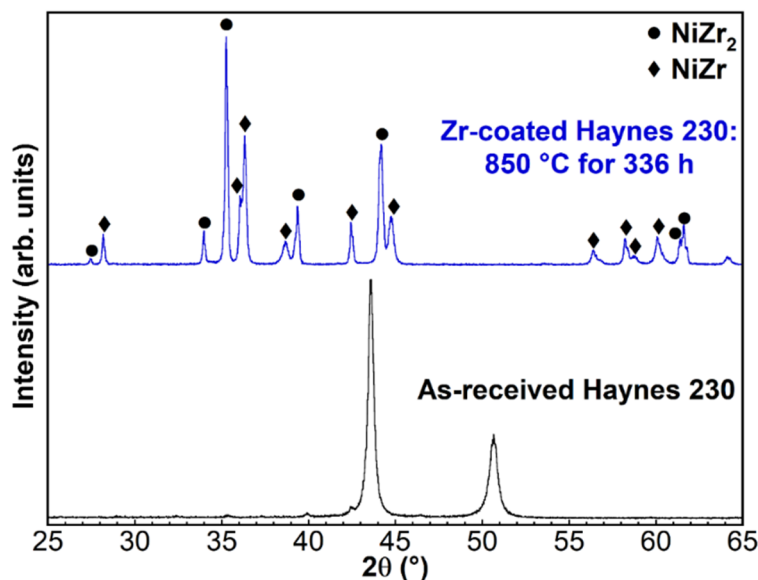


Figure 32. XRD patterns for pristine H230 and H230 coated with Zr at 850 °C for 336 h.

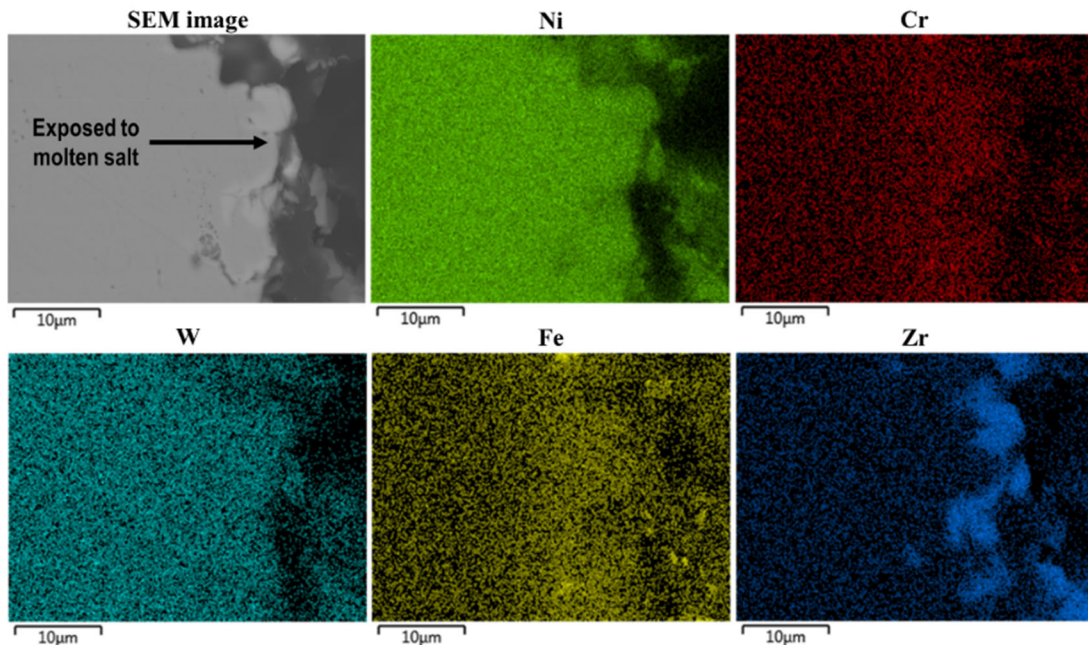


Figure 33. Elemental maps acquired for a coupon of a crucible exposed to molten salt containing Zr; the crucible was utilized in the Zr-coating experiment conducted at 850 °C for 336 h.

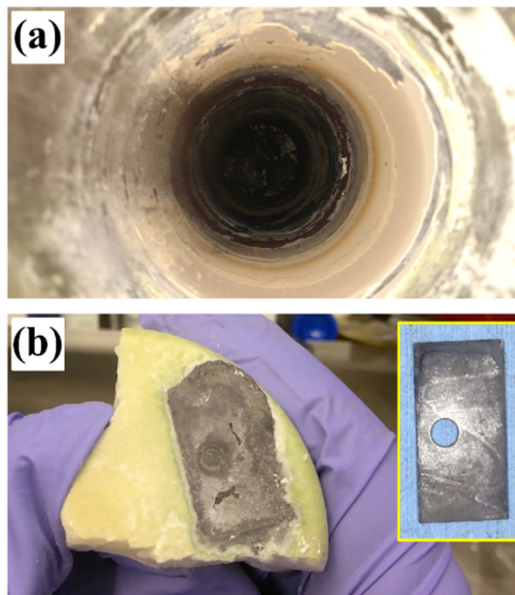


Figure 34. Photographic images of (a) the Incoloy vessel used for the corrosion test conducted in UHP air and (b) sample H230-G3-SRC-Zr5 embedded in salt after removal from the pyrolytic boron nitride crucible; the inset of (b) shows the specimen after sonication in DI water.

During sonication of H230-G3-SRC-Zr5, the DI water employed for the cleaning step turned a light gray; this could be attributed to release of some of the protective Zr coating or coating/carnallite reaction products on the H230 coupon from portions of the carnallite as the salt gradually dissolved. While the mass of the sample after the corrosion test

decreased from 4.4994 to 4.3048 g, the final mass was still greater than that measured before the Zr-coating test (4.2559 g, see Table 13), suggesting Zr was still present on the surface of the specimen.

Elemental maps were obtained for specimen H230-G3-SRC-Zr5 upon completion of the corrosion test; the results are shown in Figure 35. Assuming that the average Zr diffusion depth for H230-G3-SRC-Zr5 was comparable to that of sample H230-G3-SRC-Zr4 prior to the corrosion experiment (believed to be a reasonable assumption given the data provided in Table 13), it appears that the Zr layer thickness decreased over the course of the experiment. Such a finding supports the notion that Zr acts as a sacrificial layer while preventing the release of Cr into the molten salt.

To quantify the Zr loss, cross-sectional line scans were acquired for H230-G3-SRC-Zr5. The average Zr thickness from 6 line scans was $78.4 \pm 5.3 \mu\text{m}$, a decrease of approximately 36% when compared to the Zr coating thickness measured for sample H230-G3-SRC-Zr4.

Given the promising results obtained from the test in air, specimen H230-G3-SRC-Zr6 was subjected to corrosion testing at 800 °C for 100 h under a 200 – 250 sccm flow of Ar. The final mass of the sample, 4.4438 g, was still greater than the mass measured prior to the application of a Zr coating. It is noted that mass transfer from the Zr-coated sample to the uncoated Ni crucible should be expected from this sample, as described earlier during the Zr coating experiment.

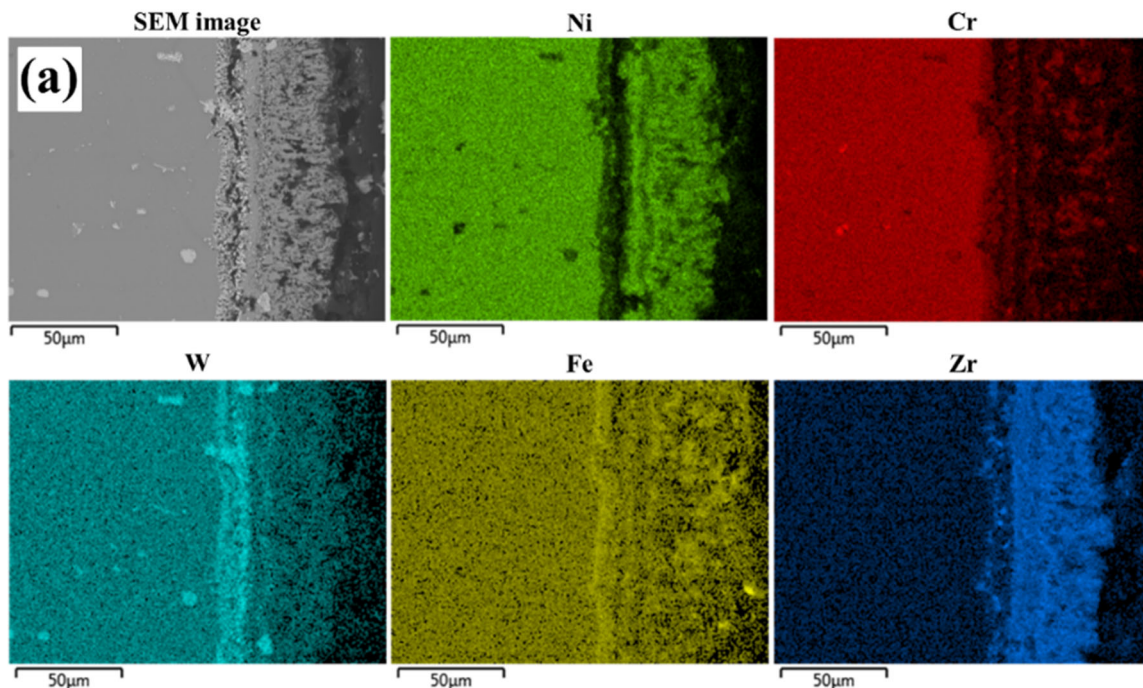


Figure 35. Elemental maps obtained for H230-G3-SRC-Zr5 after heating the sample in ultra-high purity air at 800 °C for 100 h.

To confirm the corrosion mitigation capabilities of Zr film growth on H230, ICP-OES data was obtained on salt samples from the corrosion tests conducted in air and Ar for samples H230-G3-SRC-Zr5 and H230-G3-SRC-Zr6; the results are displayed in Table 15. The content of both Cr and Ni in the post-test salts were found to be below the detectable limits of the instrument.

Table 15. ICP-OES data obtained for salt samples collected after corrosion tests in air and Ar for H230-G3-SRC-Zr5 and H230-G3-SRC-Zr6, respectively.

Salt Sample	Ni	Cr	Fe	Co	Mo	Mn	Ca
H230-G3-SRC-Zr5 (tested in air)	<8.3	<2.6	<1.7	<1.9	<9.1	42.1	863
H230-G3-SRC-Zr6 (tested in Ar)	<6.5	<1.4	<1.4	<1.5	<9.5	<0.2	815

Subtask 2.1.3: Design and test a getter bed for a thermosiphon reactor in collaboration with ORNL

ORNL provided feedback that a getter bed with as little flow resistance as possible was desired due to the low flow and pressure drop of the thermosiphon. To address this request, efforts were focused on a getter rod design. The getter rod design would also minimize loop/getter integration work required by ORNL, in that the rod could simply be attached to a finished loop and inserted through the top. The design of the rod insertion apparatus, a purgeable double-ball valve, was based off earlier work described by ORNL in the literature [13]. A photograph of the constructed getter assembly with the inserted Zr rod is shown in Figure 36(a), while schematics of the Zr getter rod in withdrawn and inserted positions are displayed in Figure 36(b) and (c), respectively.

A length of commercially pure Zr without the Hf component removed was threaded into a longer 304SS rod that can then be passed through two ball valves. After the rod is inserted into the Swagelok fitting, the first ball valve would be opened and the gas space would be purged of air with high purity argon prior to opening the second ball valve and submerging the rod at a set depth. A hose clamp and piece of wire can be used to electrically connect the HARP loop to the Zr rod to provide passive galvanic protection of the HARP loop during the initial Zr dissolution and plating. High temperature valves were obtained that can be operated up to ~426 °C. It is expected that many of the double ball valve connections will be welded at ORNL to prevent air ingress.

Only a part of the total Zr rod length would be inserted in the salt, specifically into the surge tank at the top of the loop hot zone. It is expected that the surge tank will be one of the cooler if not the coldest location on the loop. The Zr rod is about 12 mm in diameter. If 10 cm of the rod was immersed, then the wetted surface area of the rod would be about 40 cm², or about 20 cm² for a 5 cm immersion depth. In previous static Zr coating tests, the 4 Zr coupons used to coat 3 H230 coupons were each about 25 cm² and lost about 0.5 g after ~224 h at 800 °C. Assuming the same weight loss/area, it can be expected that the Zr rod would lose about 0.8 g after ~224 hours if immersed to a depth of 10 cm and half that for 5 cm.

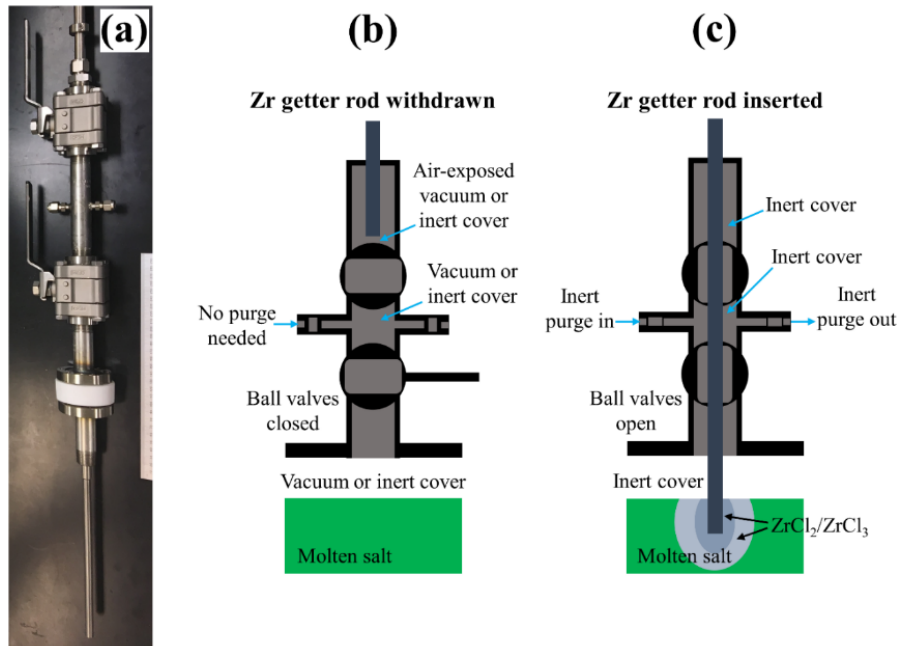


Figure 36. (a) Zr getter rod components and schematics of the Zr getter rod in (b) the withdrawn position and (c) the inserted position.

The actual rate of mass loss will depend on the implementation of the Zr getter rod. It is recommended that the Zr rod be electrically connected to the HARP loop; this will ensure that a galvanic couple is formed. The Zr rod will act as an anode in the galvanic cell, and anodically protect the HARP loop, which will be the cathode. Anodic dissolution could be exacerbated by the large surface area of the HARP loop compared to the small surface area of the wetted Zr rod when in electrical contact, provided there were high concentrations of impurities in the salt. Fluid flow could also enhance anodic dissolution. However, dissolution rates could be suppressed from that previously observed if the salt is of higher purity, there is poor electrical contact, or the rod/salt is at a much lower temperature. To determine the Zr rod weight loss rates, the Zr section of the rod can be unscrewed and weighed before and after the loop tests, or periodically during testing if the rod is cleaned well prior to immersion.

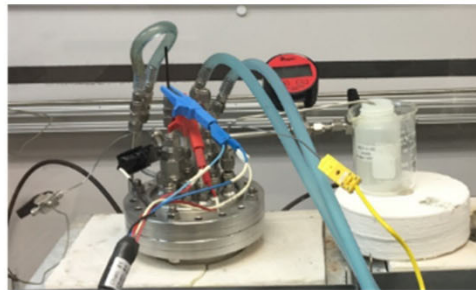
Before sending the Zr getter rod and associated insertion apparatus to ORNL, DOE requested the design and fabrication of an electrolytic Mg production cell that could be inserted via the same double-ball valve setup. To fabricate the electrode, alumina ceramic was chosen for the majority of the electrical insulator. The selection of alumina was aimed at minimizing the number of different materials in the system, as ANL intends to use alumina for their electrochemical probe. The actual current density to be used can vary, but literature provided by ICL suggests that a current density of 1.2 A/cm² is ideal for maximum Mg production efficiency at temperatures between 650 °C and 750 °C. Mg can be produced at lower temperatures, but it will likely coat the plating electrode and need to be allowed to dissolve or oxidize off to perform its corrosion mitigation role. The cell used for initial Mg electrolytic dissolution tests is displayed in Figure 37.

Shown in Figure 38 is the fabricated electrolytic cell apparatus along with schematics of the electrode assembly in operation. The three-electrode assembly is interchangeable

with the Zr gettering rod. Based on previous work, a decision was made to use glassy carbon for the anode. Graphite is commonly used for the anode but can degrade with Cl₂ gas formation and leave graphite particulates in the salt. Glassy carbon should be much more resistant to degradation. Tungsten was used for the cathode since it should not react with the reduced Mg and is already used on the electrochemical probe by ANL (thereby minimizing different materials in the system). It should be noted that during operation, the gas vented from the double ball valve would need to be scrubbed to remove Cl₂ gas. Upon verifying compatibility of the electrode apparatus with the Zr gettering assembly, the latter was shipped to ORNL

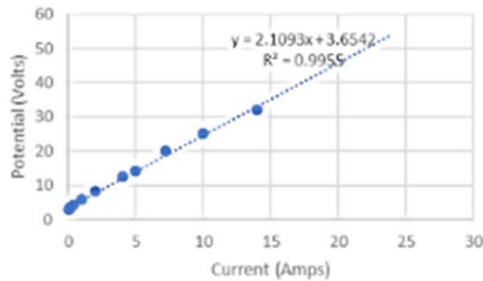


Prepped in glovebox



Ran in standard furnaces, purged at 100 sccm with Ar and vented to NaOH solution

- Ran in 2-electrode configuration
- Tungsten as WE (Mg plate and drip-off electrode)
- Glass carbon as CE
- Thermocouple in 0.25" thermowell
- PBN crucible
- Years-old KCl-MgCl₂ used
- From 0.16 – 450 W
- J from 0.02 – 4.4 A/cm²

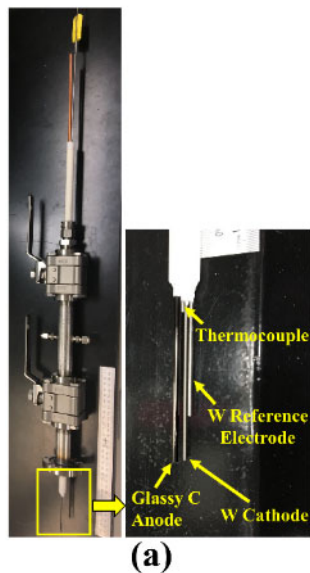


Linear I-V relation

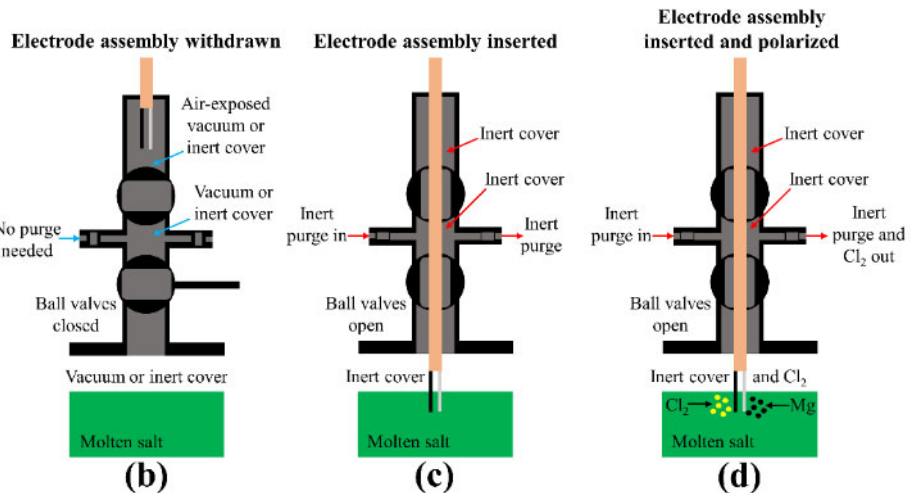


Post-test: Mg on W and pink salt

Figure 37. Initial Mg reduction tests.



(a)



(b)

(c)

(d)

Figure 38. (a) Electrolytic cell apparatus fabricated to fit in the gettering assembly and schematics of the electrode assembly when (b) withdrawn, (c) inserted, and (d) inserted and polarized.

Subtask 2.1.4: CFD Modeling of Optimized Getter Bed for Thermosiphon Integration

Task 1: Develop the three dimensional model to predict the effect of different getter bed inside the flow loop on the temperature, pressure, and velocity.

Establishment of 3D Flow Loop Geometry

Figure 39 shows the three-dimensional geometry created from drawing and information provided by ORNL [14]. The tube of the flow loop is Inconel 600. There are three heaters installed at the hot leg at the right-hand side and bottom of the Flow Loop. They are called Top Hot Leg, Middle Hot Leg, and Bottom Hot Leg. These three heaters control the temperature gradient in the Hot Leg. With a temperature difference between Hot Leg and Cold Leg (left), the fluid inside the Flow Loop is moved around in a counter-clockwise direction due to natural convective flow.

Computational Mesh Generation

Polyhedral mesh was selected for computational cells in the Flow Loop. There are two main parts: one is Inconel 600 tube called solid domain and second is fluid flowing inside the tube called fluid domain. The Base Size of two domains was set as 0.001 m. Star-CCM+ commercial software provided by Siemens was used to generate the computational mesh. The total number of computational cells is 9,178,687. Figure 40 shows the computational mesh in this work. The mesh test has been performed with perfect cell in overall. All computational cells have Face Validity equal or greater than 1.0 and 99.42% of computational cells have Cell Volume Change equal or greater than 0.1.

Model Development and Numerical Procedure

Computational Fluid Dynamics (CFD) technique was used to performance model calculation for heat and flow characteristic. Finite control volume based commercial CFD software from Siemens, Star-CCM+, was chosen as the computational tool [15]. The model includes mass, energy and momentum balance equations with inclusion of gravity effect. The boundary of Hot Leg was set at a fixed temperature: Top Hot Leg = 850 K, Middle Hot Leg = 757 K, and Bottom Hot Leg = 729 K. The thermal properties of Inconel 600 and Pb-Li were taken from previous research [16, 17]. Algebraic Multigrid (AMG) algorithms are used to solve equations and the model calculation is set to converge when the residual of all variables (i.e., pressure, velocity, and temperature) is below $1.0e-4$.

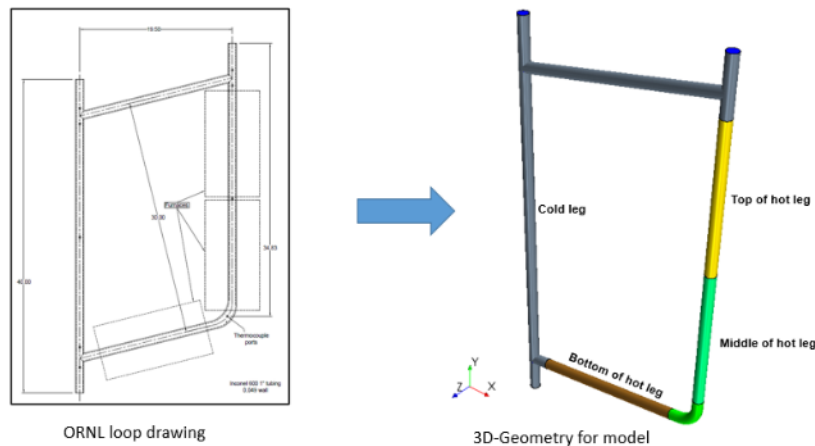


Figure 39. Three-dimensional geometry model of ORNL's flow Loop.

Model Predictions and Validations

Figure 41 presents model validation against Ref [14]. This figure shows the numerical values and experimental data at 6 locations where the thermocouples were installed. With temperature boundary condition applied in this first trial, the model prediction gives good agreement with experimental data. The maximum error is around 0.95% at the top left of Cold Leg and the minimum error is around 0.18% at location of Bottom Hot Leg.

Figure 42 shows the model prediction of temperature compared with experimental data under 650 °C Pb-Li flow loop condition. The experimental setup and data were obtained at ORNL. Again, the model predictions agree well with experimental measurement data for all 6 locations with error less than 2%. Figure 43 shows predictions of velocity and pressure distributions at 650 °C Pb-Li flow loop. These distributions are similar to the distributions given at lower temperature as shown in previous report but with the higher values.

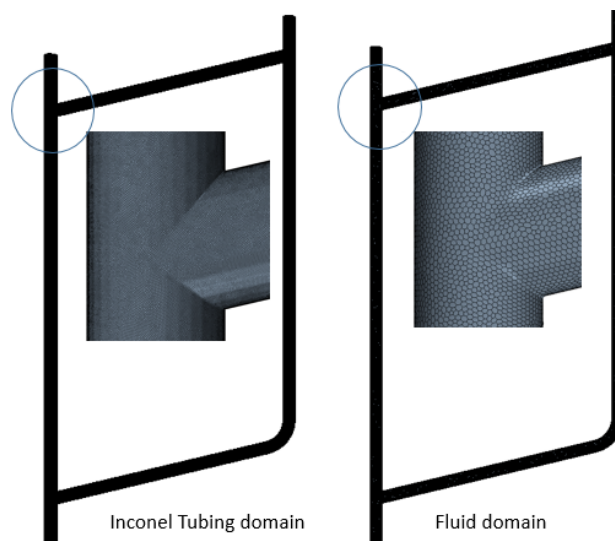


Figure 40. Computational cells.

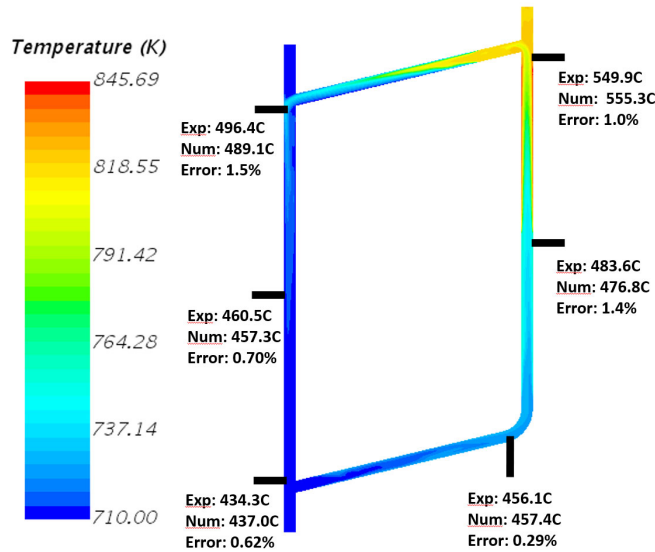


Figure 41. Temperature validation against Ref. [14].

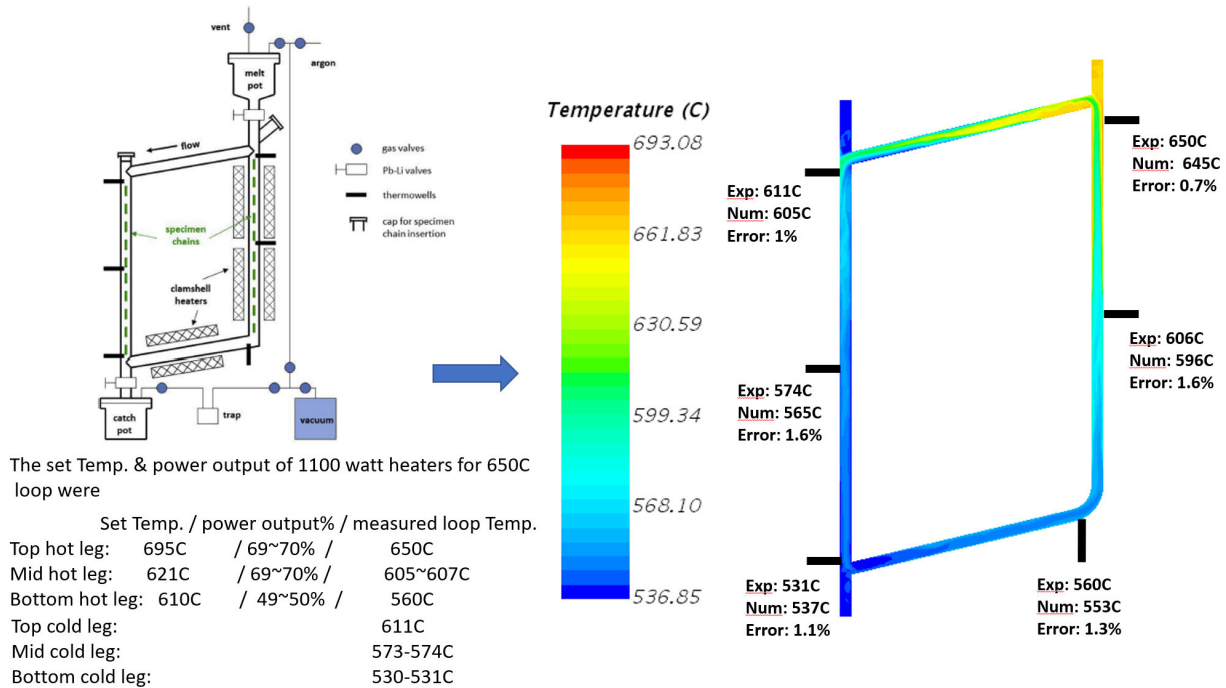


Figure 42. Numerical Predictions of Pb-Li Flow Loop for 650 °C loop. Data provided by Jun, Jiheon: junj@ornl.gov

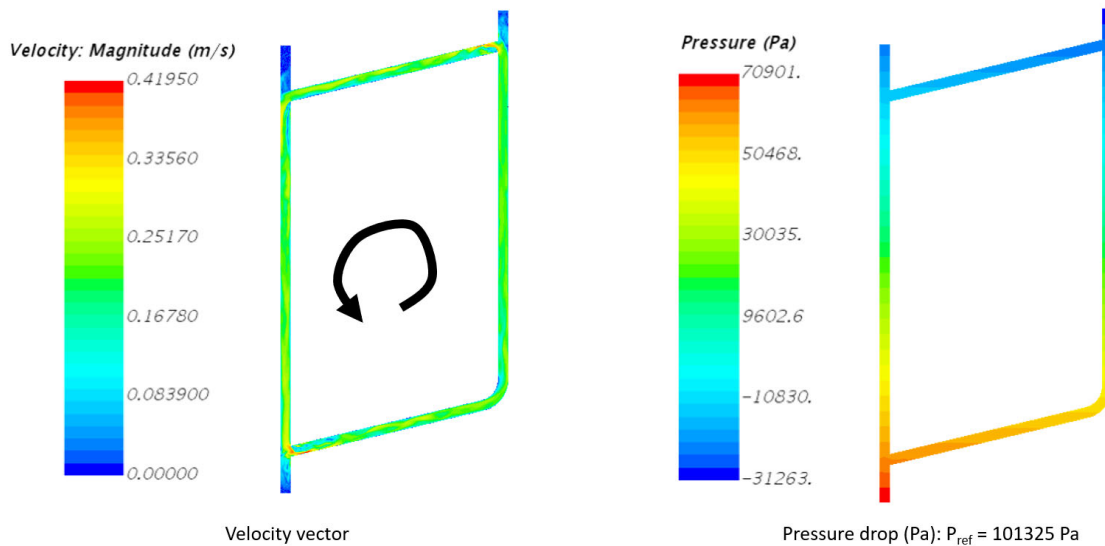


Figure 43. Numerical predictions of velocity vector (m/s) and pressure (Pa).

Calculation of flow characteristics for a flow loop with three different getter bed designs suggested by SRNL and compare against flow loop without getter bed

The bed design to be installed in the flow loop has been proposed for three types by SRNL team. The first one is the Rod type as shown in Figure 44-1. It is Zirconium with the diameter of 2 mm and the length of 50 cm; it is seated at the bottom of cold leg as shown in Figure 44-1. The second design is the Tube type. This tube design is also Zirconium with the thickness of 5 mm as shown in Figure 44-2. The outer diameter is the same as inner diameter of flow loop; the length is also 50 cm. The last design presented in Figure 44-3 is Honeycomb type made of Zirconium. It can be counted as a porous material. Therefore, we set its properties as follow; the diameter is the same as inner diameter of flow loop, the length is 10 cm, the porosity is 0.5, the tortuosity is 1.1, and the viscous resistance is 20000 kg/m³-s.

Figure 45 shows the temperature comparison of model predictions between these three designs against the flow loop without bed (Figure 45-0). The temperature distributions reveal that Overall, Tube design shown in Figure 45-2 gives the lowest temperature profile. Honeycomb design (see Figure 45-3) gives the highest temperature at the hot legs but the lowest at the cold legs. Furthermore, Rod design presented in Figure 45-1 gives the similar profile as the flow loop without bed (Figure 45-0).

The predictions of velocity magnitude and their distributions for all three designs compared with no-bed type are shown in Figure 46. The model predictions conclude that the Tube design gives the highest velocity magnitude particularly inside the Zirconium tube. This phenomenon can cause the lower in temperature as it gives better heat transfer inside the flow loop as already presented in Figure 45-2. The Honeycomb design gives the lowest velocity magnitude due to the insertion of porous honeycomb type bed. However, the prediction of this design can be changed by adjusting the properties of porous material. The Rod design shown in Figure 45-1 gives the similar velocity profile as the flow loop without bed.

Figure 47 presents the model prediction of pressure. The pressure distribution and its difference are similar for all four cases including the flow loop without bed. In detail, the Tube design gives the highest pressure difference and the Honeycomb type was predicted to be the lowest pressure difference.

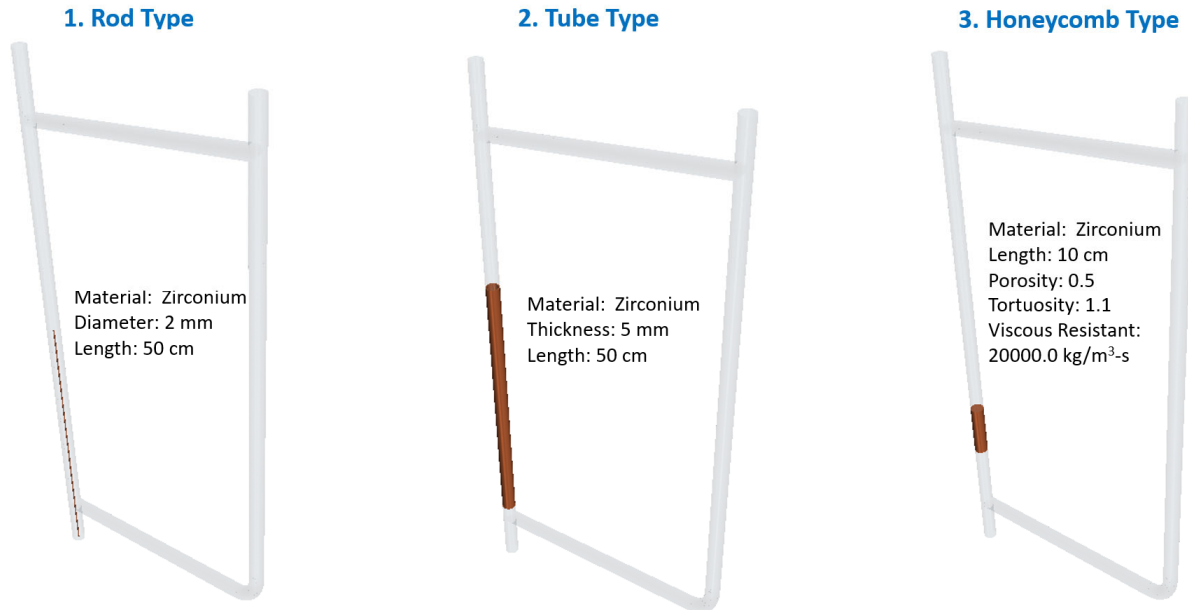


Figure 44. Getter bed designs proposed by SRNL.

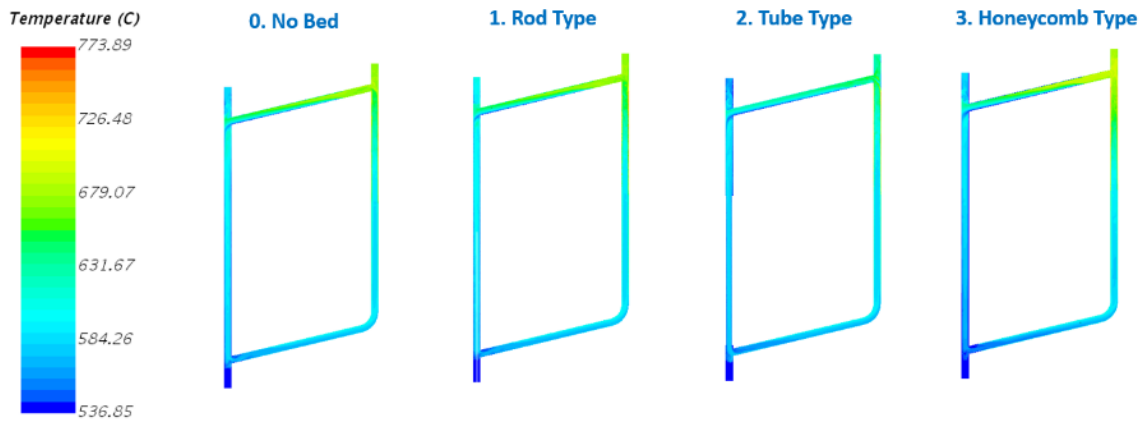


Figure 45. The effect of getter bed designs on temperature distribution.

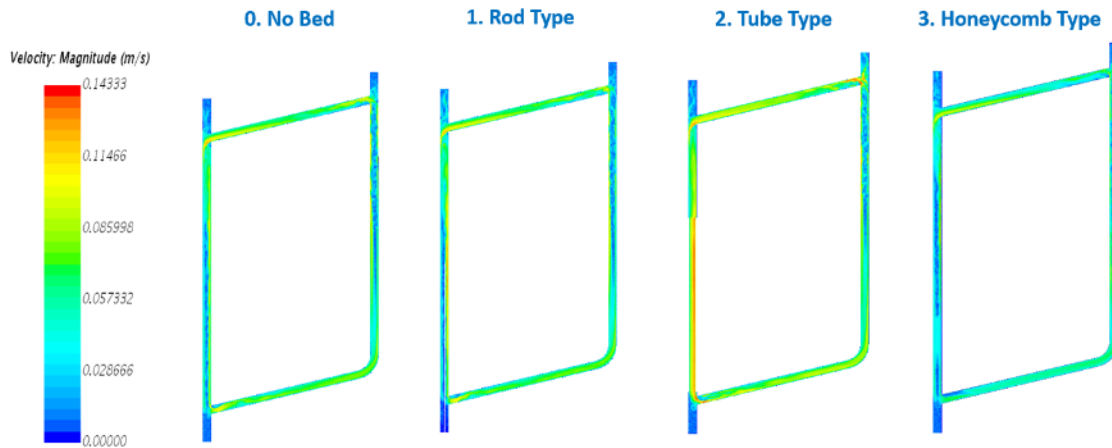


Figure 46. The effect of getter bed designs on velocity distribution.

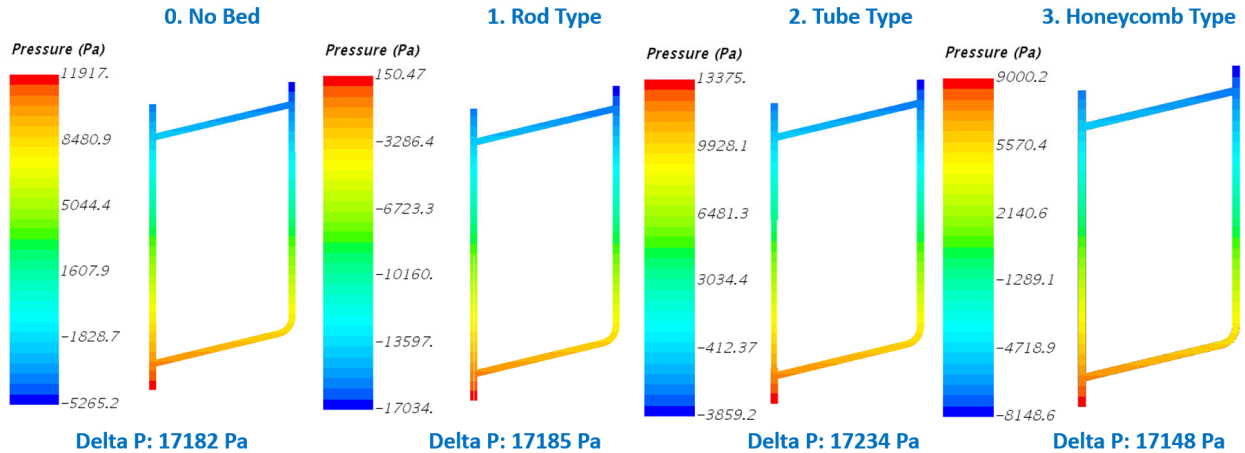


Figure 47. The effect of getter bed designs on pressure distribution.

The Getter Bed designs of improvement

Figure 48 shows the Rod type design of improvement from previous design and setup to the new proposed design and setup. From this figure, it shows that the rod's diameter was increased from 2 mm to 10 mm and the length was reduced from 50 cm to 25 cm. The increase of cross-section area from previous design would equally create hydraulic diameter compared to other designs. The position of the new design was moved to the top of the cold leg inside the flow loop.

Figure 49 presents the Tube type design modified from the previous design. The Tube design has the wall thickness of 5 mm thus creating the same hydraulic diameter as new Rod type shown in Figure 1. In this new Tube type design, the length was shortened from 500 mm to 100 mm. This length is the same as the length of Honeycomb type getter bed shown in Figure 50.

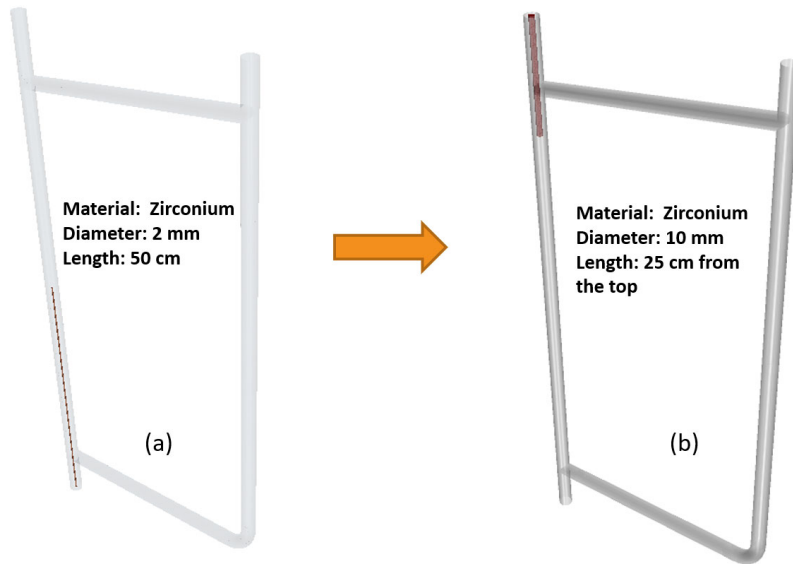


Figure 48. The design improvement of Rod type: a) Previous design and b) New design.

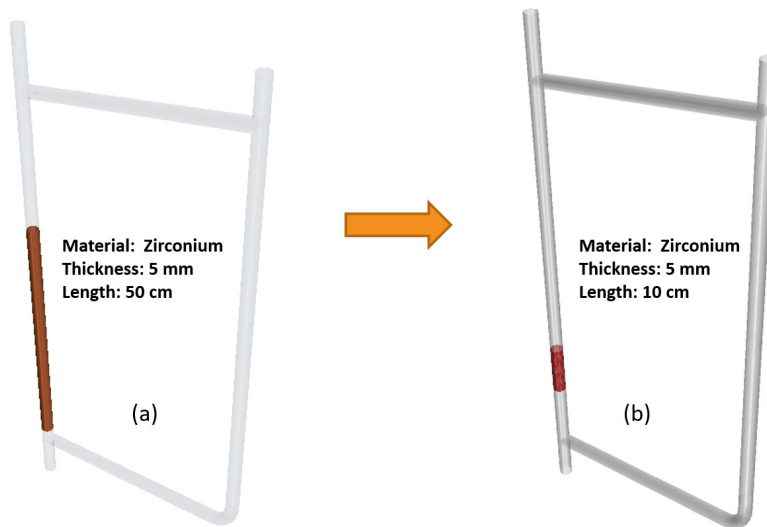


Figure 49. The design improvement of Tube type: a) Previous design and b) New design.

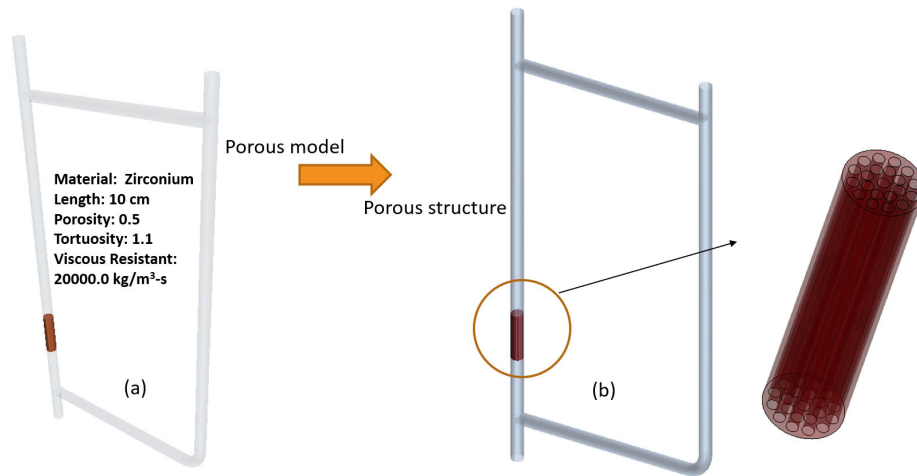


Figure 50. The design improvement of Honeycomb type: a) Previous design and b) New design.

Figure 50 shows the getter bed of Honeycomb type. This honeycomb type is designed to be high pore volume material. In previous study, the model of honeycomb getter bed was assumed to be porous model with its properties given in Figure 50a. However, the model prediction gave unrealistic results and therefore, the Honeycomb type was reconstructed as close as honeycomb shape as shown in Figure 50b. It is noted that the cross-section area of open volume is the same as the cross section areas in Figures 10b and 11b and therefore, the hydraulic diameter of these designs are similar.

Model predictions

Figure 51 shows the temperature comparison of model predictions between these three new designs against the flow loop without bed (Figure 51-0). The temperature distributions reveal that in overall, the Tube design shown in Figure 51-2 still gives the lowest temperature profile. The Honeycomb design (see Figure 51-3) also yet gives the highest temperature at the hot legs but much lower at the cold legs. The Rod type design (Figure 51-1) gives the most uniform temperature distribution compared to other design. Furthermore, the overall temperature distribution of Honeycomb design is similar to the profile of the flow loop without getter bed (Figure 51-0).

The predictions of velocity magnitude and their distributions for all three designs compared with no-bed type are shown in Figure 52. The model predictions conclude that the Tube design Figure 52-2) gives the highest velocity magnitude particularly inside the Zirconium tube followed by the Honeycomb type design (Figure 52-3) in the getter bed. This phenomenon can cause the lower in temperature as it gives better heat transfer inside the flow loop as already presented in Figure 51-2 and 3. The Rod design shown in Figure 52-1 gives the similar velocity profile as the flow loop without bed.

Figure 53 presents the model prediction of pressure. The pressure distribution and their differences are similar for all four cases including the flow loop without bed. In specific detail, similar to the previous designs, the Tube design gives the highest pressure difference and the Honeycomb type was predicted to be the lowest pressure difference but the values of both of them are not significant.

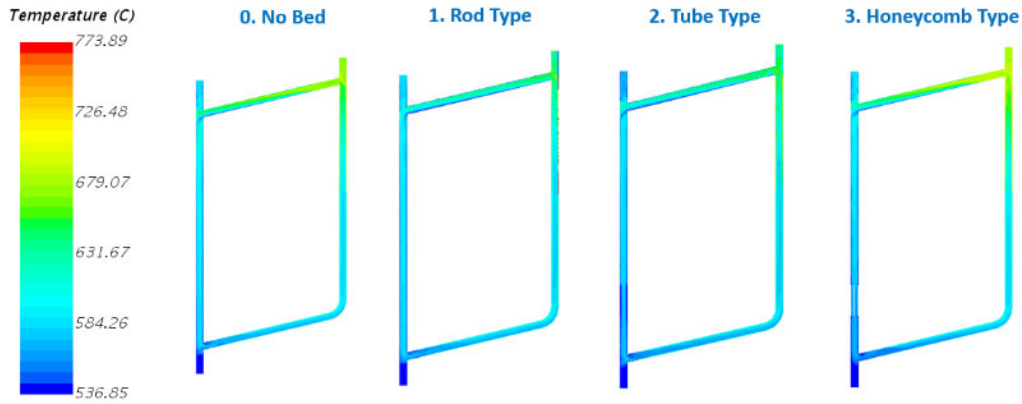


Figure 51. The effect of getter bed designs on temperature distribution.

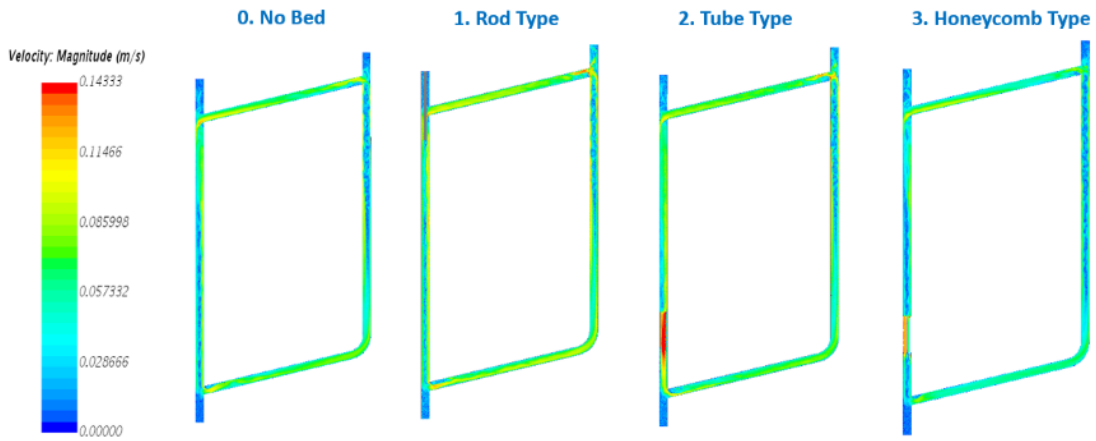


Figure 52. The effect of getter bed designs on velocity distribution.

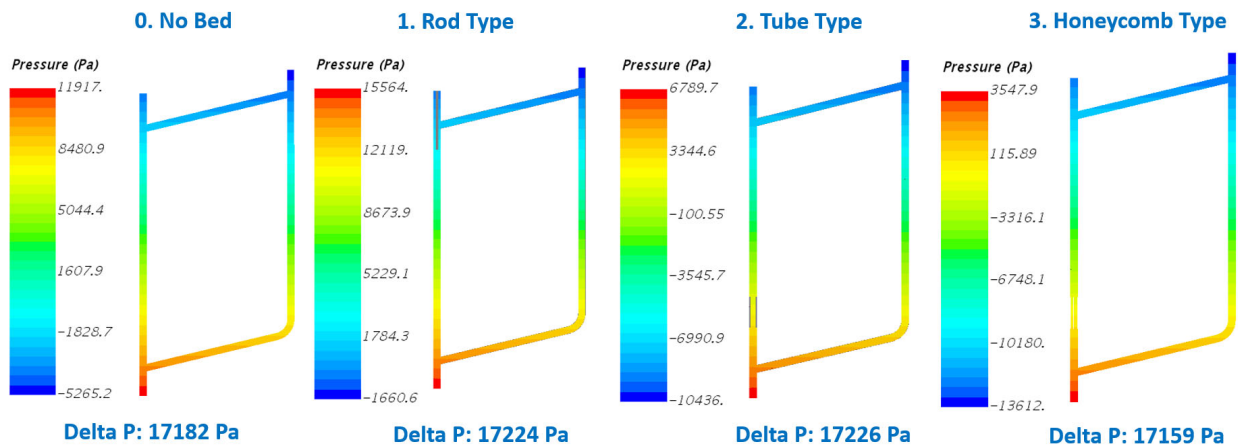


Figure 53. The effect of getter bed designs on pressure distribution.

Task 2: Develop the three dimensional model to predict the corrosion behavior of specimens inside the flow loop.

Development of model geometries of specimen, flat spacer, chain spacer, and ring

Figure 54 shows the image of specimen, flat spacer, chain spacer and rings provided by ORNL. There are total of 28 specimens with 14 specimens are hanged inside the cold leg of flow loop and another 14 specimens are inside the hot leg of flow loop. There are 12 flat spacers with 6 flat spacers are inserted between specimens inside the cold leg and another sets are located in the hot leg. There are 4 chain spacers with 2 spacers on each side those are in the middle and the bottom to maintain the center of gravity of the specimens' line. Lastly, there are 42 rings connected between each specimen, flat spacer, and chain spacer. Based on the conversation with ORNL, all of solid samples mentioned above are made by Alloy 600. The CAD drawing of these Alloy 600 specimens, flat spaces, and chain spacers were also provided by ORNL.

Figure 55 presents the development of model geometry of the Alloy samples in Figure 54. The CAD geometries were created and imported to CFD model. Then they were positioned inside the flow loop presented in this report as also shown in Figure 55. However, the computational mesh was needed to recreate during the addition of specimens, flat spacers, chain spacers, and rings. Polyhedral type of mesh was selected and generated with the total computational cells of around 11 million. The conservation of mass, momentum, energy equations of the CFD solver were computed using high performance computing of 12 processors.

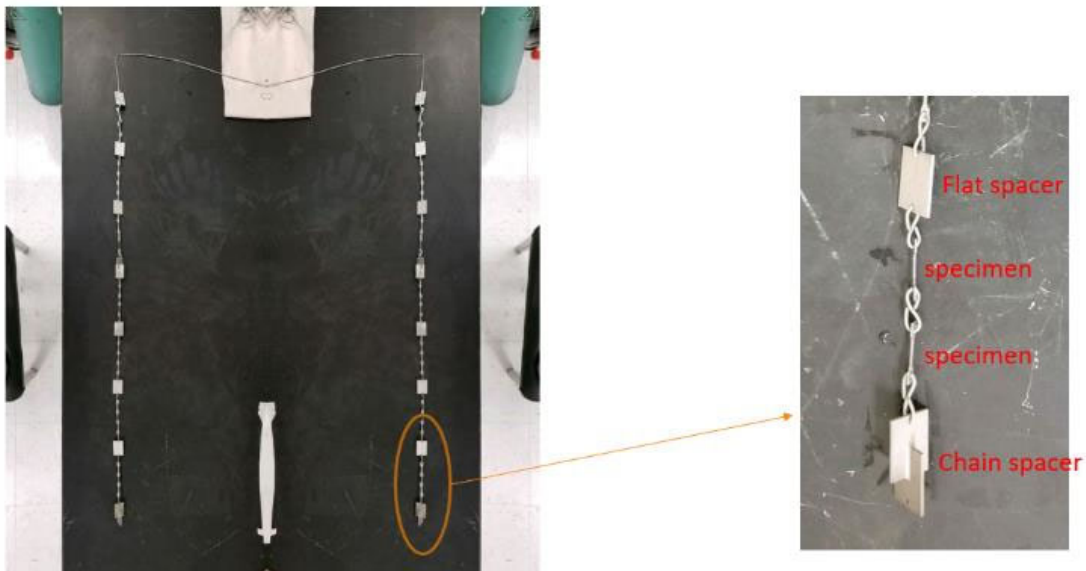


Figure 54. Specimens, flat spacer, chain spacer, and ring inside the flow loop (this images were provided by ORNL).

Composition			Density (g/cm ³)	Heat Capacity (J/g K)	Viscosity (cP)	Thermal Conductivity (W/m K)
NaCl	KCl	MgCl ₂				
-	68 mol%	32 mol%	-5.0997E-04T + 1.8943, R ² = 9.9923E-01	1.9700E-08T ² - 1.2203E-05T + 1.0091, R ² = 9.9763E-01	1.8075E-05T ² - 2.8496E-02T + 1.3489E+01, R ² = 9.9976E-01	-1.0000E-04T + 5.0470E-01, R ² = 1.0000E+00
20.5 wt%	24.5 wt%	55 wt%	-3.9660E-04T + 1.9032, R ² = 1.0000E+00	2.2500E-06T ² - 2.4815E-03T + 1.7897, R ² = 9.9309E-01	Not available but see comments in the actual data tab	Not available but see comments in the actual data tab
~20 mol% ~40 mol% ~40 mol%			1.5015E-06T ² - 1.9041E-03T + 1.5539, R ² = 1.0000E+00			
20-22 mol%	Equimolar KCl and MgCl ₂ to balance		-4.0600E-04T + 1.8821, R ² = 1.0000E+00	-5.2799E-4T + 1.3946 (based on the average of 20, 21, and 22 mol% NaCl compositions)	Not available, recommend using equation below. See comments in the actual data tab	Not available, recommend using equation below. See comments in the actual data tab
27.5 mol%	32.5 mol%	40 mol%	-4.0924E-04T + 1.8922, R ² = 1.0000E+00	-4.6197E-05T + 1.0634, R ² = 9.9992E-01	0.3036*exp(2137.3/T(K))	-1.0000E-04T + 5.0820E-01, R ² = 1.0000E+00
30 mol%	20 mol%	50 mol%	-3.8929E-04T + 1.9063, R ² = 1.0000E+00	-3.6787E-05T + 1.0533, R ² = 1.0000E+00	0.2885*exp(2108.2/T(K))	-8.8889E-05T + 4.9984E-01, R ² = 1.0000E+00
20 mol%	52.5 mol%	27.5 mol%	-4.4248E-04T + 1.8879, R ² = 1.0000E+00	-4.4367E-05T + 1.0580, R ² = 9.9996E-01	0.2803*exp(2153.2/T(K))	-1.1667E-04T + 5.1073E-01, R ² = 1.0000E+00

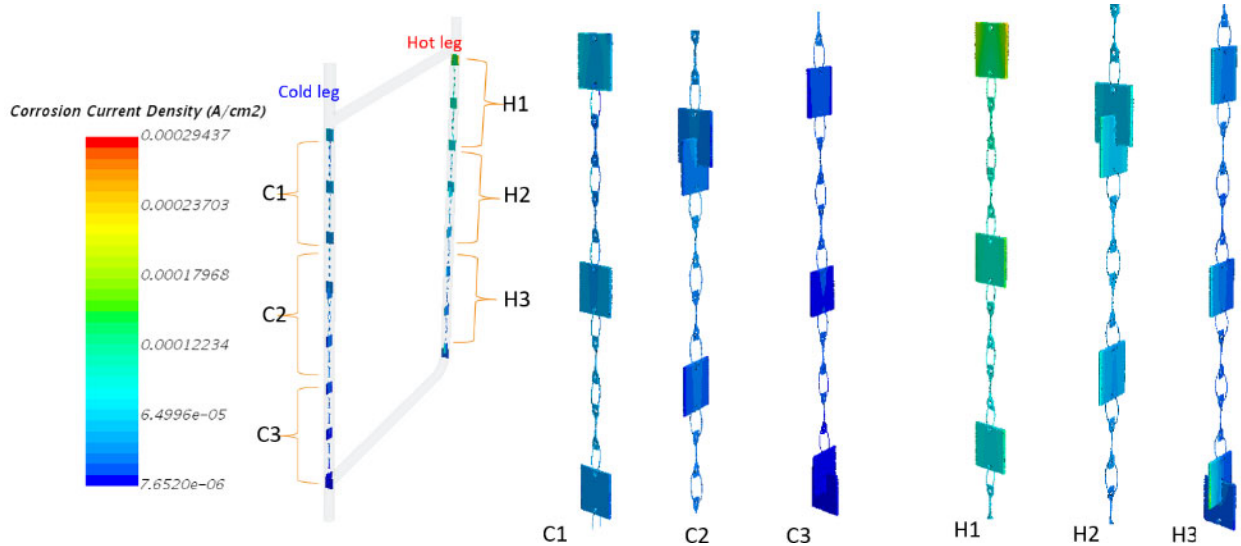


Figure 56. Corrosion rates prediction of specimens, flat spacers, chain spacers, and rings inside NaCl-MgCl₂-KCl (20%-40%-40%) flow loop. All solid samples inside flow loop is Alloy 600.

the harp loop and they are used for further data analysis. Figure 58 shows the effect of salt solutions on temperature profile inside the harp loop. The figure on the left is for the cold leg and the figure on the right is for the hot leg. Overall the temperature profiles of samples in MgCl₂-KCl, 2 compositions of NaCl-MgCl₂-KCl, and the estimated temperature from experimental data look similar. In the cold leg, the temperature profile under MgCl₂-KCl is the higher than temperature profiles under both compositions of NaCl-MgCl₂-KCl and the estimated temperature from experimental data. In the hot leg, the temperature profiles of MgCl₂-KCl looks similar with temperature profile under both compositions of NaCl-MgCl₂-KCl. The estimated temperature profile from experimental data provided by ORNL is the highest. It is noted that the salt solution in the experiment had 0.04% Mg in the salt solution.

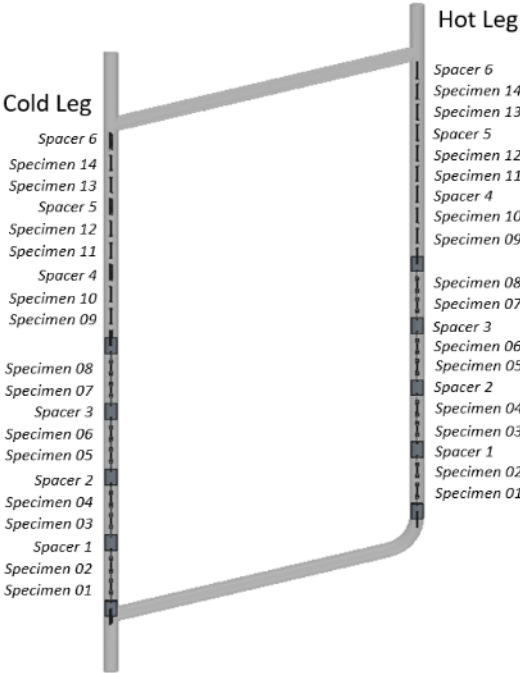


Figure 57. Position of samples (Specimens and Flat Spacers)

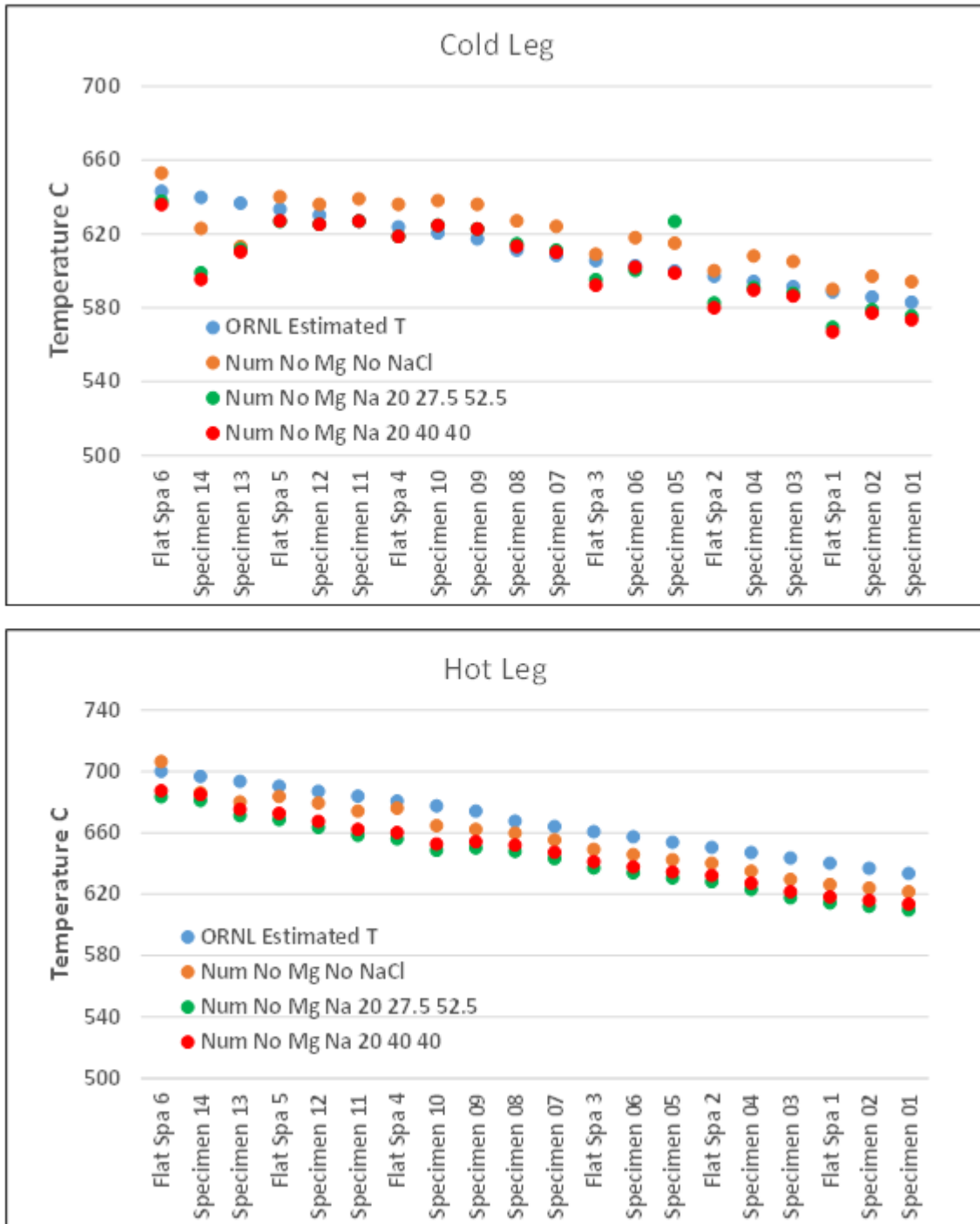


Figure 58. The effect of salt solution on temperature profile

Figure 59 and Figure 60 show comparison of corrosion current density distributions between three salt solutions ($MgCl_2$ -KCl, NaCl- $MgCl_2$ -KCl/20-27.5-52.5, and NaCl- $MgCl_2$ -KCl/20-40-40) for both Hot leg and Cold leg, respectively. The H1/H2/H3 and C1/C2/C3 are the position ranges shown in Figure 56. For Hot leg section shown in Figure 42, the

corrosion current density of $MgCl_2$ -KCl predicts the highest value and the most non-uniform distribution when compared to both compositions of NaCl- $MgCl_2$ -KCl in particular the location H1 where is the hottest region of the flow loop. It is also note that the corrosion current density for 20-40-40 composition of NaCl- $MgCl_2$ -KCl is slight non-uniform than 20-27.5-52.5 composition of NaCl- $MgCl_2$ -KCl even though the average value is about the same. The distributions at the Cold leg look similar for all salt solution especially for both compositions of NaCl- $MgCl_2$ -KCl. The solution of $MgCl_2$ -KCl still provided the highest corrosion current in the Cold leg section.

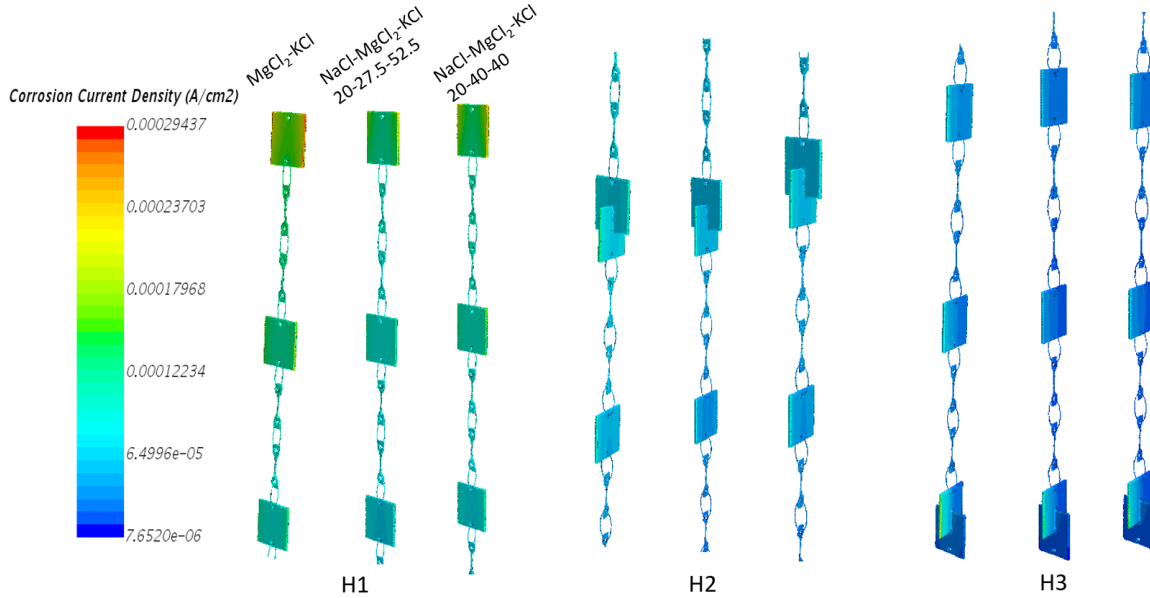


Figure 59. Detail comparison of corrosion current density distribution for three different salt solutions inside hot leg.

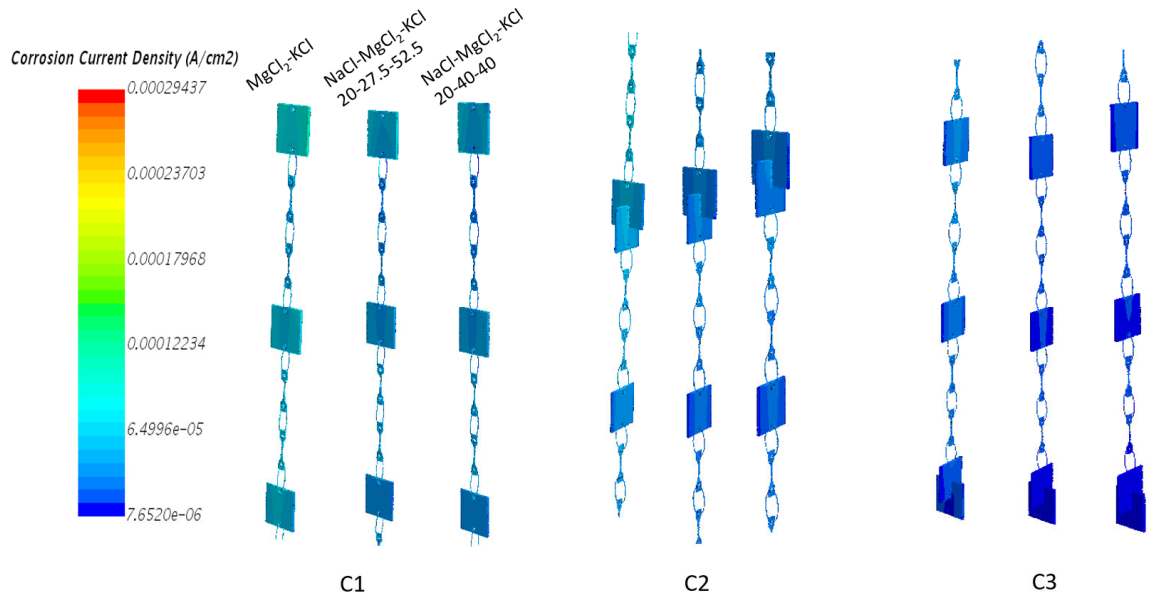


Figure 60. Detail comparison of corrosion current density distribution for three different salt solutions inside cold leg.

Figure 61 and Figure 62 show the effect of salt solution on the mass change of the samples at different temperature inside cold leg and hot leg, respectively. These predictions are also compared with experimental data. Once again, there was 0.04% Mg added in the salt solution used in the experiment for corrosion protection but not in the model simulation. Therefore, in both figures, there were minimal mass change due to corrosion of all samples (specimens and flat spacers) for both in cold and hot legs. However, in the model simulation of both salt solutions without the effect of Mg, the mass loss of all samples is significantly increased with increasing in temperature. The samples in cold leg (i.e., Figure 61) have the less mass loss than the samples in hot leg (i.e., Figure 62). In both figures, the samples in $MgCl_2$ -KCl have more mass loss than both compositions of NaCl- $MgCl_2$ -KCl. This can be easily recognized from the mass change of specimens in both cold and hot legs. Both compositions of NaCl- $MgCl_2$ -KCl show similar averaged mass change with the change in temperature for entire loop. However, these predictions need to be further validated with experimental data under similar operating condition.

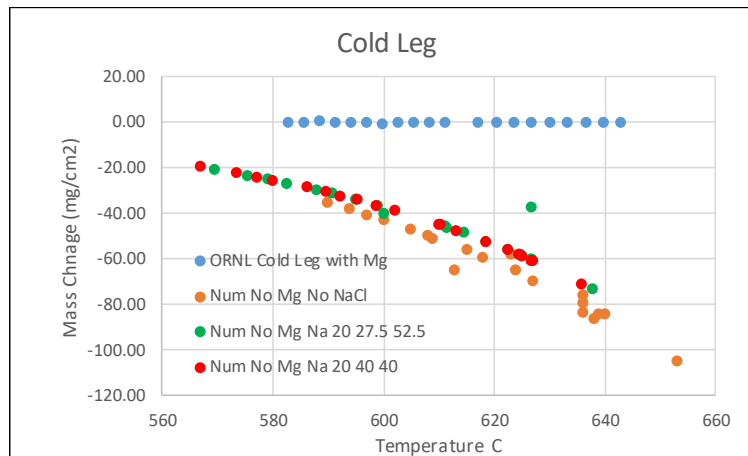


Figure 61. The effect of salt solution on the mass change (mg/cm^2) of the samples at different temperature inside cold leg.

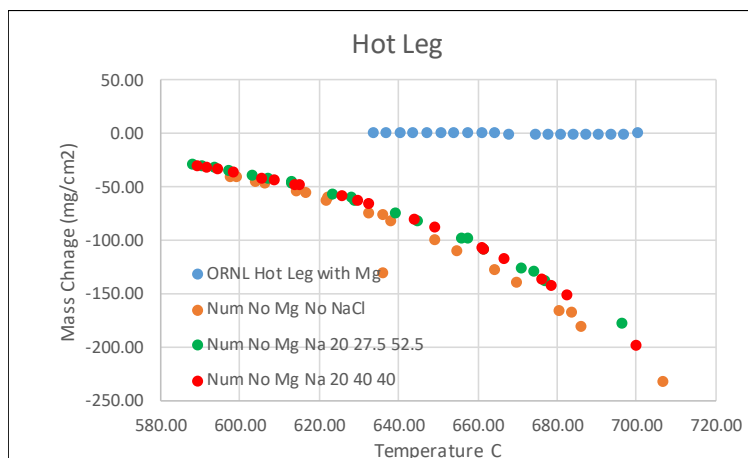


Figure 62. The effect of salt solution on the mass change (mg/cm^2) of the samples at different temperature inside hot leg.

The effect of Mg on corrosion current and mass change

The cathodic protection using magnesium was introduced into the flowloop system under MgCl₂-KCl salt solution. All kinetic equations and their parameters were taken from our previous publication [4] to create the model. Figure 63 shows the prediction of corrosion current after 0.04% mole of Mg was introduced into the MgCl₂-KCl. The overall corrosion current distribution looks similar to the case without Mg where the highest current is located at the top flat spacer of the hot leg where it is the hottest location and the lowest current is located at the bottom chain spacer of the cold leg where it is the lowest temperature. However, the value of corrosion current is significantly lower than the salt solution without Mg.

Figure 64 presents the plots of mass change (lost) in the samples as function of temperature. This figure contains the plots of every case studies (i.e., MgCl₂-KCl no Mg, NaCl-MgCl₂-KCl no Mg, and MgCl₂-KCl with Mg) and are compared with experimental data (i.e., MgCl₂-KCl with Mg). This figure shows that by introducing the 0.04% mole of Mg into the salt solution (MgCl₂-KCl), the mass loss profile (black marker) is significantly decreased and their values are close to the experimental data. Figure 65 shows the close comparison of the mass change profile of the samples with Mg in the salt solution (MgCl₂-KCl) with experimental data. The prediction shows the mass change (lost) increases with the increase in temperature and they are in between the profile of experimental data. The minimum weight lost due to corrosion is around 0.11 mg/cm² and the maximum is around 0.5 mg/cm². However, the experimental data reveals that there is weight gain of the samples in particular at the lower temperature region. Due to the unclear physic of the weight gain in the sample, the current corrosion model has not included this effect in this quarterly report.

Figure 66 predicts the effect of Mg concentration on the mass change (lost) of the samples. There are three Mg concentration values in this study, which are 0.01%, 0.04%, and 0.1% mole of Mg. The prediction shows that the mass change (lost) is decreased with the increase of Mg concentration. These changes in mass as function of Mg

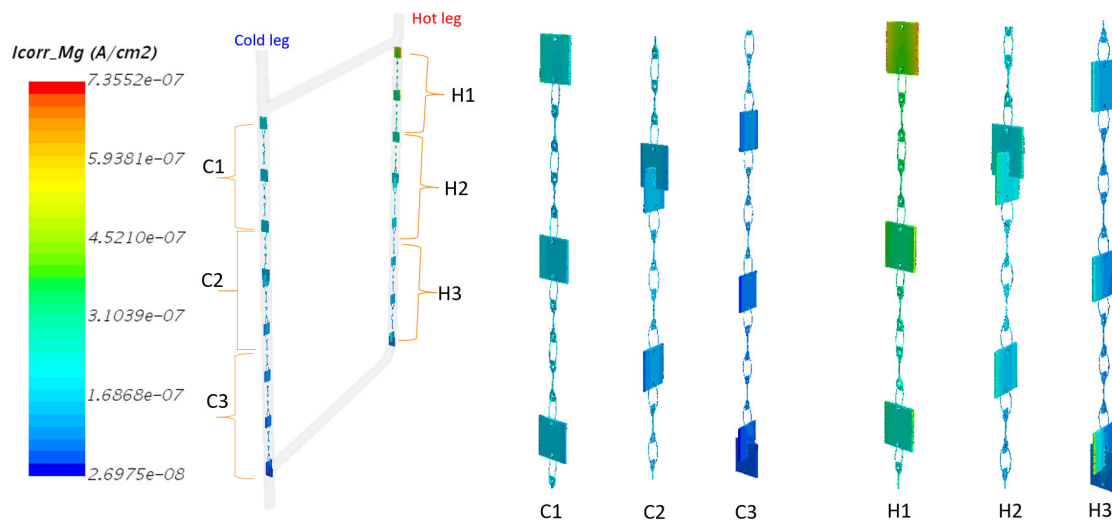


Figure 63. Corrosion rates prediction of specimens, flat spacers, chain spacers, and rings inside MgCl₂-KCl flow loop with 0.04% mole Mg. All solid samples inside flow loop is Alloy 600.

concentration is similar to exponential decay which is also reported in our previous publication [17]. That means there is a significant of mass change when Mg is introduced into the system from 0.01% mole to 0.04% mole but there is small mass change of the sample when Mg is introduced from 0.04% mole to 0.1% mole.

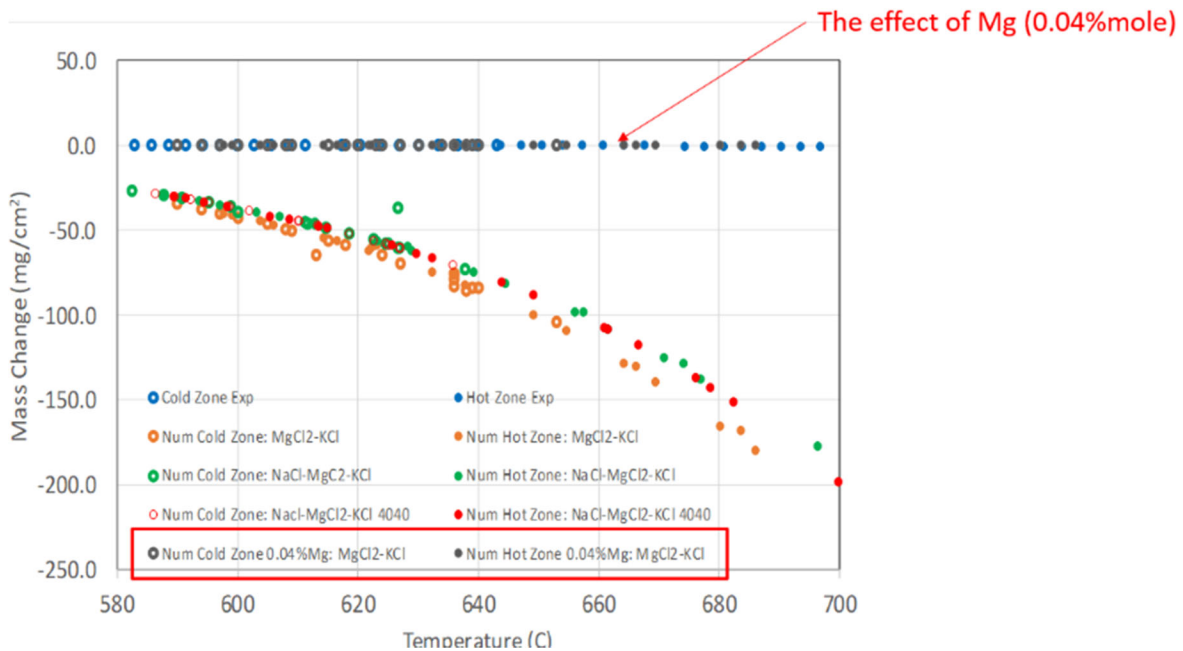


Figure 64. The effect of 0.04% mole Mg on mass change of the samples comparing with other salt solution without Mg and experimental data.

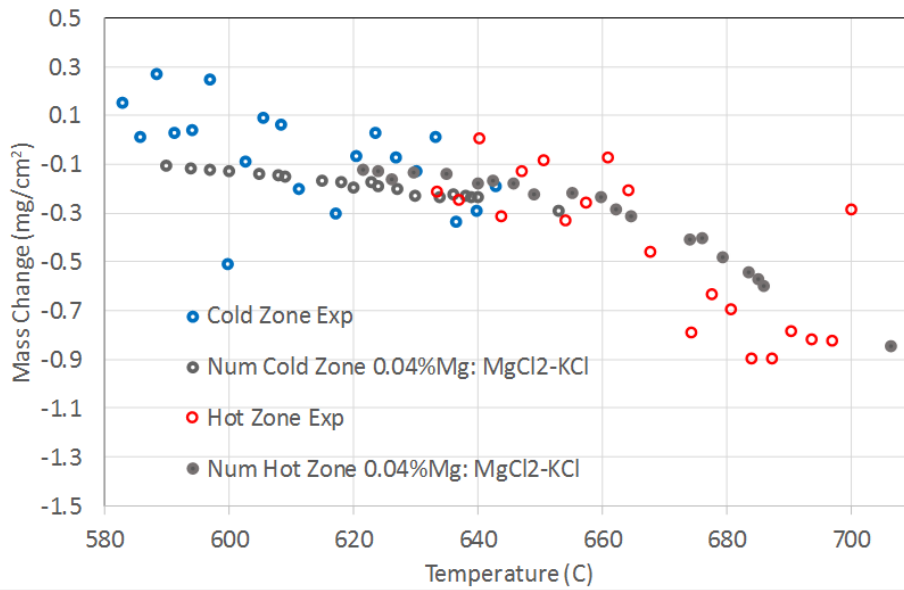


Figure 65. Comparison of mass change plot with experimental data

The effect of Cr²⁺ on the net mass change

Figure 67 shows the concentration distribution of Cr²⁺ that was predicted on the surface of all specimens. This Cr²⁺ has been assumed that it might be deposited on the surface of specimens and affect the net mass change of specimens. This figure confirms that the highest concentration of Cr²⁺ is presented at the specimen that has the lowest temperature (i.e., at the cold leg). At the highest temperature of specimen, it shows the lowest Cr²⁺ concentration (i.e., at the hot leg).

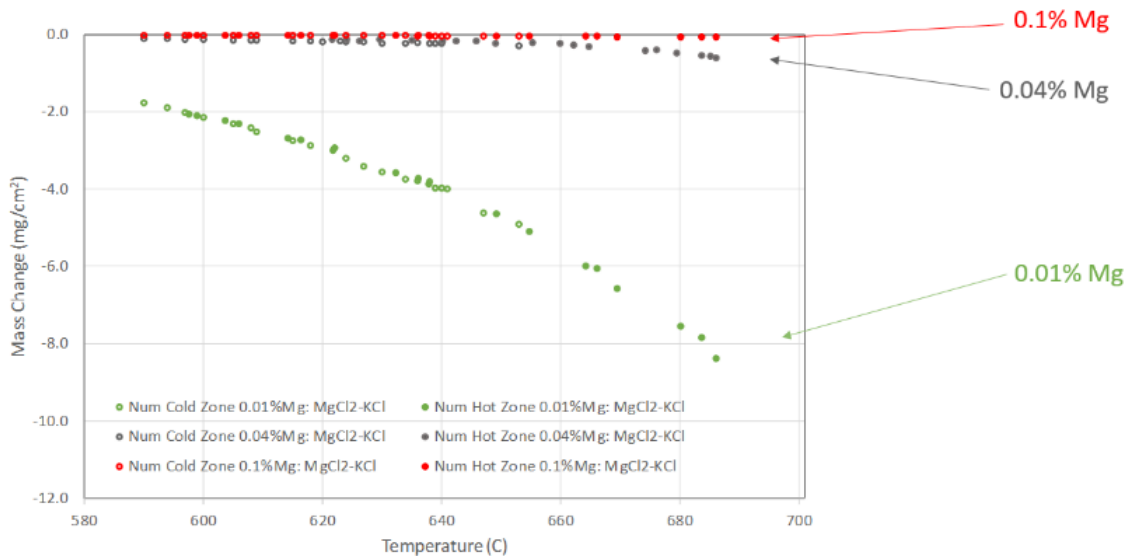


Figure 66. Prediction of the effect of Mg concentration on the mass change.

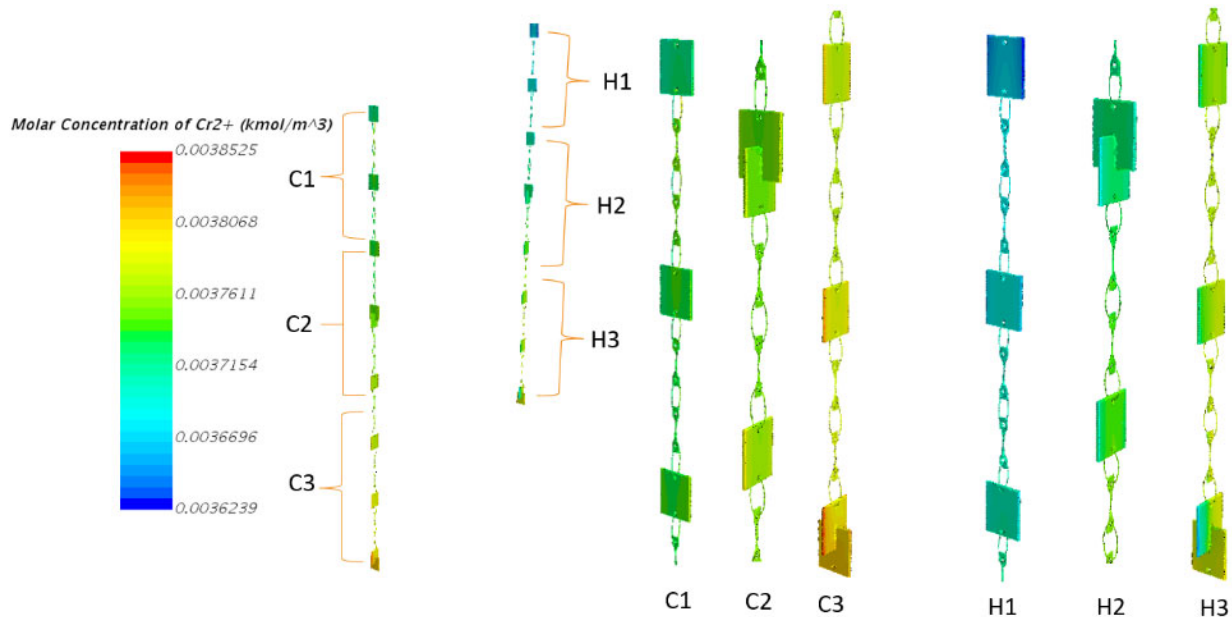


Figure 67. The Cr^{2+} distribution on the surface of specimens.

By incorporating the concentration of Cr^{2+} on the surface of specimens in the mass change of specimens, the new mass change can be predicted by implementing the prediction of mass gain from Cr^{2+} into the mass change of specimens. Figure 68 shows the mass change plots versus experimental data before and after the inclusion of Cr^{2+} . This prediction clearly reveals that the new prediction is closer to the experimental data. Figure 69 shows the comparison of mass change predictions between without the Cr^{2+} and with Cr^{2+} . The prediction noticeably shows that there is significant mass gain of specimens in the Cold Leg compared the Hot Leg. Therefore, the change of specimen mass in the Hot Leg due to the Cr^{2+} is small.

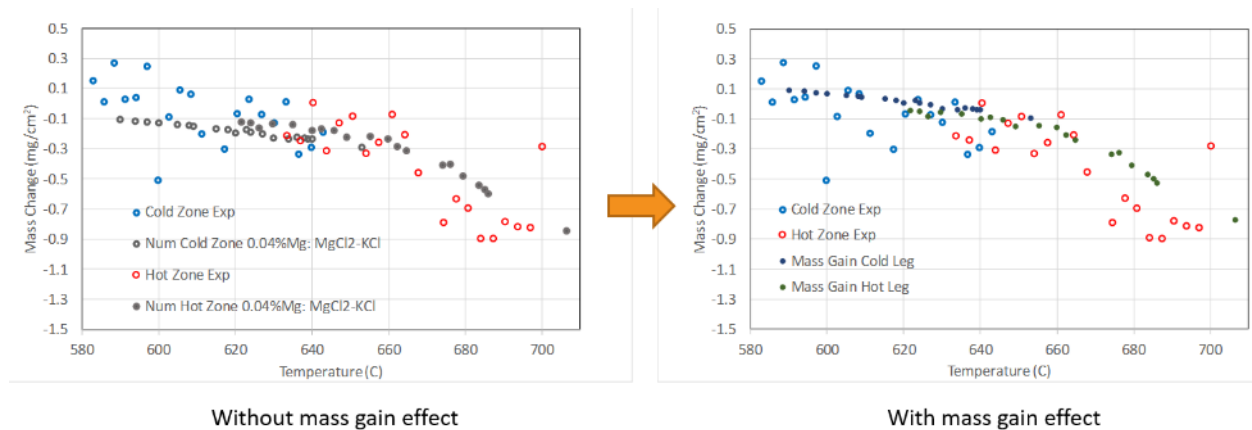


Figure 68. The effect of Cr^{2+} on the net mass change. These data are compared with experimental data.

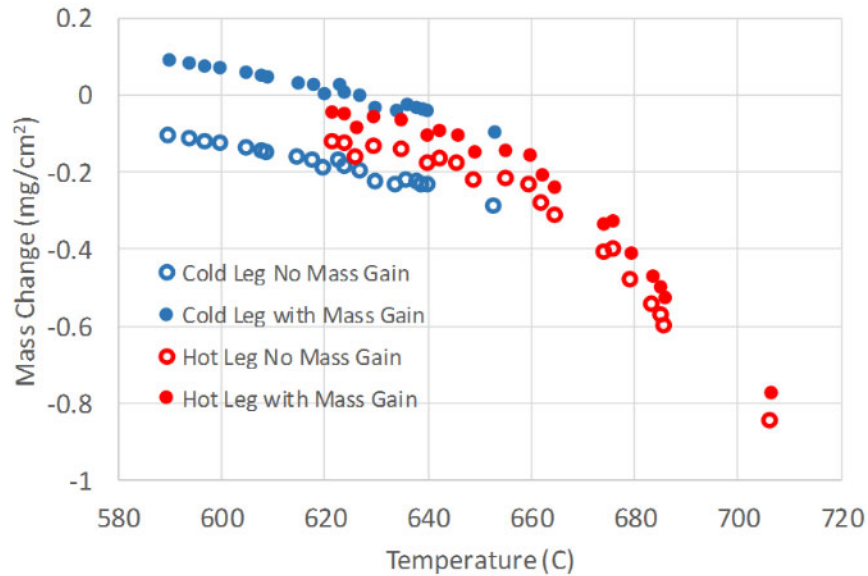


Figure 69. Comparison of net mass change between without and with mass gain effect.

Conclusions

The project team worked very closely with the DOE Chloride Collective on developing standardized protocols for characterization of molten chloride corrosion and molten chloride corrosion mitigation. A statistical analysis of tests performed by chloride collective members was performed and SRNL and NREL were able to match corrosion rates with similar procedures. Methods of molten salt purification that had been developed with ICL and Haynes were adapted and demonstrated for use with multi-kilogram batches of salt. Methods of monitoring the purification by monitoring the pH of a base bath that neutralizes the exhaust gas from salt purification was demonstrated to show when purification was complete.

SRNL was successful in developing spontaneous coating of alloys with active metals that can form a uniform adherent layer on the surface. The active metal coating were effective in preventing corrosion and tests exposing coated samples to molten salts in an air environment were successful in mitigating corrosion of the base metal through sacrificial oxidation of the coating. Controlling the rate of coating deposition by setting temperature was challenging and there were concerns about the ability to control coating thickness on components in a CSP plant to necessary tolerance over long timescales. These concerns led methods of redox control using Mg that SRNL had developed in its previous project to be a favored method of corrosion mitigation. SRNL developed a getter for molten salt corrosion mitigation for insertion into the flow loop at ORNL that could be utilized with Mg or active metals such as Zr to implement corrosion mitigation by redox control. The getter was shipped to ORNL for integration with their flow loop.

SRNL also developed electrochemical methods for monitoring salt purification using pulsed voltammetric methods such as square wave voltammetry (SWV). The decrease of oxidation peaks at 1.2 and 1.3 V appear to very closely track purification of the salt. Monitoring these peaks in-situ during purification or during flow loop operation could

provide valuable information about salt purity and the need for additional purification of the salt.

SRNL also improved corrosion modeling using CFD to implement modeling of corrosion mitigation during non-isothermal transport inside of a flow loop. The modeling results were compared with weight loss results from the ORNL flow loop. It was demonstrated that the CFD model was able to predict variation in weight loss within the flow loop and closely match with experimental data.

References

- [1] B.L. Garcia-Diaz, Fundamental Corrosion Studies in High-Temperature Molten Salt Systems for Next Generation Concentrated Solar Power Systems, Savannah River National Laboratory, SRNL-STI-2019-00017, (2016).
- [2] B.L. Garcia-Diaz, Fundamental Corrosion Studies in High-Temperature Molten Salt Systems for Next Generation Concentrated Solar Power Systems: Q1, Q2, Q3 Progress Reports, Fundamental Corrosion Studies in High-Temperature Molten Salt Systems for Next Generation Concentrated Solar Power Systems: Q1, Q2, Q3 Progress Reports, (2015)
- [3] B.L. Garcia-Diaz, Full Loop Thermodynamic Corrosion Inhibition and Sensing in Molten Chloride Systems: Q1 Progress Report, Full Loop Thermodynamic Corrosion Inhibition and Sensing in Molten Chloride Systems: Q1 Progress Report, (2018)
- [4] H.E. Friedrich, B.L. Mordike, Magnesium Technology: Metallurgy, Design Data, Automotive Applications, 1st ed., Springer-Verlag Berlin Heidelberg, Berlin, 2006.
- [5] T. Bauer, W. Ding, Report on innovative techniques for molten salts high temperature measurements, Solar Facilities for the European Research Area, (2018).
- [6] N. Klammer, C. Engtrakul, Y. Zhao, T. Wu, J. Vidal, Method To Determine MgO and MgOHCl in Chloride Molten Salts, *Anal. Chem.*, 92 (2020) 3598 - 3604
- [7] M.S. Sohal, M.A. Ebner, P. Sabharwall, P. Sharpe, Engineering Database of Liquid Salt Thermophysical and Thermochemical Properties, Idaho National Laboratory, (2010).
- [8] V.L. Cherginets, T.P. Rebrova, Studies of some acid–base equilibria in the molten eutectic mixture KCl–LiCl at 700°C, *Electrochim. Acta*, 45 (1999) 469 - 476.
- [9] W. Ding, A. Bonk, T. Bauer, Corrosion behavior of metallic alloys in molten chloride salts for thermal energy storage in concentrated solar power plants: A review, *Frontiers of Chem. Sci. and Eng.*, 12 (2018) 564-576.
- [10] A.M. Kruizenga, Corrosion Mechanisms in Chloride and Carbonate Salts, Sandia National Laboratory, SAND2012-7594, (2012).
- [11] L. Olson, R. Fuentes, M. Martinez-Rodriguez, B. Garcia-Diaz, J. Gray, Reducing Agent Effects on Haynes-230 in Molten Halide Salts, in: Transactions of the American Nuclear Society, Reno, Nevada, USA, 2014, pp. 859-862.
- [12] T. Paul, A. Paul, Interdiffusion in the Ni-Zr System, *J. Phase Equil. Diffus.*, 36 (2015) 381-389.
- [13] D.F. Williams, D.F. Wilson, G.D. Del Cul, L.M. Toth, J. Caja, J.P. Renier, Advanced High-Temperature Test Loop for Materials Compatibility in Advanced High-Temperature Reactors, FY 2003 ORNL Laboratory Directed Research and Development Annual Report, (2003).
- [14] S.J. Pawel, K.A. Unocic, Compatibility of an FeCrAl alloy with flowing Pb-Li in a thermal convection loop, *J. Nucl. Mater.*, 492 (2017) 41-51.

- [15] Siemens, STAR-CCM+ 2019 user's guide, (2019)
- [16] H.-S. Cho, J.W.V. Zee, S. Shimpalee, B.A. Tavakoli, J.W. Weidner, B.L. Garcia-Diaz, M.J. Martinez-Rodriguez, L. Olson, J. Gray, Dimensionless Analysis for Predicting Fe-Ni-Cr Alloy Corrosion in Molten Salt Systems for Concentrated Solar Power Systems, *Corrosion*, 72 (2016) 742-760.
- [17] B. Tavakoli, J. Weidner, B. Garcia-Diaz, M. Martinez-Rodriguez, L. Olsen, S. Shimpalee, Modeling the Effect of Cathodic Protection on Superalloys inside High Temperature Molten Salt Systems, *J. Electrochem. Soc.*, 164 (2017) C171-C179.